Spacecraft Navigation
Around Small Bodies in Early-characterisation Phases

V.M. Moreno Villa

Technische Universiteit Delft

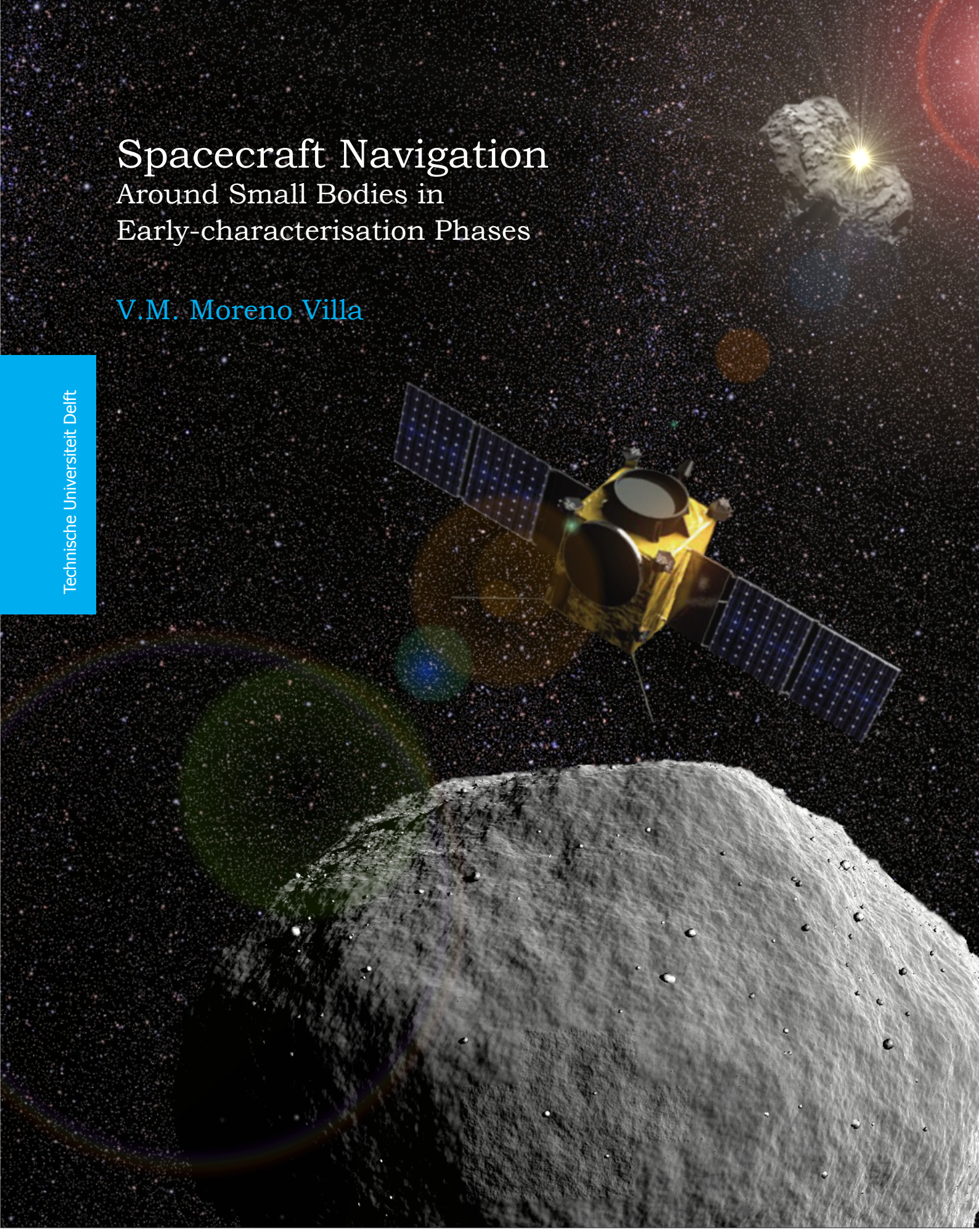

TU Delft Delft University of Technology

Challenge the future

Spacecraft Navigation

Around Small Bodies in Early-characterisation Phases

by

V.M. Moreno Villa

in partial fulfilment of the requirements for the degree of

Master of Science
in Aerospace Engineering

at Delft University of Technology,
to be defended publicly on Friday April 6, 2018 at 9:30.

Supervisors:	Dr. ir. E. Mooij	TU Delft	
	F. Cabral	GMV	
Thesis committee:	Dr. D.M. Stam	TU Delft	Chair
	Dr. ir. E. van Kampen	TU Delft	External Examiner

An electronic version of this thesis is available at http://repository.tudelft.nl/.

Cover image depicts the AIM spacecraft observing the impact of DART's kinetic impactor on the Didymos binary-asteroid system's moon. Asteroid images were obtained with the PANGU® software by courtesy of GMV.

TU Delft Delft University of Technology

gmv INNOVATING SOLUTIONS

"... the cosmos is also within us, we're made of star-stuff,
we are a way for the cosmos to know itself."

Carl Sagan

Preface

The Master of Science in Aerospace Engineering at TU Delft culminates with the MSc Thesis Project, of which this is the final document that collects and synthesises the work performed from May 2017 to October 2017. The complete MSc Thesis Project was carried out at GMV Innovating Solutions in Tres Cantos, Spain.

I am very grateful to GMV for providing me the perfect environment on which I could thrive as an engineer. I have loved the intense working bounds that are commonplace at GMV, where your coworkers are as much interested in your professional development as you are. Among of all them, I would like to thank Francisco Cabral, my supervisor, who has helped me a lot to become much more efficient, always pointing me out the important and the unnecessary. I will always remember our long whiteboard discussions.

Two intense but yet short years ago, I started my MSc in Aerospace Engineering at TU Delft. During this period, I have regained the passion for space and I have revived each of the things that made me chose space engineering in the first place. I would like to thank my supervisor, Erwin Mooij, from whom I have learnt scientific rigour and passion for one's work; his hints and comments made me widen my view, which proved key for performing quality research work. I would like to also thank him for his deep interest, infinite patience and always constant and constructive feedback.

Por último, me gustaría agradecerles a mis padres, sin los cuales esta tesis no existiría siquiera; por su apoyo y esfuerzo constante, que, en último lugar, hizo esto posible.

V.M. Moreno Villa
Delft, February 2018

Abstract

Asteroid exploration is a new booming field for planetary sciences and space engineering. This navigation study deals with the first characterisation of the binary asteroid system, Didymos, for ESA's AIM mission. In particular, it tackles the estimation of its highly-uncertain environment and the scale-factor indetermination problem.

Previous asteroid missions, such as NEAR-Shoemaker and Hayabusa, solved the scale-factor indetermination using ranging instruments while Rosetta combined simultaneous optical navigation and radiometry to solve for it. However, the imposed low-budget character of AIM makes both of these solutions impracticable; radiometry is only gathered when SC-ground communications are established while the fixed navigation camera and the non-steerable high-gain antenna (HGA) prevent the possibility of simultaneous optical and radiometric data. New navigation strategies are studied to effectively solve the proposed problem without incurring into higher operational costs that outweigh the initial system savings.

A GNC simulator was designed to test the behaviour of orbit determination (OD) methods used at ground control centres involving high-precision filtering techniques and realistic measurements models developed on projects for ESA, including a landmark matching model for image processing. Compromise navigation strategies were found, where the OD is first carried out by the sole use of radiometric measurements. These carry information on distances, although referenced to Earth, whereas optical measurements only provide angular information. Then, landmark matching navigation techniques are incorporated to refine the orbit solution and obtain the most precise characterisation of the system, including the landmarks position knowledge.

Results show a difference in magnitude between the along and cross-track directions and the radial direction, caused by the lack of information along the line-of-sight of the optical measurements, which cannot be removed, A weak correlation was found for the relative position of the Earth and the Sun, implying a good level of independence on the simulated scenario's epoch. Manoeuvre execution errors were found to directly drive the performance of the GNC. The inclusion of either a steerable HGA or an altimeter is seen to improve equally the navigation performance.

Taking into account all these considerations, a final navigation strategy that tackles both operational constraints and mission design is proposed. These recommendations and analyses can serve as a starting point for any further asteroid-navigation assessments, in particular, for the newly proposed HERA mission.

Glossary

Acronym	Description
AIAA	American Institute of Aeronautics and Astronautics
AIDA	Asteroid Impact and Deflection Assessment
AIM	Asteroid Impact Mission
ATOMIC	Assessment Toolbox for Optimal MIssion Cost and performance
COPINS	Cubesat Opportunity Payload
CPU	Central Processing Unit
DART	Demonstration of Autonomous Rendezvous Technology
DCP	Detailed Characterisation Phase
DOD	Differential One-way Doppler
DOF	Degrees of Freedom
DOR	Differential One-way Range
DVV	Design Verification and Validation
ECP	Early Characterisation Phase
ECTS	European Credit Transfer and Accumulation system
EKF	Extended Kalman Filter
ESA	European Space Agency
ESOC	European Space Operations Centre
FASTMOPS	Fast Mission Operations Platform
FCS	Flight Control System
FDS	Flight Dynamics System
FEST	Filtering and Estimation Techniques
FOV	Field Of View
GNC	Guidance Navigation and Control
GUI	Graphical User Interface
HGA	High Gain Antenna
IMU	Inertial Measurement Unit
JAXA	Japan Aerospace eXploration Agency
JPL	Jet Propulsion Laboratory
LGA	Low Gain Antenna
LIDAR	Light Imaging Detection And Ranging
LM	Landmark
LOS	Line Of Sight
LRF	Laser Range Finder
MASCOT	Mobile Asteroid Surface scOuT
MGA	Medium Gain Antenna
MJD	Modified Julian Date
MUSES	MU Space Engineering Spacecraft
NAC	Narrow Angle Camera
NASA	National Aeronautics and Space Administration
NEA	Near-Earth Asteroid
NEAR	Near-Earth Asteroid Rendezvous
NSG	Non-Spherical Gravity
ODE	Ordinary Differential Equation
ODP	Orbit Determination Program
PDF	Probability Density Function
PDP	Payload Delivery Phase
RAAN	Right Ascension of the Ascending Node

Acronym	Description
RMS	Root Mean Square
SC	Spacecraft
SRD	System Requirements Document
SRIF	Square Root Information Filter
SW	Software
TU Delft	Delft University of Technology
UKF	Unscented Kalman Filter
UTC	Universal Time Coordinated
VLBI	Very-Long Baseline Interferometry
WAC	Wide Angle Camera
WP	Work-Package

List of Notations

Regarding the case font of the symbols used, the following classification has been followed:

- $\mathbf{A}$ Capital bold symbols represent matrices, excepting velocity $\mathbf{V}$ and augmented state-vector $\mathbf{X}$
- $\mathbf{a}$ Vector are shown in lowercase bold font
- a Scalars are represented in italic
- a Functions, units, and other text are written using the plain font
- α Greek letters are used for angles, excepting $\boldsymbol{\omega}$, $\boldsymbol{\Lambda}$, and $\boldsymbol{\Phi}$

Accents, subscripts, and superscripts represent:

- $\mathbf{A}^T$ Transpose matrix
- $\mathbf{A}^{-1}$ Inverse matrix
- $\mathbf{A}_{ij}$ An element of $\mathbf{A}$ in the ith row and the jth column
- a_i The ith element of a vector, or ith vector
- $\|\mathbf{a}\|$ Euclidean norm of a vector
- $\dot{a}$ First derivative of a
- $\ddot{a}$ Second derivative of a
- $\hat{a}$ Estimate of a
- $\overline{a}$ A-priori estimate of a
- $\breve{a}$ Estimated deviation of a

Latin symbols:

Symbol	Units	Description
$\mathbf{A}$	m^2	Area
b	various	Bias error
$\mathbf{C}$	various	Dispersion matrix
C_r	-	Solar radiation pressure coefficient
$\mathbf{F}$	N	Force vector
f	m	Focal distance
g	various	Global parameters
$\mathbf{H}$	various	Design matrix
$\mathbf{I}$	-	Unit matrix
$\mathbf{l}$	various	Local parameters
$\mathbf{M}$	various	Correlated process noise propagation matrix
n	various	Noise error
$\mathbf{P}$	various	Covariance matrix
P_R	N/m^2	Solar pressure
$\mathbf{R}$	various	Upper-triangular Cholesky decomposition of the covariance matrix
$\mathbf{R}_{B/A}$	various	Rotation matrix from frame A to frame B
$\mathbf{T}$	various	Orthonormal transformation matrix
$\mathbf{V}$	m/s	Velocity vector
$\mathbf{q}$	-	Quaternion
$\mathbf{r}$	M	Position vector
u	various	Element of a series
$\mathbf{X}$	various	State vector
$\mathbf{y}$	various	Observation vector
$\mathbf{z}$	various	Pseudo-observations

Greek symbols:

Symbol	Units	Description
ϵ	various	Residuals
$\boldsymbol{\eta}$	various	Mechanisation error
θ	rad	Pitch angle
Λ	various	Information matrix
Λ	various	Guidance matrix
λ	rad	Latitude
λ	various	Eigen-value
μ	m^3/s^2	Gravitational parameter
ρ	m	Range measurement
$\dot{\rho}$	m/s	Range-rate measurement
$\boldsymbol{\Phi}$	various	Transition matrix
Φ	rad	Rotation angle
ϕ	rad	Longitude
ϕ	rad	Roll angle
ψ	rad	Yaw angle
$\boldsymbol{\omega}$	rad/s	Angular velocity

Contents

1 Introduction **1**

1.1 Motivation . . . 1
1.2 Background information and state-of-the-art . . . 1
1.3 Navigation problem description . . . 2
1.4 Research objectives . . . 3
1.5 Report structure roadmap . . . 3

2 Mission Heritage and Mission Requirements **5**

2.1 NEAR-Shoemaker . . . 5
2.1.1 Mission Overview . . . 6
2.1.2 Spacecraft Systems . . . 6
2.1.3 Navigation Techniques . . . 6
2.2 Hayabusa . . . 8
2.2.1 Mission Overview . . . 8
2.2.2 Spacecraft Systems . . . 9
2.2.3 Navigation Techniques . . . 9
2.3 Rosetta . . . 10
2.3.1 Mission Overview . . . 10
2.3.2 Spacecraft Systems . . . 10
2.3.3 Navigation Techniques . . . 11
2.4 Asteroid Impact Mission . . . 13
2.4.1 Spacecraft Systems . . . 13
2.4.2 Mission Design . . . 13
2.5 Mission Constraints and System Requirements . . . 15
2.5.1 Mission Constraints . . . 15
2.5.2 Feasibility Parameters . . . 17
2.5.3 Requirements List . . . 17

3 Astrodynamics **19**

3.1 Frame transformations . . . 19
3.1.1 Frames of Reference . . . 20
3.2 State Variables . . . 23
3.3 Dynamics around Didymos . . . 24
3.3.1 Didymos system . . . 24
3.3.2 Main Body Force . . . 25
3.3.3 Third-Body Disturbance . . . 25
3.3.4 Solar-Radiation Pressure . . . 26
3.3.5 Non-Spherical Gravity . . . 26

4 Navigation and Guidance **29**
4.1 Measurement Models . . . 29
4.1.1 Radiometric Measurements . . . 30
4.1.2 Optical Measurements . . . 32
4.2 Navigation Algorithms . . . 35
4.2.1 The Square Root Information Filter . . . 36
4.3 Guidance Algorithms . . . 38
4.3.1 Guidance Law selection . . . 39
4.3.2 Fixed-time of Arrival Guidance Law . . . 39
4.3.3 Mechanisation Error Model . . . 40

5 Numerical Methods **43**
5.1 Numerical Integrator . . . 43
5.1.1 The Runge-Kutta Numerical-Integration Method . . . 44
5.2 Chebyshev Polynomials . . . 45
5.3 Cholesky Decomposition . . . 48
5.4 Givens Orthogonal Transformation . . . 48

6 Software Design, Verification, and Validation **51**
6.1 Software Design . . . 51
6.2 Software Development and Implementation . . . 53
6.2.1 Real World . . . 53
6.2.2 Sensors . . . 54
6.2.3 Navigation Filter . . . 54
6.2.4 Guidance . . . 56
6.3 Software Validation and Verification . . . 57
6.3.1 Validation and Verification Plan . . . 57
6.3.2 Unitary Validation . . . 59
6.3.3 Functional Validation . . . 60
6.3.4 Acceptance Test . . . 60

7 Navigation Problem Analysis **63**
7.1 Research Problem . . . 63
7.2 Assumptions and Operational Constraints . . . 64
7.2.1 The Early-Characterisation Phase (ECP) . . . 64
7.2.2 Constants and assumptions . . . 64
7.2.3 Navigation parameter estimation . . . 66
7.2.4 Filter tuning . . . 67
7.2.5 Operational Schedule and Communication Links . . . 67
7.3 Parameter estimation . . . 70
7.3.1 Scale-factor problem . . . 70
7.3.2 Didymos ephemeris estimation . . . 73
7.3.3 Didymoon mass estimation . . . 73
7.4 Strategy preselection . . . 73

8 Results **75**
8.1 Single-arc Navigation Strategy . . . 75
8.1.1 Navigation Performance with Centroiding . . . 76
8.1.2 Navigation Performance with Radiometric Measurements . . . 79
8.1.3 Navigation Performance with Landmark Matching . . . 80
8.2 Multi-arc Navigation Strategy . . . 85
8.2.1 Navigation Performance without Actuation Errors . . . 85
8.2.2 Manoeuvre Impact on Navigation Performance . . . 86
8.3 Sensitivity to ECP parameters . . . 89
8.3.1 Orientation of the Didymos System . . . 89
8.3.2 Distance to the Asteroid . . . 90
8.3.3 Initial Navigation Error . . . 92
8.4 Monte-carlo Analysis . . . 92

9 Conclusions and Recommendations **95**
9.1 Navigation Strategy Selection . . . 95
9.2 Conclusions . . . 96
9.3 Future Work . . . 96
9.3.1 Hybrid and Fully-autonomous Navigation . . . 96
9.3.2 HERA mission . . . 97

A Acceptance Test - Detailed Characterisation Phase (DCP) **99**

B The Early Characterisation Phase (ECP) **101**
B.1 Alternative approaches to the scale-factor problem . . . 101
B.2 Alternative analyses . . . 103
B.2.1 Steerable high gain antenna . . . 103
B.2.2 Altimeter . . . 103
B.3 Final navigation strategy results . . . 104

C GMV Inputs **107**

D Frame transformations **109**

Bibliography **111**

Chapter 1
Introduction

This MSc Thesis deals with spacecraft navigation around small bodies whose characterisation, in other words, the complete description and modelling of the environment around the orbited body, is poor and a very challenging and technology-pushing aspect of guidance navigation and control (GNC) systems.

1.1. Motivation

The Asteroid Impact Monitoring mission (AIM) was projected ESA mission, that together with NASA's Double Asteroid Redirection Test (DART) would fly to the binary asteroid system Didymos, formed by two asteroids: Didymain and Didymoon. Its main mission objectives were to demonstrate new technologies for deep space missions and planetary defence, as well as scientific observations of a binary asteroid system. The mission analysis of AIM was carried out by GMV, an aerospace company that has hosted the present work.

The objective of this work is to give an answer to a still-open research field, which was identified during AIM's consolidation phase, and it required deep analysis. This, together with other research and work fields were listed in [AD01]. It reads as follows:

Initial Asteroid Characterisation. The navigation performance analysis proved the concept of the proximity trajectories, however, these were based in a set of conservative assumptions. Namely the initial characterisation of Didymos (landmark accuracy, dynamical parameter estimation, ephemerides estimation, scale factor problem…) should be addressed to see how these results can affect the navigation performance, potentially opening the door to new trajectory solutions. Current tools do not possess the capability for performing this task efficiently.

1.2. Background information and state-of-the-art

On-board GNC systems oversee estimating the state of the spacecraft and compare it with the planned trajectory, search for deviations and control the spacecraft accordingly. They are becoming more and more sophisticated. Their technology is rapidly advancing and autonomy is progressing, taking an increasingly wider role. Current developments are mainly focused on pattern recognition and tracking, as shown by Gil-Fernandez et al. (2016), Kicman et al. (2016), Pellacani et al. (2016), and Suatoni et al. (2016). However, autonomy is not total yet, and even less considering the highly uncertain environment, we are dealing with, thus the GNC system still depends on ground planning and commands for its correct functioning.

The flight dynamics system (FDS) is the system in the ground segment in charge of the mission control, planning of operations, and ensuring that the mission objectives are met. The FDS stands for its great adaptability to any situation and its higher precision. However, its performance is very limited due to the communications between the spacecraft and ground team, which worsens the overall quality of the navigation. A clear and steady evolution can be observed by reviewing the role that ground centres and autonomous systems have been undertaking in interplanetary spacecraft navigation; from the work by Miller et al. (2002), passing by Kawaguchi (2006) and Munoz et al. (2015), to the latest designs by Kicman et al. (2016). The most obvious evolution pattern is seen in the use of the available resources. Each system is operated in the circumstances where its performance is the strongest. Thus, their weaknesses are mitigated, and the overall navigation is improved.

This becomes critical when a spacecraft first approaches a small body that has not been visited before. The characterisation of these systems is done from Earth and yields very poor and uncertain results, as showed by Richardson et al. (2016). Small-body features, such as shape and mass distribution, are quite irregular. These irregularities are often completely unknown and remain so until the spacecraft approaches this kind of bodies. This time also corresponds with the time when the knowledge on these characteristics is needed the most. Thus, this uncertain environment has a heavy impact on the mission design, which must deal with these uncertainties.

This highly uncertain environment restricts the spacecraft to remain at remote distances during the first phases of a mission. Very long hyperbolic arcs are used to reduce the impact of the yet unknown dynamics on the orbit, as well as to reduce the number of manoeuvres. This was done for Rosetta and proved key for the safety and cost of the mission, as described by Herfort and Casas (2015). The data quality that can be gathered during these phases is still poor. Nevertheless, it is crucial to refine the model to a point where the spacecraft can safely come closer to the body.

Low-budget asteroid missions, such as AIM, often resort on removing the most expensive instruments on the Spacecraft. These instruments, in turn, use to provide the most precise and significant data. AIM will not be carrying neither an altimeter nor an steerable high-gain antenna. These two have proven key in former missions to asteroids for precise orbit reconstruction. Hence, new navigation alternatives must be found to compensate for the lack of these two elements. Navigation strategies, understood as how the different estimation techniques are combined to compute the spacecraft's state and the unknown parameters, for a highly uncertain environment will be assessed. An optimised use of resources, such as time, person-hours, and cost, and increased performance will be explored, so that the new navigation does not incur in additional costs which could cancel the saving effect of not carrying and developing these expensive instruments.

1.3. Navigation problem description

During the early characterisation phase of a mission to a small body, knowledge of the body is almost null. The estimation of the distance to the body needs knowledge on the body size and vice versa. A problem arises when only navigation cameras are used for orbit determination. The indeterminacy, as described by Godard et al. (2015), is due to the under-determination of the geometrical problem to be solved. Only a pair of parameters for each landmark is obtained from images taken by navigation cameras, but each landmark has three parameters to be estimated (three position coordinates). When several images at different epochs are acquired, a 3D distribution of landmarks can be determined.

Thus, the problem is solved in shape, as shown by Grieger and Küppers (2017), but not in size. However, if the distance between two positions at which the spacecraft has taken two images is known, the scale is determined. The same occurs for the spacecraft-asteroid distance. Without having solved the problem for scale, the distance remains unknown. This has traditionally been solved by absolute navigation, with radiometric measurements. But, these can only be taken when SC-ground communications are established, which, due to the lack of a steerable antenna, never occurs simultaneously with image collection. Since the spacecraft cannot point the camera to the asteroid and the antenna towards Earth at the same time, slew manoeuvres are executed in between these two attitudes and camera measurements and communications become mutually exclusive.

1.4. Research objectives

During asteroid interplanetary missions around small irregular bodies such as AIM, important dynamical parameters such as the target body's ephemerides, centre-of-mass and landmarks positions, and shape model, which are critical for the subsequent close-distance mission phases, are estimated. However, as it was stated before, the knowledge on these parameters is null and their estimation both not trivial and, in some cases, coupled. Having described the context of this work and the navigation problem to be addressed, a research question, to be answered by this project, is outlined:

How can we estimate the highly uncertain dynamical parameters, typical of small-body missions, whose accurate knowledge is key to safely navigate around these types of bodies at close distances?

These estimation processes are organised under navigation strategies, which integrate all parameters involving the complete estimation process. Thus, the research question can be reformulated to:

What navigation strategy delivers the best cost/performance for safe operations and the characterisation of the dynamics around small celestial bodies?

This question embeds many particular topics that should be addressed individually. These subquestions will be listed and further explained in Chapter 7.

The research on Navigation will be performed by defining a characteristic and innovative case study of the space missions in the project's scope, the Asteroid Impact Mission. Realistic ground-navigation performance models will be tailored by surveying former interplanetary mission designs and results. State-of-the-art algorithms for spacecraft navigation and mission heritage will also be implemented and used. All of this will be incorporated into a conceptual model that will be translated into a GNC software for computational analysis. Then, scenarios to test all hypotheses will be tailored. Quantitative performance comparisons between all hypotheses will be carried out. Analysis on these results will lead to updates on the conceptual model, which will be further tested.

Thus, navigation strategies will be probed and assessed by simulating their performance on a GNC-performance software, which will be designed and implemented.

1.5. Report structure roadmap

This report has been structured to be able to answer the research questions effectively. It is structured into three main blocks: a literature review, the software design and validation, and the navigation-problem analysis.

Firstly, the background on the work will be outlined in Chapter 2. Former asteroid missions that preceded AIM will be reviewed, together with their most relevant navigation problems which will be present for AIM as well. This will help establish a set of navigation issues and ways to approach them.

The modelling of the to-be-simulated system will follow. The dynamical model will be described together with the most relevant force-models that are to be used in its construction in Chapter 3. After the dynamics, in Chapter 4, AIM's sensors and how their measurements are modelled are depicted. The chosen navigation filter, which will constitute the core of the simulations, will be deeply described with all its particularities and the possible ways in which they will influence the navigation. The manoeuvre computation algorithm and its error model will end this first system-modelling part in this report.

This aforementioned problem is to be analysed in a computer simulation. Thus, the selected numerical models that will be used, e.g., numerical integration and derivation methods, will be described in Chapter 5. The design of the complete software framework will follow in Chapter 6. Its architecture and functions will be schematised and described. A functional division will be provided together with the interface description of the identified items in the software. Then, the validation and verification plan and its execution will be reported. The most relevant tests on which the software validation was carried out will be depicted.

Then, the analysis on the navigation, the core of this Thesis work, will follow in Chapter 7. Having gathered all the previous information, the research question will be decomposed into more manageable questions, which are to be answered individually. The particularities of the field of study will be analysed and ways to approach them will be discussed. The analysis scenarios will be set up and their

assumptions will be stated. All this information will provide a plan-of-attack on which the simulations will be based. Having prepared the simulations accordingly, their results will be presented and discussed in Chapter 8. These discussions will lead to answers to the research questions, which will be eventually converted into a navigation strategy.

Finally, this report will end with the discussion of considerations that can be extracted from the present work in Chapter 9. Conclusions will be stated and discussed. Future implications of the current work will be identified to highlight the working areas that open after this MSc. Thesis Project.

Chapter 2

Mission Heritage and Mission Requirements

During the past decades, interest in asteroids and other kinds of small bodies, such as comets and small moons, has been growing. The progress in technology has also been helping make space missions to this kind of bodies possible, as well as expanding the interplanetary-mission capabilities.

In this chapter, former missions to these bodies will be reviewed, together with their advancements in navigation. Two key asteroid missions, the NEAR-Shoemaker and Hayabusa, will be reviewed, due to both being direct precursors of the Asteroid Impact Mission (AIM), in terms of the similarity of the target bodies, as De León et al. (2010) describes. The Rosetta mission will also be reviewed, since the navigation technology developed for that mission will be directly adapted for AIM, which makes Rosetta become the parent mission of AIM.

This chapter will end with a review of the AIM mission itself. This will help write what requirements can be set for this MSc Thesis, as well as the constraints at which this work is delimited.

2.1. NEAR-Shoemaker

NEAR Shoemaker, where NEAR stands for Near Earth Asteroid Rendezvous, was a NASA mission whose main objective consisted on orbiting a Near Earth Asteroid (NEA), Eros. It was launched in the late 90s, and after a miss-burn and some corrections, it made a rendezvous with Eros, in February 2000. The NEAR spacecraft was inserted in a circular 350-km orbit around the asteroid. After a series of propulsive impulses, the size of the orbit was reduced to 50 km and 35 km. It was from these orbits that NEAR Shoemaker did the complete characterisation of the Eros asteroid. Landmark position and ranging determination allowed this.

Once the mission came to an end, the NEAR spacecraft was landed on the surface of Eros for its decommission. The landing was planned to maximise the survival chances of the SC. However, this was not a design constraint, and it only came as an option, once the decommissioning phase was being planned. Finally, NEAR was deposited on the surface of Eros, and telemetry was gathered during several days. This allowed reconstructing the most possible orientation on which the SC was resting on the asteroid.

2.1.1. Mission Overview

As Miller et al. (2002) described, due to the power constraints, the orbit of NEAR was always maintained almost perpendicular to the Sun direction. This helped avoid eclipses, while ensuring that the phase angle, understood as the angle between the Sun direction and the SC direction to the asteroid, representing a measure of illumination, did not vary along the orbit. The inclination of Eros' rotation axis and the irregularity of its shape caused that its south pole was not seen at NEAR's arrival. These aspects caused that the complete characterisation of the system needed half an orbital revolution for its completion. At arrival, the north pole was the main illuminated region, thus the mission started with its characterisation. The equatorial areas followed, and then, when the south pole was for the first time illuminated, after half an orbital revolution, its characterisation commenced.

NEAR disposal, as depicted by Williams (2002), was designed so that the SC would rest in the surface of EROS. The spacecraft was put out of its circular 36-km orbit until it entered the final descent phase at almost five km over Eros. The antenna was kept pointing Earth while the cameras pointed nadir. This allowed for a continuous tracking of the descent phase. The remaining manoeuvres were executed to keep this pointing attitude and reducing the impact velocity.

2.1.2. Spacecraft Systems

The NEAR spacecraft was designed aiming for simplicity. No moving parts were included. All sensors and solar arrays were placed on fixed positions, those seen in Figure 2.1[1], limiting the functional attitudes in which the SC could carry on gathering scientific data. The phase angle, angle between nadir and the Sun direction, was always limited to a 30-degree maximum. For communication with Earth, the spacecraft had to do attitude manoeuvres to point the antenna to Earth. This required very precise attitude control. Four reaction wheels controlled the spacecraft's pointing. NEAR also mounted a laser-ranging altimeter, which proved key for the asteroid's shape reconstruction and orbit determination.

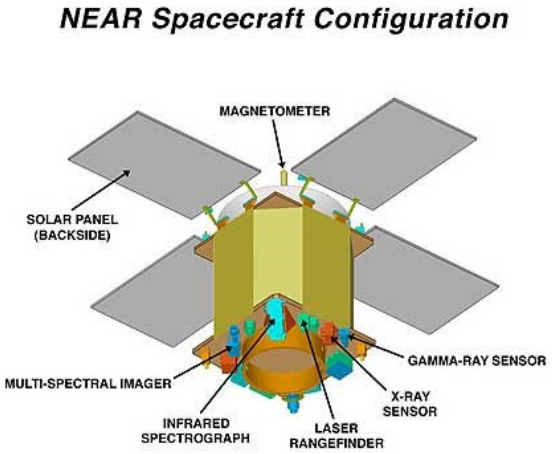

Figure 2.1: NEAR spacecraft by

2.1.3. Navigation Techniques

NEAR's orbits around Eros were used to obtain estimates of the force environment around the asteroid. The trajectories were reconstructed using radiometric data, such as range and Doppler measurements, as Scheeres (2002) described. Optical images were used to determine landmarks. These observations were divided into 30-day arcs for which a Square Root Information Filter was used, as shown by Miller et al. (2002). This filter was designed to estimate up to 800 parameters and 18 stochastic variables.

[1]Extracted from http://www.aerospace-technology.com/uploads/project/near/images/near_spacecraft4.jpg on March 26, 2017

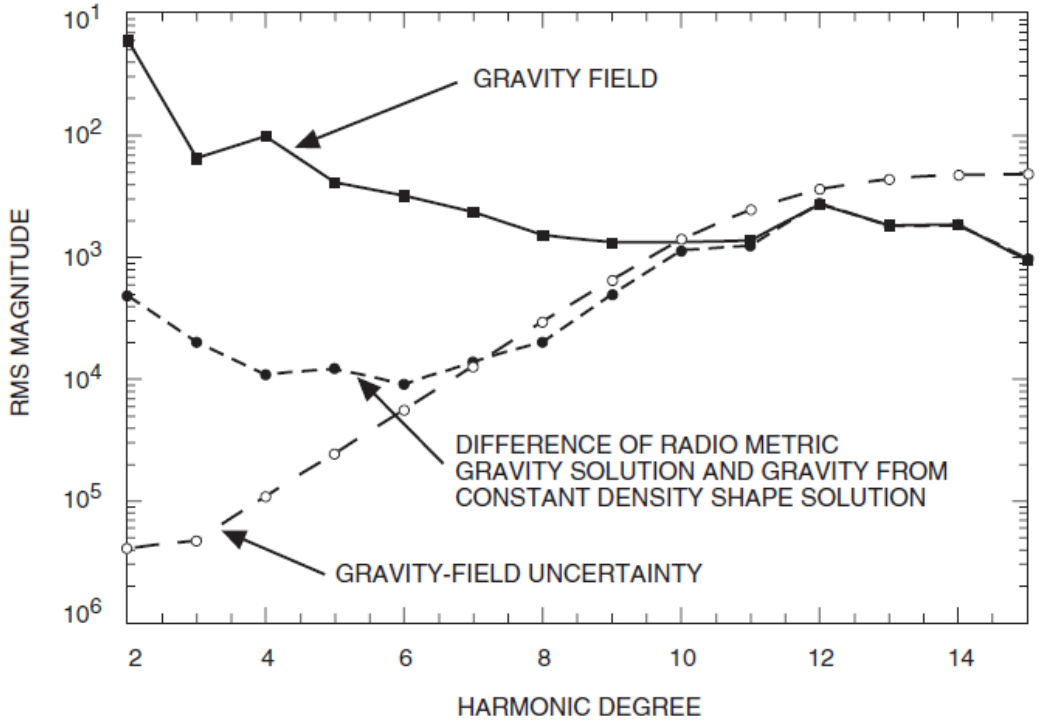

Figure 2.2: Comparison between the estimated gravity solution (from ODP) and the constant-density shape (from PCODP) model by Scheeres (2002)

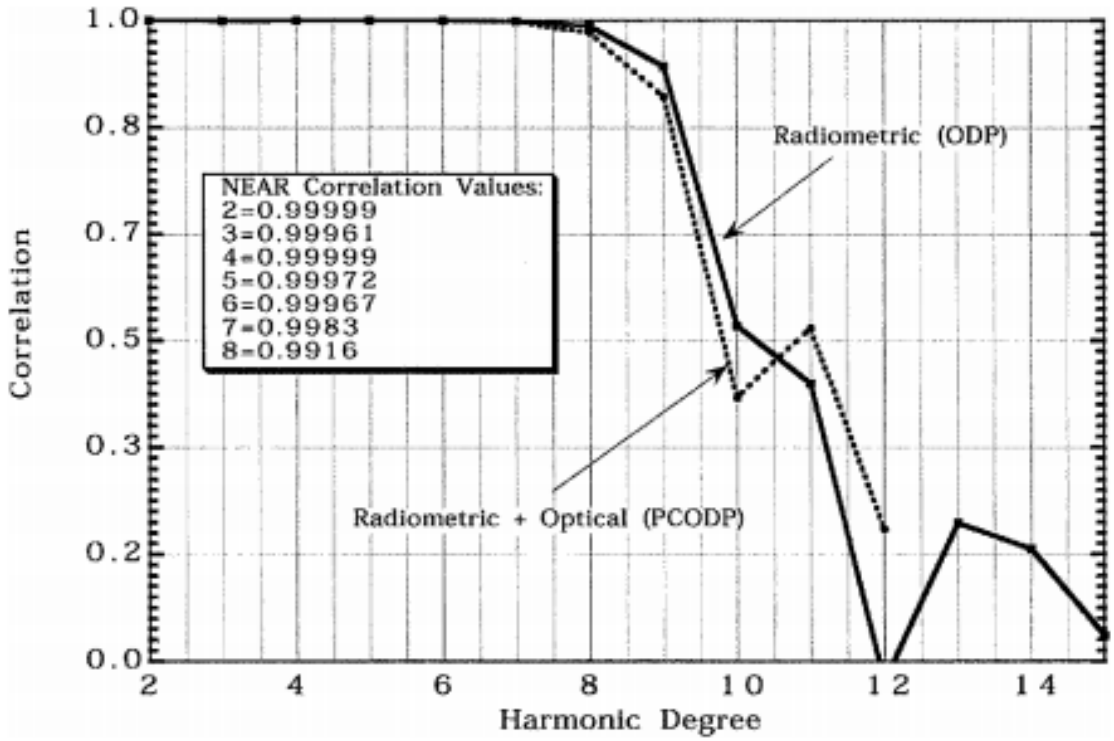

Figure 2.3: Correlation between the estimated gravity solution (ODP) and the constant-density shape model (PCODP) by Miller et al. (2002)

Among the estimated parameters, the environment of Eros was included. Some of them were the ephemeris, rotational state, spherical harmonics up to 12 degree, inertia tensor, etc. The inertia elements were estimated by detecting wobbling on the principal axes. The convergence of the filter required that the first arcs contained only a few days. Once a solution was found, it was fed back into the filter, and a longer arc was solved for. Then, several-day batches were introduced until all information was processed. This process provided the best data for processing the laser ranging measurements.

Altimetry measurements were used to compute a 3D model or Eros. This model, when a uniform density is considered, was compared to the radiometric gravity solution, as shown in Figure 2.2 and Figure 2.3. The gravity field of Eros was characterised using a spherical harmonics expansion by Scheeres (2002). A solar-pressure-force model was included in the estimation, for which 12 different parameters for a multiple-surface discretisation was used. Nevertheless, this solution (PCODP), limited to 30-day arcs, did not provide enough precision for the spherical harmonics. A second Square Root Information Filter was used (ODP), for which no optical data was included. This method provided a more accurate solution with a higher number of spherical harmonics. A comparison between both models is shown in Figure 2.2 and Figure 2.3.

The solution for the gravity field, which was expressed in a Lagrange spherical harmonics expansion, did not provide a very accurate solution. This was due to Eros' shape. Its high irregularity and its elongated shape causes that, for a high order spherical-harmonic representation, the solution is not representative of the actual gravity field. This was observed when the noise of the estimated coefficients was compared against the estimated values. From 10^{th} degree upwards, the RMS of each coefficient is of the order of its estimate, as depicted by Miller et al. (2002).

2.2. Hayabusa

Hayabusa was an interplanetary mission by JAXA, previously named MUSES-C, whose objective consisted on delivering an asteroid sample to Earth. It involved an entirely new challenge for GNC technology, since the spacecraft had to land on the asteroid, collect a sample, and then return it to Earth. This set the mission goal of developing and demonstrating the key technologies for future exploration missions to small bodies in the Solar System.

Hayabusa involved other key technological challenges such as:

- The use of ion engines for interplanetary cruise as the main propulsion.
- Autonomous navigation and guidance using the optical images gathered by its navigation cameras.
- Collection of asteroid samples in a micro-gravity environment.
- The use of interplanetary fly-by's together with low-thrust assistance.
- Usage of the ion engines for reaction wheel desaturation.

Those were not the only technological challenges that Hayabusa faced. Others were low-thrust bi-propellant attitude thrusters, lithium-ion batteries, multi-junction solar cells, X-band up, and down-link, among others. Nevertheless, Hayabusa's most interesting aspect for this review was the descent and landing on Itokawa.

2.2.1. Mission Overview

Hayabusa made a rendezvous with the asteroid Itokawa on August 28, 2005. From there, the spacecraft started approaching Itokawa in a 3-month scheduled descent. This approach made use of the relatively weak asteroid gravity at far distances. Hayabusa was always kept on the Earth-asteroid line due to a constraint in its design, it carried a fixed high-gain antenna. This solution was taken to ensure that asteroid operations could be done at the same time that communications were estabilised. Its initial distance to the asteroid was 20 kms. One month after insertion, by the end of September, the spacecraft had reduced its distance to 8 km.

Since the descent was being done on a straight line, no accurate physical estimation of Itokawa was being done. Thus, a partial orbit was planned. At 3 km from Itokawa's centre of mass, Hayabusa engaged in a partial revolution that allowed the navigation teams estimate the gravity field and the solar radiation pressure.

Once this first characterisation and recognition of Itokawa was finished, two touchdown attempts were performed. These were preceded by several descent rehearsals. These descents and landings were partitioned into two phases, a descent phase, and a vertical descent phase. The transition between them two was scheduled at 500 metres altitude above the asteroid.

2.2.2. Spacecraft Systems

A schematic representation of Hayabusa is shown in Figure 2.4. The Hayabusa spacecraft contained two different propulsion systems. It used both chemical, 12 20N-thrusters for attitude and high-thrust manoeuvres, and an electric propulsion engine as the main propulsion method for deep-space manoeuvres.

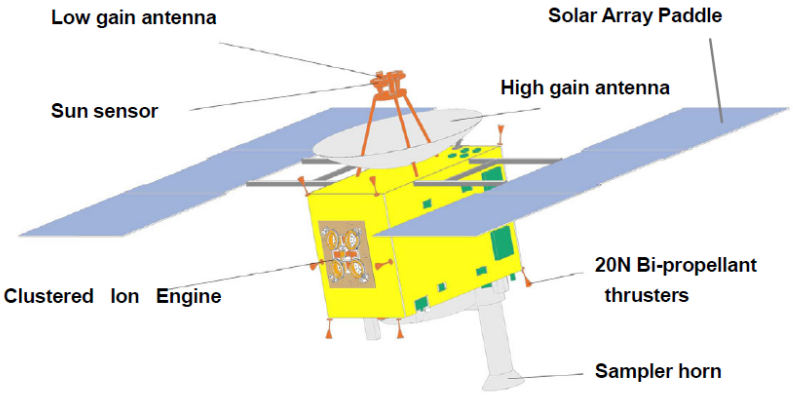

Figure 2.4: Hayabusa spacecraft by Kominato et al. (2006)

As it happened for NEAR, Hayabusa carried only fixed instruments. As Kominato et al. (2006) describes, Hayabusa mounted two different navigation cameras: a narrow-angle camera (NAC), for asteroid mapping and scientific observations, and a wide-angle camera (WAC), for on-board navigation. A laser range finder (LRF) and a LIDAR were included, as well as in NEAR Shoemaker. A star tracker was used for inertial attitude determination, but for some applications were the attitude of the spacecraft made the navigation cameras point away from the target, it was used as an extra navigation camera. The high-gain antenna was fixed to the spacecraft and opposed to the side on which the sampler was located. This configuration causes the trajectory design to lie between the Earth and Itokawa, so communications can always be established while all instruments point towards the asteroid. Thus, this constraint was solved by restricting the trajectory, as opposed to NEAR, which solved this problem by slew manoeuvres.

2.2.3. Navigation Techniques

Hayabusa was mainly navigated using his on-board LIDAR. It provided slant range measurements that allowed a precise estimation of its distance to Itokawa, as well as, a complete 3D model of the asteroid. The navigation cameras were mainly used for centroid recognition. This allowed Hayabusa keep its attitude pointing with respect to the asteroid. Ground-based navigation used radiometric measurements and Doppler for the estimation of the absolute position. Images taken by the navigation cameras were processed on-ground. Landmark recognition was done manually by an operator, as Takeishi (2013) described. This process is depicted in Figure 2.5.

As described by Shirakawa et al. (2006), this procedure was very costly in both time and effort. Landmarks were identified on a single image and their movement was tracked on the following pictures.

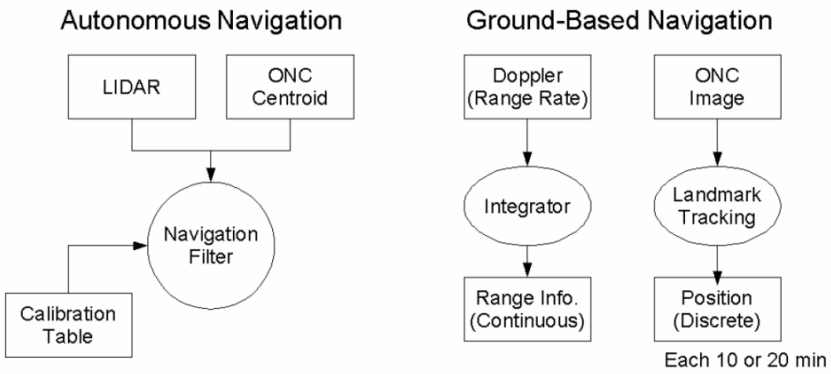

Figure 2.5: Hayabusa's navigation schematic for distances larger than 500 m, by Shirakawa et al. (2006)

Hayabusa, as described by Kawaguchi (2006), used an extended Kalman filter for its on-board navigation and a Feed-Forwards control scheme. The filter estimates the state of the spacecraft relative to the asteroid. It used a combination of different sensors, depending on the mission phase. LIDAR measurements were used for almost all the descent, while the LRF was used only during the last metres, for the shortest distances.

2.3. Rosetta

Rosetta is an ESA mission to the comet 67p/Churyumov-Gerasimenko. The mission is named after the Rosetta stone, an Egyptian plate with carved text in old Greek and hieroglyphic Egyptian writing, which allowed the translation of all hieroglyphic writing in Egypt. The Rosetta mission had the main objective of characterising a comet's nucleus. It was meant to study the morphology and composition of comets, as well as, the volatiles that are expelled out from the nucleus; thus, the formation of a comet's coma could finally be studied.

2.3.1. Mission Overview

The Rosetta mission's launch was first planned to take place in January 2003, the destination comet was 46P/Wirtanen. However, the launch was delayed, and the launch window to that comet was missed. Thus, another candidate was searched by ESA, and 67P/Churyumov-Gerasimenko was selected. Its launch finally took place on March 2nd, 2004. Several gravity-assist manoeuvres were performed. Rosetta had the unique opportunity to test its navigation with two asteroid encounters: Steins and Lutetia.

2.3.2. Spacecraft Systems

As Munoz et al. (2015) described, the Rosetta spacecraft mounted two long steerable solar arrays, which allowed the spacecraft to operate at distances of three AU from the Sun. For further distances, the spacecraft had to enter a state of hibernation, where almost all power was dedicated to keep the spacecraft's temperature. It also mounted a high-gain steerable antenna, which allowed for simultaneous science operations and communications, unlike the two previously analysed missions. Rosetta also mounted numerous scientific instruments, such as optical cameras, gas and particle detectors, and radio/microwave instruments.

Rosetta carried a small lander called Philae. This lander had two harpoons. These were fired once the landing had occurred, so Philae could attach itself to the comet's surface. These harpoons are believed to have not worked, which caused Philae to rebound several times on the comet's surface. The contact with Philae was lost and it could never be recovered.

Rosetta was equipped with the following sensors and actuators:

- One inertial measuring unit (IMU) with three ring-laser gyros and three accelerometers.
- Four reaction wheels.
- Two star trackers.
- For propulsion: 24 10N bi-propellant thrusters, 8+8 for attitude control, and 4+4 for translational motion.
- Two navigation cameras (NAVCAM)
- The instrument OSIRIS that contains a NAC and a WAC.

Table 2.1: Rosetta's navigation cameras, by Herfort and Casas (2015)

	NAVCAM	NAC	WAC
Sensitivity	11 mag	>15 mag	>15 mag
Field of View	5x5 deg x deg	2.2x2.2 deg x deg	11x11 deg x deg
Pixels	1024x1024	2048x2048	2048x2048
Resolution	12 bits/px	16 bits/px	16 bits/px

2.3.3. Navigation Techniques

As it has been described in Subsection 2.3.2, Rosetta mounted two navigation cameras (NAVCAM) and two extra cameras in the instrument OSIRIS. These cameras took images of the comet. Since the main objective of the navigation was to estimate Rosetta's relative state w.r.t. the comet, the main source of data comes from landmark tracking. Landmarks had to be first identified and to allow their tracking. This identification process was done by a human operator on the Earth. It was observed that the identification could be done with sub-pixel precision. Then, landmarks were subsequently using the images sent by Rosetta. A summary of Rosetta's cameras is shown in Table 2.1

However, landmark tracking only retrieves two measurements per landmark and observation. This is not enough for the complete determination of the SC's state. The scale and orientation have to be solved for yet. This will be an important objective of this MSC Thesis, thus an extensive explanation will be carried out. Nevertheless, this indeterminacy was solved for Rosetta by using range and Doppler measurements, thanks to Rosetta's steerable HGA, which allowed for these measurements to be obtained at the same time the pictures are being taken.

First the spacecraft's orbit is solved using these measurements, and then, the landmark tracking is incorporated to obtain the relative state. A schematic of how the relative and absolute states are related to each other is shown in Figure 2.6. This estimation process used a Square Root Information Filter, which included the estimation of many forces acting on the spacecraft, such as coma drag, the gravitational potential of the comet, solar radiation pressure, and third body effects. The estimated values for these forces are depicted in Figure 2.7.

Since the centre of mass of the comet is set as the centre of the gravitational force, the first-degree spherical harmonic coefficients. C_{10} S_{10} and C_{11}, can be set to zero. The second-degree coefficients can be expressed as a function of the components of the comet's inertia tensor. Thus, once the orbit determination process manages to give estimates of these coefficients, this information can be used to solve for the scale of the inertia tensor, together with the measured wobbling of the rotation axis.

Rosetta, unlike Hayabusa and NEAR Shoemaker, did not carry an altimeter. Thus, the shape reconstruction and navigation had to be done using only information coming from the navigation cameras. For shape reconstruction, two main techniques were used, as explained by Pardo De Santayana and Lauer (2015). On the first hand, the surface was characterised using maplets. Maplets are 3D high resolution maps centred on a Landmark. They are obtained from the images of the narrow-angle cameras. A technique called stereophotoclinometry was used. It consists on translating the greys in an image into slopes, and then, the slopes are integrated into heights.

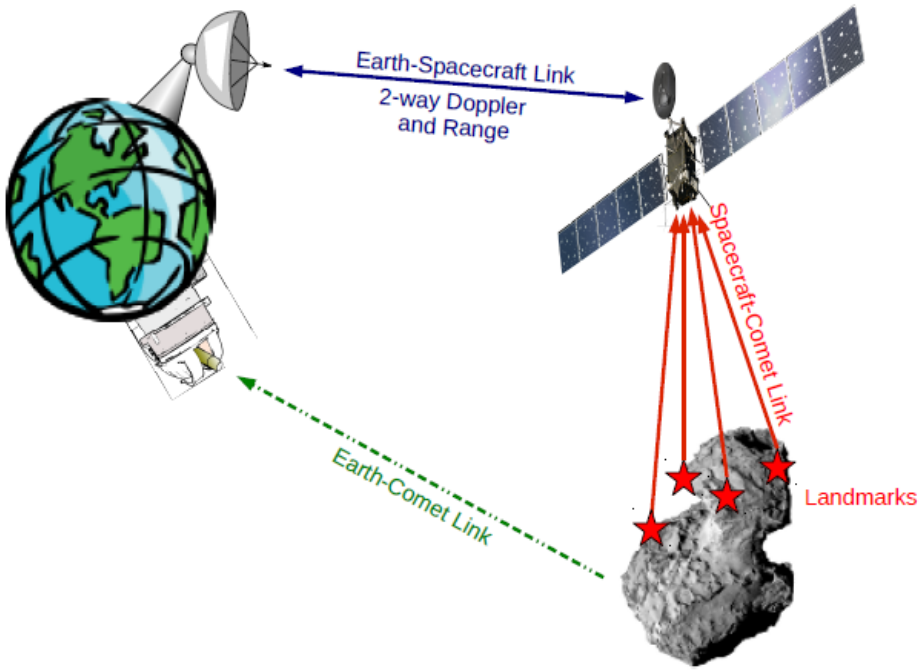

Figure 2.6: Schematic of the link between the relative and absolute navigation, by Godard et al. (2015)

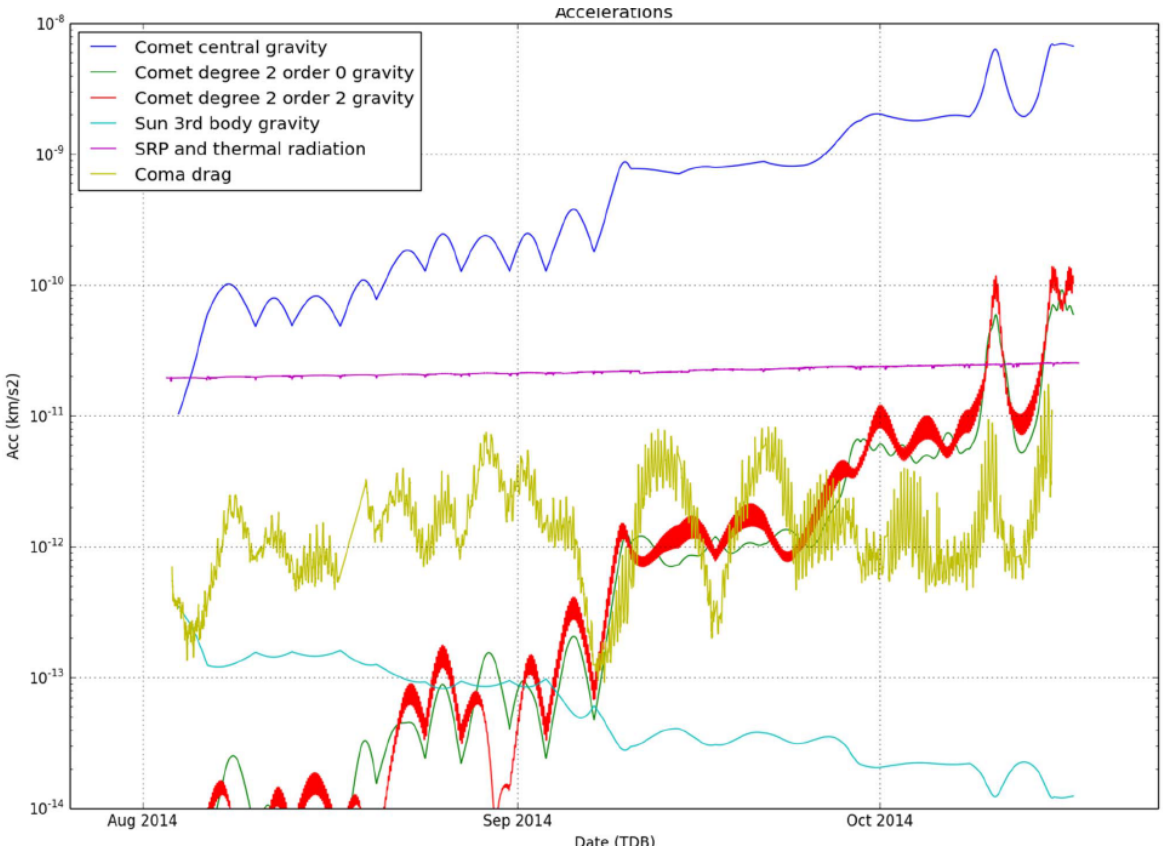

Figure 2.7: Accelerations acting on Rosetta in the vicinity of 67P-Churuymov-Gerasimenko as shown by Companys (2015)

On the other hand, the overall shape model of the comet was computed using a silhouette carving method. This method consists on removing chunks of a model bigger than the comet's, using the navigation images. It requires very long times for a proper shape reconstruction, and, since the south pole was not illuminated during the first months of Rosetta's characterisation phase, the shape model of those areas took a longer time to be produced. Then, the maplets are mounted on the silhouette-carving 3D model. This yields a highly precise shape model, which for most navigation applications is not used, due to the increase in memory and CPU usage.

2.4. Asteroid Impact Mission

The Asteroid Impact Mission (AIM) is an ESA S-class mission that will fly to the binary asteroid system Didymos, formed by Didymain and Didymoon. The main mission objectives are to demonstrate new technologies for deep space missions and planetary defence, as well as scientific observations of a binary asteroid system.

Thus, three mission objectives can be extrapolated.

- Technology demonstration
- Asteroid scientific exploration
- Contribution to the Asteroid Impact and Deflection Assessment mission (AIDA)

The AIM mission is part of the joint AIDA mission, by ESA and NASA, where NASA is participating in the mission with the the Double Asteroid Redirection Test (DART). DART's main objective is to send an kinetic impactor to Didymoon and observe the consequences of this impact on the dynamics of Didymos. DART's arrival is currently set to October 2022. Thus, AIM will have the important objectives of characterising Didymos prior and post the impact of DART. Thus, its arrival is scheduled to take place earlier in May 2022, so that, in the intermediate months, AIM will have enough time to carry out an extensive characterisation.

2.4.1. Spacecraft Systems

AIM is currently undergoing an extensive remodelling and redesign, due to budget cuts caused by the outcome of the last ESA Ministerial Council in Lucerne, 2016. The design is being iterated to fit the new financial constraints. Current data for the old SC model, as per [AD01], are shown Table 2.2. Due to budget constraints and the low-cost philosophy of the AIM mission, the spacecraft was designed so that the navigation is purely done with navigation cameras, thus, no altimeters were included. This decision will have a direct impact on the navigation strategy design of AIM and will differentiate this mission from all its predecessors, excepting Rosetta. However, unlike Rosetta, AIM's high-gain antenna is not steerable. Thus, slew manoeuvres must be executed to establish communications. This does not allow simultaneous operations and communications, which imposes a heavy constraint on the navigation.

2.4.2. Mission Design

The AIM mission schedule prior to DART's arrival has been divided into seven phases. All data is extracted from [AD01]. These phases range from large distances to the asteroids, for first system characterisation, to low orbits for cubesat insertion.

Among these phases, the one that concerns this project is the Early Characterisation Phase, or ECP. The main objective of the ECP is to provide the ground teams with a first approximation to the dynamics around Didymos. These data are crucial for safe navigation and unlock the following phases by giving the first in-situ estimation of parameters such as the gravitational parameters of Didymain and Didymoon, thus providing the necessary data to construct all trajectories.

The ECP is comprised of four hyperbolic arcs around Didymos. The hyperbolic arcs are selected so that the highly unknown dynamics of Didymos would impact AIM's trajectory as minimum as possible while performing the characterisation. Thus, it was selected that during the entire phase, AIM's velocity will never fall below twice the local escape velocity. The complete duration of these arcs is 14 days,

Table 2.2: AIM SC System's Summary as per [AD01]

Sensors	
Camera	FoV 5.5 deg 1024x1024
Altimeter	None
Thrusters	
Thrust with 6 DoF	2 x 10N (translation) 8 x 10N (RCS) Isp 240 s
Thruster error models (3σ)	3% magnitude 1º direction
Other	
Solar array	area of ~5 m2
Total mass @ Proximity Operations	503 Kg
Antennas	one fixed HGA one backup fixed MGA two LGA (providing omnidirectional capabilities)
Star tracker (STR)	DTU μASC NEA: 2.5 arcsec (2σ) Measurement rate: 2Hz
IMU	Northrop Grumman LN200-S ARW: 0.07 deg/√Hz Measurement rate:10Hz
Reaction wheels (RW)	MSCI MicroWheel Maximum Torque: 0.03Nm Momentum Storage: 1.1Nms
Coarse Sun sensor	Moog Bradford
Battery	8S6P ABSL 18650 NL battery (incl. redundant string) – 30min energy

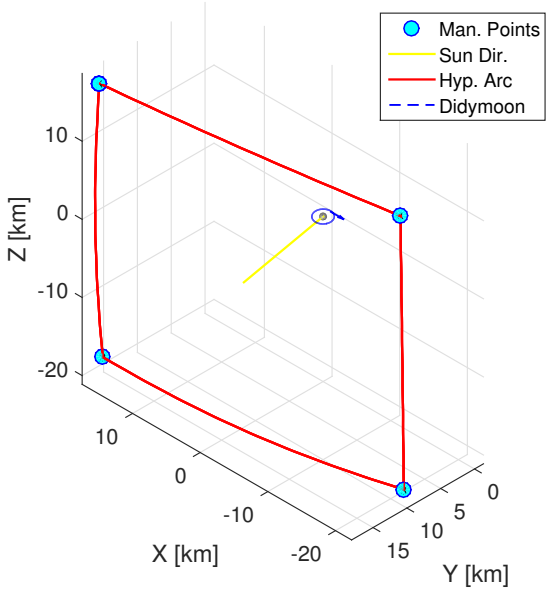

Figure 2.8: Four ECP Hyperbolic arcs as per [AD01]

of which, two of them will be 4 days long, and the two remaining arcs 3 days each. These will be interchanged, so that the complete duration of two arcs is 7 days, which perfectly fits the duration of a week, thus, scheduling will be easier and cost efficient for the ground operations centre.

During this phase, it was required that both Didymain and Didymoon could always fit inside the field of view (FOV) of the camera. To satisfy this constraint, AIM shall remain at altitudes higher than 24.5 km over Didymain, due to its 5.5º FOV of its navigation camera. For optimal illumination, needed for science and navigation, the phase angle, understood as the angle between the Sun direction and the SC position w.r.t. the asteroid, must be always remain below 70º and above 20º.

The current design iteration of the early characterisation phase complies with the above exposed constraints. Thus, it will be the base on which the navigation analyses for this MSc Thesis will be carried out. The four arcs that compose this phase are depicted in Figure 2.8. The trajectory is shown together with Didymain and Didymoon and the manoeuvre points. The Sun direction is also shown so that it can be observed, both in this figure and also in Figure 2.9b that the phase angle is always below the 70º limit, thus, AIM will always observe the illuminated hemisphere of Didymain. In Figure 2.9a, the range to Didymos is plotted for the complete phase, showing that for almost all the duration of the phase AIM will be further than 24.5 km to the asteroid. Thus, Didymain and Didymoon could be observed simultaneously. In terms of the velocity excess, in Figure 2.9c and Figure 2.9d, it is shown that for all four arcs the velocity excess condition is met.

2.5. Mission Constraints and System Requirements

The main objective of the Asteroid Impact Missions, as described by Cheng et al. (2015), is to determine the geophysical properties of the primary and secondary component of asteroid Didymos.Michel et al. (2016) listed what properties shall be estimated and its accuracy. This includes the shape, mass, density. In addition, the dynamical state of the asteroid shall be analysed (period, orbital pole, spin rate, and spin-axis). Cheng et al. (2015) also described the secondary objectives of the mission. However, all of them are related to the geophysical characterisation of the asteroids and post-DART observations. Thus, those objectives are not relevant for this study. For the scenario definition of the AIM mission, to be analysed by the software to be developed, described in Chapter 6 Software Framework, the most challenging phase and that of interest for this project, the Early Characterisation Phase (ECP), is selected. The navigation analysis on this phase will provide several important outputs:

- Feasibility of the navigation strategy
- Optimal system selection for cost/performance
- Optimal interface point between FDS and GNC
- Navigation performance

2.5.1. Mission Constraints

The constraints on the AIM mission are be related to the operations, geometries, and the low-cost philosophy of the mission. These constraints will have a direct impact on the navigation performance, thus they must be carefully. Specifically:

MC-AIM-01 Communication Windows A communication link can only be set if there is direct visibility between one of the identified stations for the mission and the SC, without any blocking object, and with the Sun at a higher angular distance than the identified solar exclusion angle.

MC-AIM-02 Minimum time between Manoeuvres The minimum time between manoeuvre using standard operations is 3 days. This time is decreased to 1 day for critical operations at the expense of increased operational costs. Furthermore, it possible to upload several manoeuvres at once to the SC but this has a negative impact at the level of the manoeuvre correct computation for the later manoeuvres as it will be based on outdated navigation information. This is also valid for the upload of the attitude profiles.

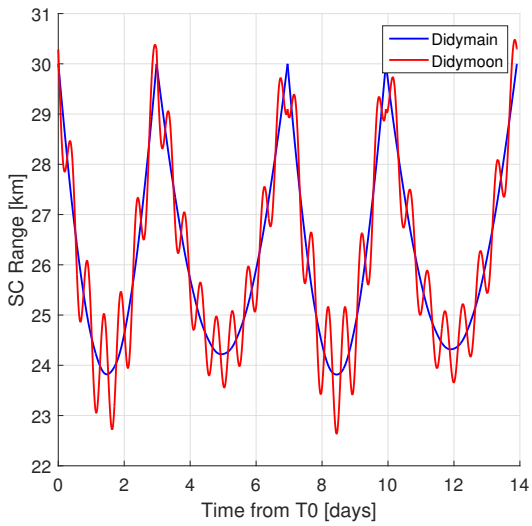

(a) Range to Didymain and Didymoon

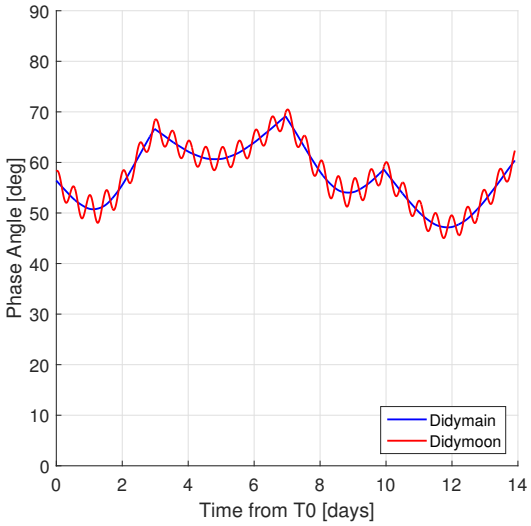

(b) AIM's ECP Phase angle

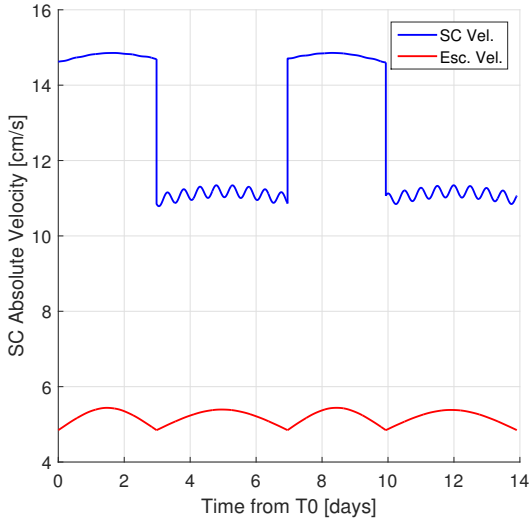

(c) Velocity w.r.t Didymain

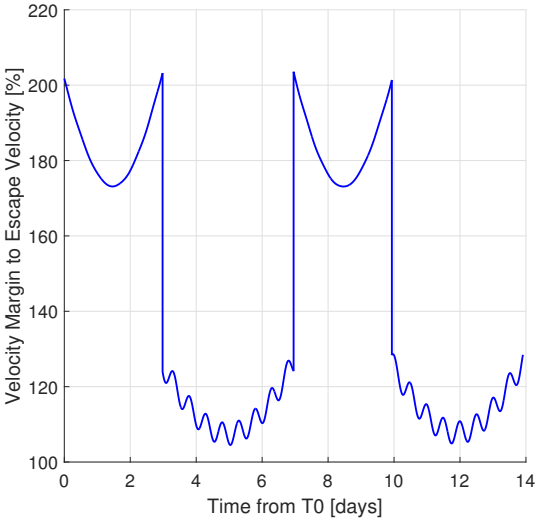

(d) Velocity excess in %

Figure 2.9: AIM's Early Characterisation Phase as per [AD01]

MC-AIM-03 No more than 30 minutes without direct sunlight The batteries in the AIM SC were designed to last only 30 minutes long without any power input. Thus, it is important that the SC will not be eclipsed by more than 30 minutes.

MC-AIM-04 Fixed High Gain Antenna (HGA) A fixed HGA will be responsible for communicating with Earth. This means that a slew manoeuvre is required each time to change between target point and Earth pointing modes. Science and communication modes cannot be engaged at the same time.

MC-AIM-05 Safety The AIM mission is quite challenging at the navigation and guidance levels and, thus, for increased safety the nominal trajectory shall never been in dangerous of colliding with either Didymain or Didymoon and its velocity should always be above the escape velocity at least with a 40% margin and a 100% margin in ECP.

2.5.2. Feasibility Parameters

The mission feasibility performances parameters are defined that will dictate if a navigation strategy is feasible or not. Furthermore, these parameters are also used in the search for the optimal cost/performance. For the AIM mission these are defined as:

FP-AIM-01 Didymoon Mass Estimation One of the AIM objectives is to characterise the DART impact. To do so, an accurate measurement of the moon's mass is required, as explained by Grieger and Küppers (2017).

FP-AIM-02 Safety The safety must be ensured at all time by, first, having its navigation and dispersion performance be well within safe margins and second, have its attitude performance ensure the correct follow up of targets as needed to ensure that there is no risk of losing the required bodies necessary for navigating the SC.

FP-AIM-03 Operational and Development costs Another crucial consideration is the mission cost, as each mission will have an available budget that must be met if the mission is to become a reality.

FP-AIM-04 Mass and ΔV Another important consideration is the mass. The considered systems plus the required propellant mass cannot surpass the maximum launch mass for the mission. In AIM, the proximity operations tend to spend little ΔV, however, this is a low-cost mission with very restricting mass constraints.

FP-AIM-05 Science return The science return, in quantity (data volume) and quality (coverage and resolution), is another important performance factor as in a science mission the characterisation of the dynamical system is also important and a good delivery of the SC on this side will result in better results for the scientific objectives.

2.5.3. Requirements List

Thanks to the previously described mission constraints and feasibility parameters a list of requirements for the AIM mission can be worked out. These describe the relevant requirements on the AIM mission that this MSc Thesis will be dealing with. Nevertheless, another list must be made to translate these previous requirements to a more manageable list, which has a direct impact on present work.

Mission Requirements

REQ-AIM-01 The AIM spacecraft shall never fall in a collision course trajectory with any of the two components of the Didymos system.

REQ-AIM-02 Time between two manoeuvres shall never be shorter than four days.

REQ-AIM-03 Sufficient illumination and viewing conditions of the Didymos system shall always be ensured.

REQ-AIM-04 The AIM spacecraft shall never be eclipsed by any of the components of the system due to power availability constraints.

REQ-AIM-05 The length of communication windows shall permit the complete downlink of all science data during the science-gathering periods.

System Requirements

REQ-SYS-01 The AIM spacecraft shall describe hyperbolic arcs in the Didymos system.

REQ-SYS-02 The minimum duration of ECP arcs shall be limited to three days.

REQ-SYS-03 The operational schedule shall be divided into natural Earth-days.

REQ-SYS-04 AIM's velocity shall never fall below twice the local escape velocity.

REQ-SYS-05 The phase angle shall always be between 20 and 70 degrees for optimal centroid and landmark navigation.

REQ-SYS-06 The mass of Didymoon shall be determined with a 3-sigma accuracy of at least 10%.

REQ-SYS-07 The AIM SC state shall be known with an accuracy of 300 m and 1 mm/s, with a 3-sigma confidence level.

Chapter 3
Astrodynamics

In this chapter, the physical models to be used in the modelling of the SC dynamics around Didymos will be described. First, in Section 3.1, the frame transformations between all reference systems in use will be described, and these systems will be listed and characterised. Second, in Section 3.2, the variables that will compose the SC state will be presented. Last, the complete model for the SC dynamics around Didymos will be described in Section 3.3.

3.1. Frame transformations

Here in this section, the frame transformations used for the conversion between two frames of reference will be listed. These frame transformations are needed to operate quantities expressed in different frames of reference. There are several ways to mathematically describe these transformations; among them are: the direction cosine matrix, Euler Angles, quaternions, Rodrigues parameters, and the Gibbs vectors. However, many of these frame transformations have a singularity for a certain rotation. This singularity is not present for quaternions and the direction cosine matrix.

Direction Cosine Matrix (DCM) represent the projection of the coordinates of one reference frame into the other. It takes the form of a matrix, which can be used to directly operate vectors. Its easy construction and its operability makes it the preferred solution to describe the attitude transformation between most systems.

Euler Angles can represent frame transformations by a set of at most three consecutive rotations. The order of these rotations and the axis around which they are performed determine the charter of the complete rotation. Their implicit physical meaning makes them useful for representing the direction of rotational axes, and the rotation about them.

Quaternions are a set of four quantities, three of which are linearly dependent, that describe the rotations between frames. They have been long implemented for asteroid missions for describing the attitude of SC, as shown by Munoz et al. (2012), Godard et al. (2015), and Johnson and Matthies (1999).

Two reference frames can be totally described by three linearly independent vectors, which are called basis vectors. These vectors are often defined as a set of three orthonormal vectors, but this is not a necessary condition for them to be considered basis vectors, a depiction of this is shown in Figure 3.1 [1]. For a three-dimensional space, any vector in a frame of reference can be described as a linear combination of the basis vector of that frame. These are called the components of a vector.

[1] Extracted from https://qph.ec.quoracdn.net/main-qimg-1c6b0ecacab9c7ba93762882626889a1 on 20th of March 2017

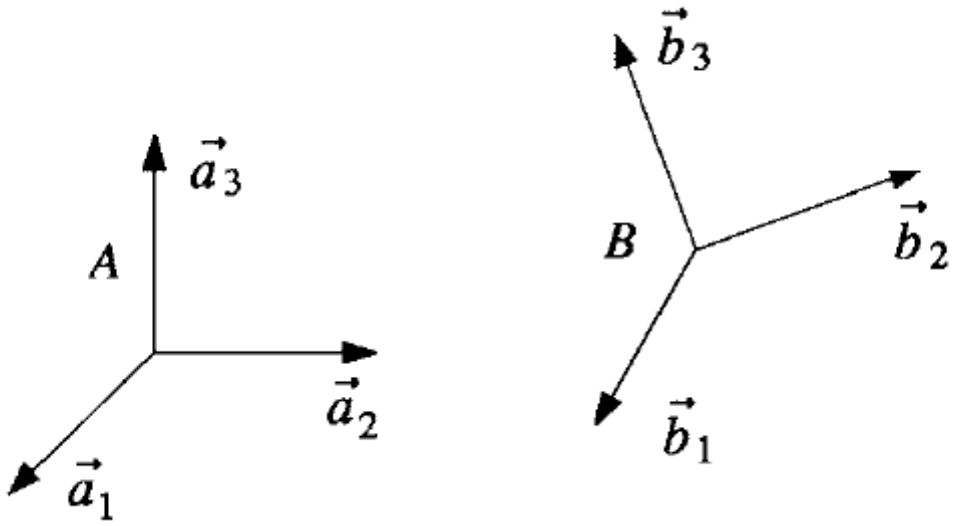

Figure 3.1: Representation of two reference systems along their basis vectors by Wie (2008)

$$\mathbf{R}_{B/A} = \begin{bmatrix} \mathbf{b}_x \cdot \mathbf{a}_x & \mathbf{b}_x \cdot \mathbf{a}_y & \mathbf{b}_x \cdot \mathbf{a}_z \\ \mathbf{b}_y \cdot \mathbf{a}_x & \mathbf{b}_y \cdot \mathbf{a}_y & \mathbf{b}_y \cdot \mathbf{a}_z \\ \mathbf{b}_z \cdot \mathbf{a}_x & \mathbf{b}_z \cdot \mathbf{a}_y & \mathbf{b}_z \cdot \mathbf{a}_z \end{bmatrix} \tag{3.1}$$

$$\mathbf{R}_{B/A}^{-1} = \mathbf{R}_{B/A}^{T} = \mathbf{R}_{A/B} \tag{3.2}$$

Direction cosine matrices can be described using these basis vectors. Two sets of basis vectors, describing two different frames of reference, can compose a matrix that contains the respective director cosines between the two bases. Thus, the matrix is expressed by the outer product of the basis vectors of the two systems, and its elements are composed of the scalar product of all basis vectors between the two frames, as shown in Equation (3.1).

This equation can also be interpreted as placing in columns the components of the arriving frame's basis vectors w.r.t. the departure frame. This last interpretation is used for most frame transformations to frames which are described by unitary vectors in the inertial frame, as seen in Equations (D.3)-(D.2) for the orbital frame. Another example is shown in Equation (D.1), where the axes are interchanged.

The direction cosine matrix is both symmetrical and orthonormal. These two properties can be expressed as the mathematical relations shown in Equation (3.2). The inverse of the direction cosine matrix, which equals its transposed matrix, also represents the inverse transformation. The remaining frame transformations coming from both euler angles and quaternions will be transformed into their equivalent DCM, as those transformations in Equations (D.4)-(D.5). The conversion seen in these equations is extracted from the work by Wie (2008) and Sidi (1997).

3.1.1. Frames of Reference

The characterisation of the dynamics around Didymos needs of the definition and set up of frames of reference, on which all vector quantities will be expressed. Some of these references frames can be observed in Figure 3.2. There, the relative location of the equatorial plane of Didymain/orbital plane of Didymoon (cyan) w.r.t. the ecliptic (green) is shown.

Some of the below-listed frames of reference have distinctive transformations that are depicted in Appendix D.

Didymos Ecliptic J2000 (DEJ2000), in green, also referred as Didymos J2000, is the inertial frame on which the dynamics will be integrated.

Origin Didymain's centre of mass

X-Axis Vernal equinox

Y-Axis Completes the right-handed system

Z-Axis Ecliptic pole

Didymos Equatorial J2000 (DJ2000) is the inertial frame, much like Ecliptic J2000, that is useful as a mid-step conversion between all Didymos's reference frames and Ecliptic J2000.

Origin Didymain's centre of mass

X-Axis Vernal equinox

Y-Axis Completes the right-handed system

Z-Axis Didymain's pole

Didymain-Didymoon Rotating Frame is a non-inertial mid-step frame used to convert quantities that are referenced to Didymoon.

Origin Didymain's centre of mass

X-Axis Pointing to Didymoon

Y-Axis Completes the right-handed system

Z-Axis Didymoon's orbital pole

Didymain Body-fixed Frame (DM), in cyan, is the non-inertial frame fixed to Didymain, useful for landmark and non-spherical gravity computation.

Origin Didymain's centre of mass

X-Axis Arbitrary direction perpendicular to the z-axis

Y-Axis Completes the right-handed system

Z-Axis Didymain's rotation axis

Didymoon Body-fixed Frame (Dm), in dark blue, is the non-inertial frame fixed to Didymain, used for non-spherical gravity computation. Since Didymoon is tidally locked, the relative orientation between this frame and the Didymain-Didymoon Rotating Frame is fixed.

Origin Didymoon's centre of mass

Axes Along three orthogonal directions

Earth-centred Inertial (ECI) is the inertial frame on which the ephemeris of Didymos expressed.

Origin Earth's centre of mass

X-Axis Vernal equinox.

Y-Axis Completes the right-handed system

Z-Axis Perpendicular to Earth's J2000 equatorial plane

Earth-centred Earth-fixed (ECEF) is the non inertial frame fixed to the rotating Earth, on which ground station coordinates are expressed.

Origin Earth's centre of mass

X-Axis Points to the intersection of the prime meridian with the equatorial plane

Y-Axis Completes the right-handed system

Z-Axis Earth's North Pole.

Local Vertical Local Horizontal is the non-inertial orbital frame, useful to decouple the effects on the navigation performance.

Origin Spacecraft's centre of mass

X-Axis Perpendicular to the instantaneous orbital plane

Y-Axis Direction of flight

Z-Axis To nadir

SC Body Frame (SC), in light blue, is the non-inertial frame that will describe the attitude of the SC.

Origin Spacecraft's centre of mass

X-Axes Along three orthogonal directions

Camera Frame (CAM), in red, is the non-inertial frame on which the quantities observed by the camera will be simulated.

Origin Mid-point on the camera sensor

X-Axis Parallel to one side of the sensor

Y-Axis Completes the right-handed system

Z-Axis Perpendicular to the camera sensor

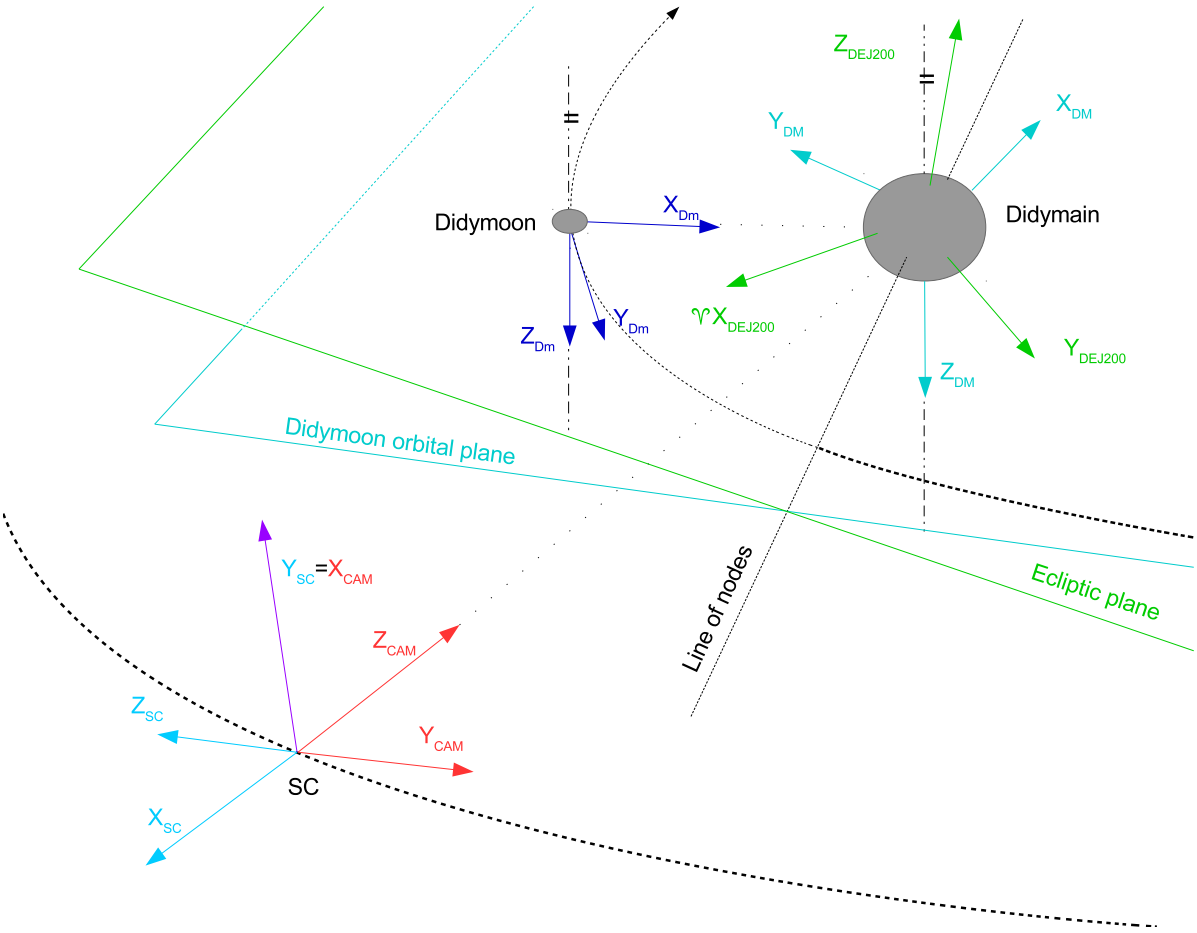

Figure 3.2: Schematic of all references frames in the Didymos system and the AIM SC

3.2. State Variables

In this section, the variables used to describe the state of the spacecraft will be summarised. These state variables are divided into three types, those which describe position, velocity, and attitude. A four set of variables, keplerian elements, will also be used, but these are in direct relation with position and velocity and can be interchanged.

To describe the complete spacecraft state, Cartesian coordinates will be used to describe position and velocity and a quaternion will be used for the attitude of the spacecraft. Thus, the complete state of the SC will be described using 10 variables. Three of which will be used for position, 3 for velocity, and the remaining 4 for the quaternion.

Cartesian coordinates are preferred over keplerian elements since their derivatives are easier to obtain, implement, and verify. Whereas expressing the disturbances as a function of the keplerian elements and obtaining their derivatives is a complex task that makes sense for longer-time integrations that those needed for this Thesis.

Position $[X\ Y\ Z]$

Velocity $[V_x\ V_y\ V_z]$

Attitude $[q_0\ q_1\ q_2\ q_3]$

To express the ephemeris of any body such as Didymos, the Sun or the Earth, Cartesian coordinates will also be used for their position and velocity. However, in the case of the ephemeris of Didymoon, keplerian elements are preferred. Since Didymoon rotates in a circular orbit, its orbit is totally determined by 5 parameters, instead of 6 variables. These are:

Semi-major axis (a) which describes the size of the orbit. It is directly related to the energy of the orbit

Eccentricity (e) describes the shape of the orbit, it is the modulus of the eccentricity vector.

Inclination (i) represents the angle between the orbit and a reference plane.

Right Ascension of The Ascending Node (Ω) the angle between the reference node line and the ascending node of the orbit.

Argument of periapsis (ω) the angular position of the perigee, measured from the ascending node.

True anomaly (θ) the actual position of the secondary in the orbit. This parameter is often substituted by either the mean anomaly or the eccentric anomaly.

However, since the periapsis is not defined for circular orbits, the argument of the periapsis is not defined either. Thus, a new parameter is used, which replaces ω and θ, and it is called the argument of latitude u, being $u = \omega + \theta$. This new parameter linearly depends on time following the next relation in Equation (3.3), where τ is a reference time for which the value of u equals zero, representing the time when the body crosses the ascending node.

$$u = \sqrt{\frac{\mu}{a^3}}(t - \tau) \tag{3.3}$$

Conversion between Cartesian coordinates and keplerian elements is required since the integration of the SC trajectory is done in Cartesian coordinates, thus, to operate all these quantities together, all variables in keplerian elements are converted into their equivalent Cartesian coordinates. This conversion is done using the Spice toolkit[2].

[2] https://naif.jpl.nasa.gov/naif/toolkit.html

3.3. Dynamics around Didymos

This section will describe the dynamics around the asteroid system Didymos and the force models used in its modelling.

3.3.1. Didymos system

As was described in Section 2.4, one of the main purposes of the AIM mission is to carry out scientific observations of a binary asteroid system. It is expected that AIM will provide insights in the dynamical behaviour and geophysical nature of the secondary body of the binary asteroid system known as 65803 Didymos (meaning twin in Greek) and alternatively designated by 1996 GT. The Didymos system is formed by two asteroids, Didymain, the biggest component of the system, and Didymoon, much smaller than Didymain.

The environmental models for Didymos were taken from Didymos Reference Model, by ESOC (2014). The current used values for the dynamics are presented in Table 3.1. These values were obtained from the work by Michel et al. (2016). The ephemerides to be used were obtained with the SPICE kernel provided by JPL. The current knowledge of the environmental model of Didymos is shown in Table 3.1, where it can be seen that the knowledge of the system is still very poor, and the uncertainty in all variables is comparable to their magnitude. Didymain's rotation axis has the peculiarity that its declination is negative, thus, Didymain rotates clockwise with respect to the ecliptic.

Table 3.1: Summary of Didymos' known parameters, by Michel et al. (2016) and Richardson et al. (2016)

Parameters	Units	Value	Error
Heliocentric semi-major axis	AU	1.6444327821	9.8e-9
Heliocentric eccentricity	-	0.383752501	7.7e-9
Heliocentric inclination (ecliptic)	deg	3.407649	2.4e-6
Primary rotation period	h	2.2600	0.0001
Distance between component COMs	km	1.18	+0.04/0.02
Mean diameter of the primary	km	0.780	10%
Mean diameter of the secondary	km	0.163	0.018
Bulk density of the primary	kgm-3	2100	30%
Total system mass	kg	5.28e11	0.54e11

Table 3.2: Didymos' parameter accuracy as per [AD01]

Parameter	Initial Knowledge σ	Final Knowledge σ
Didymain Gravitational Field (relative to nominal)	25% μ 25% J2 50% C22, S22, C31,S31,S32,C33,S33	0.0033% μ negligible improvement on others
Didymoon Gravitational Field (relative to nominal)	25% μ 25% J2	50% μ 50% J2 negligible improvement
Solar Radiation Pressure [m2/kg]	0.001 m2/kg	0.00015 m2/kg
Didymain's Rotation	0.5 deg	0.1 deg

The environment around asteroids, such as Didymos, is highly perturbed. Their small size, which implies a very low gravitational attraction, and their irregular shape, make other forces take a considerable contribution to the dynamics of a spacecraft. These forces are often disregarded for other types of environments. Thus, a good model of those force and torque sources must be done for making a representative model of the dynamics. The following values, listed in Table 3.3, have been used to recreate the SC dynamics around Didymos.

Values in Table 3.4 are coherent with the disturbance estimation done for the Rosetta mission, see Figure 2.7. These have been obtained by substituting the characteristic values in the respective

Table 3.3: List of assumptions as per [AD02]

Assumptions	Units	Value
SC Reflection Coefficient	-	1.5
SC Cross Section	m^2	5
SC Mass	kg	400
Didymos System Mass	kg	5.278e11
Mass Ratio	-	0.0093
Sun's Gravitational Parameter	km^3/s^2	132712440041.9394
Didymain's Diameter (Sphere)	m	780
Didymoon's Semi-Axes (Ellipsoid)	m	103 x 79 x 66
Didymoon's SMA	km	1.18

force models, to be later described. Main differences can be explained by the smaller size of AIM and Didymos, compared to comet 67P-Churuymov-Gerasimenko. As explained before, the extremely weak gravitational field of Didymos makes the solar radiation pressure force comparable to the gravitational force of the asteroid. The following two forces in order of importance are the third-body force of the Sun and Didymoon. Following them the next most important contribution is the non-spherical gravity (NSG) caused by the non-sphericity of Didymain and Didymoon on the spacecraft. Didymain and Didymoon also exert these NSG forces on each-other, and this has an impact on the spacecraft. However, the order of magnitude of these forces is too low to even consider them.

Table 3.4: Magnitude of the main disturbance torques

Disturbance	Units	Magnitude
Main-body force	m/s^2	10^{-7}
Third-body Sun	m/s^2	10^{-9}
Third-body Didymoon	m/s^2	10^{-9}
Solar radiation pressure	m/s^2	10^{-7}

3.3.2. Main Body Force

The main force in the Didymos system is the gravitational force exerted by the primary. This force is calculated as Wakker (2015) describes, and the actual expression is shown in Equation (3.4).

$$\mathbf{a}_{MB} = -\frac{\mu_{Didymain}}{\mathbf{r}^3} r \tag{3.4}$$

3.3.3. Third-Body Disturbance

The third-body disturbance is the perturbing acceleration caused by the presence of an external body. The perturbing body both accelerates the spacecraft and the central body. Thus, the acceleration experienced by the spacecraft in the reference frame centred in the main body is the difference of both perturbations, as shown in Equation (3.5), as Wakker (2015) described. In the Didymos system, the two main sources of third body disturbance are the Sun and the secondary component of the system, Didymoon. Didymoon has been observed to rotate about Didymain in a 1.18 km orbit, as listed in Table 3.4, and it mass has been measured to count for approximately 1/100th of the total mass in the Didymos system.

$$\mathbf{a}_{3B} = -\mu_{3B}\left(\frac{\mathbf{r}-\mathbf{r}_{3B}}{\left\|\mathbf{r}-\mathbf{r}_{3B}\right\|^3} + \frac{\mathbf{r}_{3B}}{r_{3B}^3}\right) \tag{3.5}$$

3.3.4. Solar-Radiation Pressure

The solar-radiation pressure is the effect of light being absorbed/reflected by a surface. Photons carry momentum with them. When a photon hits a surface, linear momentum is exchanged in between them two. If the photon is absorbed, the total linear momentum is equal to the sum of that of the photon and the surface that is being hit. However, if the photon is reflected, an extra contribution to the surface's linear momentum is observed, which comes to the fact that the photon is pushed away in another direction.

In space, the main source of radiation is the Sun, which accounts for almost all radiation pressure. The Sun emits energy that spreads out across the Solar System. The effect that the solar radiation has on any spacecraft can be modelled as a pressure which decays with the inverse square of the distance to the Sun. Thus, the amount of radiation pressure can be expressed as a function of the distance to the Sun; in this model shown in Equation (3.6), it has been referenced to the Solar Constant, which represents the solar pressure observed at the Earth's distance. The overall force depends on many parameters, being the shape of the spacecraft among them. Thus, it is modelled as Wertz (1978) described, as a single sphere with a reference area, useful for force calculation. Equation (3.7) shows the actual model used for the computation of the solar-radiation-pressure perturbation force.

$$\begin{aligned} P_R &= \frac{1}{c}\frac{C_{Sun}}{4\pi r_{SC/Sun}^2[AU]}\text{N/m}^2 \\ C_{Sun} &= 1367\text{W/m}^2 \end{aligned} \tag{3.6}$$

$$\mathbf{a}_{SRP} = P_R \frac{A_{ref} C_R}{m_{SC}} \frac{\mathbf{r_{SC/Sun}}}{r_{SC/Sun}} \tag{3.7}$$

3.3.5. Non-Spherical Gravity

The non-spherical and non-homogeneous distribution of mass in a body causes the single point approximation of the gravitational force to fall insufficient to describe the actual phenomenon. Small bodies such as asteroids, comets, and small moons have a very irregular shape, mass distribution, etc. which implies that the gravitational field around them is quite complex and highly deviates from the singl10^-point-mass approximation.

Thus, the gravitational field can be discretised using a series of spherical harmonics. These spherical harmonics are divided into to kinds, the zonal, J_n, and the tesseral harmonics, C_{nm} and S_{nm}. The singl10^-point-mass contribution is decoupled from the NSG field, as shown in Equation (3.8), where $B(r, \phi, \lambda)$ represents this field, and it can be calculated with the formula in Equation (3.9). Thus, having discretised the NSG field, as a series of J_n and C_{nm} and S_{nm} coefficients, the contribution to the acceleration is calculated by taking the gradient of the field, as shown in Equation (3.10).

$$U(r, \phi, \lambda) = \frac{\mu}{r}(-1 + B(r, \phi, \lambda)) \tag{3.8}$$

$$B(r, \phi, \lambda) = \sum_{n=2}^{\infty} \left(\frac{R}{r}\right)^n \left[J_n P_n(\sin\phi) + \sum_{m=1}^{n} \left(C_{nm}\cos m\lambda + S_{nm}\sin m\lambda\right) P_n m(\sin\phi)\right] \tag{3.9}$$

$$\mathbf{a}_{NSG} = -\nabla(U(r, \phi, \lambda)) \tag{3.10}$$

The spherical harmonics for the NSG of Didymos have been provided by GMV up to order 20. A list containing these harmonics up to 4th degree is shown in Table 3.5 and Table 3.6. In the case of Didymoon, the moon is modelled after a spheroid with three different radii, $a = 103$ $b = 79$ $c = 66$, all in metres. By assuming a constant density, the harmonics are calculated up to order 4, as shown in Equation (3.11) and Equation (3.12). The results are shown in Table 3.7.

$$R^2 = \frac{3}{\frac{1}{a^2} + \frac{1}{b^2} + \frac{1}{c^2}} \tag{3.11}$$

$$\begin{aligned} J_2 &= \frac{c^2 - (a^2 + b^2)/2}{5R^2} \\ C_{22} &= \frac{a^2 - b^2}{20R^2} \\ J_4 &= \frac{15}{7}(J_2^2 + 2C_{22}^2) \\ C_{42} &= \frac{5}{7}J_2 C_{22} \\ C_{44} &= \frac{5}{28}C_{22}^2 \end{aligned} \tag{3.12}$$

Table 3.5: Didymain - Zonal and Cosine Tesseral Harmonics

n/m	J_n	C_{n1}	C_{n2}	C_{n3}	C_{n4}
1	$7.19 \cdot 10^{-7}$	$4.84 \cdot 10^{-17}$			
2	$-1.14 \cdot 10^{-2}$	$1.35 \cdot 10^{-3}$	$7.76 \cdot 10^{-4}$		
3	$2.11 \cdot 10^{-2}$	$2.98 \cdot 10^{-3}$	$6.96 \cdot 10^{-4}$	$8.84 \cdot 10^{-5}$	
4	$4.58 \cdot 10^{-2}$	$1.31 \cdot 10^{-3}$	$-2.04 \cdot 10^{-4}$	$1.60 \cdot 10^{-4}$	$6.39 \cdot 10^{-6}$

Table 3.6: Didymain - Sine Tesseral Harmonics

n/m	S_{n1}	S_{n2}	S_{n3}	S_{n4}
1	$1.67 \cdot 10^{-17}$			
2	$1.19 \cdot 10^{-5}$	$1.06 \cdot 10^{-3}$		
3	$-3.83 \cdot 10^{-3}$	$-1.11 \cdot 10^{-4}$	$-8.74 \cdot 10^{-5}$	
4	$-7.65 \cdot 10^{-4}$	$-1.03 \cdot 10^{-5}$	$2.69 \cdot 10^{-5}$	$7.71 \cdot 10^{-6}$

Table 3.7: Didymoon - Zonal and Cosine Tesseral Harmonics

n/m	J_n	C_{n1}	C_{n2}	C_{n3}	C_{n4}
1	0	0			
2	$-1.31 \cdot 10^{-1}$	0	$3.52 \cdot 10^{-2}$		
3	0	0	0	0	
4	$4.22 \cdot 10^{-2}$	0	$-3.30 \cdot 10^{-6}$	0	$2.21 \cdot 10^{-4}$

Chapter 4
Navigation and Guidance

Guidance, navigation and control (GNC) systems are in charge of the estimation and correction of the state of a spacecraft. The dynamical parameter estimation problem consists of the determination of a set of parameters that are unknown to model the dynamics of a system. During this work, they have been divided into two main categories, depending on whether they influence the dynamics of the spacecraft in its movement or just the sensor observations.

- Dynamical parameters
  - Spacecraft state: position, velocity, attitude, and attitude rate.
  - Ephemeris of all celestial bodies involved.
  - Gravitational field: gravitational parameter and spherical harmonics.
  - Centroid/Centre of mass of the bodies and their rotational state.
  - System barycentre.
  - Shape model.
  - Solar-radiation pressure.
- Observation parameters
  - Landmark positions.
  - Rotational state of the body.
  - Observation errors.

4.1. Measurement Models

Sensors gather the information that will later be processed by the navigation system to estimate the state of the spacecraft. In this section, performance models of all measurements used in the navigation analysis of the AIM mission will be depicted and described.

The measurements to be considered in this navigation analysis can be divided by their character into two types.

Radiometric These are the data derived from the observations of ground stations. Inertial position and velocity of the spacecraft can be derived from these data. This type of measurements can only be available when SC-Ground communication is being held.

Optical Navigation cameras take pictures which will be later processed to infer the relative state of the spacecraft to the asteroid.

As per Section 2.4, AIM has a constraint in terms of communications. Its high-gain fixed antenna disables simultaneous data gathering and transmission. When cameras are pointed to the asteroid, no data transmission can be established, and vice versa. Thus, optical and radiometric measurements are mutually exclusive and attitude manoeuvres must be executed in between these two modes.

4.1.1. Radiometric Measurements

Radiometric measurements are, by definition, those measurements which are extrapolated from SC radio signals received by ground stations. Their characteristic character makes absolutely necessary to employ powerful filtering processes to remove almost all noise signals and biases. These processes are typically done together with the complete orbit determination, where the raw measurements are provided into the filter.

Thus, only real measurements such as range and Doppler, in terms of their geometrical meaning, distance and line-of-sight rate, can be obtained once the filtering process has ended. Thus, characteristic errors are obtained together with the filtered measurements. Typical values, common for these types of missions to asteroids are shown in Table 4.1. These error assumptions and models have been checked by the ground orbit-determinations teams at ESOC.

Table 4.1: Error assumptions on measurements for FASTMOPS CCN, as described by Branco et al. (2016) as per [AD03]

Measurement errors	1-Sigma noise	Bias	Acquisition frequency
Range [m]	3	5	Every hour
Doppler [mm/s]	0.1	0	Every 10 minutes
ΔDOR [m]	0.1-0.2	0	Every 4 days

Table 4.2: Deep-space ground station coordinates as per [AD03]

Ground Stations considered	Longitude	Latitude
Cebreros	-4.17º	40.27º
New Norcia	115.82º	-21.80º
Malargüe	-69.39º	-37.77º

Range Measurements

Range measurements are one-way light speed observations carried out by ground stations on Earth. This kind of radiometric measurement computes the time difference between two epochs, the one when the signal was transmitted and the one when it was received. This time difference can be translated into a distance when the transmission velocity of the signal is known.

A performance model of this process has been implemented. The measured range can be expressed as a mathematical relation between three parameters, the position of the SC with respect to the body $\mathbf{X}$, the ephemeris of that body w.r.t the Earth $\mathbf{X}_{es}$, and the current position of the ground station antenna $\mathbf{X}_{ce}$ taking the measurement. A schematic of the geometry of this problem is shown in Figure 4.1. These range measurements are restricted by their visibility conditions. In other words, for the observation to be made in the first place, e.g., not blocked by the horizon or distorted too much by the atmosphere, the condition in Equation (4.1) must be met. This condition establishes a minimum elevation angle over the horizon, on top of which it can be safely assumed that range observations can be made.

$$\|\boldsymbol{\rho}\| = \|\mathbf{X} - \mathbf{X}_{es} - \mathbf{X}_{ce}\| \tag{4.1}$$

$$\sin(\epsilon_{min}) \leq \frac{\boldsymbol{\rho} \cdot \mathbf{X}_{ec}}{\rho X_{ec}} \tag{4.2}$$

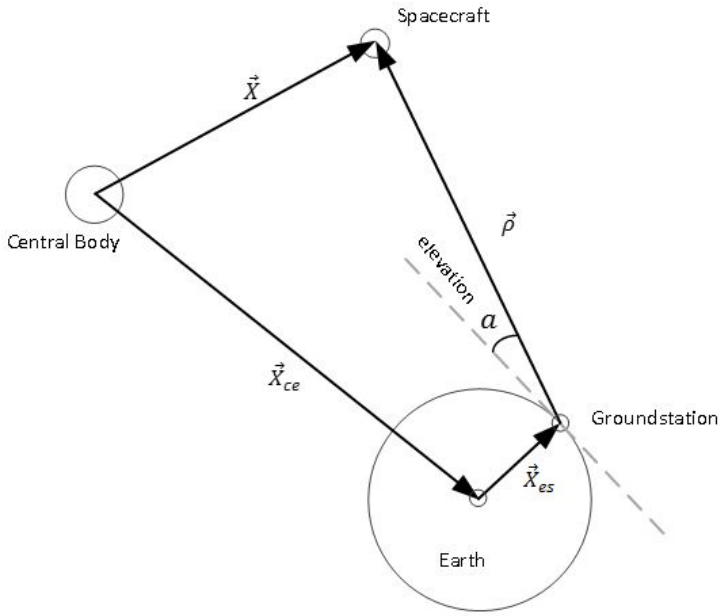

Figure 4.1: Radiometric measurements - Range computation as per [AD04]

Several range observations can be available if there is visibility by at least two ground stations. If that happens, the two range measurements can be differentiated to obtain a much more precise observation. This is called Delta-DOR.

Doppler Measurements

Doppler observations are made by measuring the received frequency from the SC. If the original frequency in which the signal was transmitted is known, the received frequency is measured and, thus, a frequency shift can be computed. This frequency shift can be transformed into into line-of-sight velocity measurements. Consequently, these velocity measurements carry no information in the perpendicular directions to the LOS.

$$\boldsymbol{\rho}' = \mathbf{V} - \mathbf{V}_{es} - \mathbf{V}_{ce} \tag{4.3}$$

$$\dot{\rho} = \frac{\boldsymbol{\rho} \cdot \boldsymbol{\rho}'}{\rho} \tag{4.4}$$

The measured LOS velocity can be expressed as the projection of the total velocity of the SC w.r.t the ground station on the LOS between them, as shown in Equation (4.3) and Equation (4.4). The range equation can be differentiated to obtain the desired expression for the velocity, which is identical to Equation (4.1). Then, this velocity is projected along the line-of-sight, to compute the actual Doppler measurement. Doppler measurements are computed in the same way as range measurements are. Thus, the same geometrical constraint, due to the blockage of the atmosphere and the horizon, is present and must be computed to exclude the non-valid Doppler measurements.

DDOR Measurements

Delta-DOR is a Very Long Baseline Interferometry (VLBI) technique that allows for a very precise position determination for deep space missions, as depicted by NASA (2009). Two ground stations are required to track the spacecraft and a quasar simultaneously. The objective of this technique is to refine the one-way ranging process by referring it to the inertial quasar background.

The signal is acquired by two ground stations, which transform it into phase measurements. These two observations are then correlated to calculate the delay between the two signals, which is transformed into an angular measurement. As can be seen in Figure 4.2, the greater the distance between two ground stations, baseline, the higher the delay, and the more precise the estimate is. Delta-DOR measurements provide a very precise angular position estimate on the sky when compared to other methods, as shown by NASA (2009).

However, the Delta-DOR technique requires two ground stations to overlap operations, as shown in Figure 4.3. The scheduling and preparation of such measurements is not easy, and it is restricted to certain windows. This is due to the long distance that separates the ground stations. The spacecraft and the quasar must be trackable by both stations at the same time. This restricts the actual operational time to short-time windows.

Delta-DOR measurements are not single instantaneous measurements, they are the result of raw-data processing received by the ground stations during hours. These processed data give a high precision range measurement from the Earth to the tracked source. Thus, the resulting performance model precises at least two ground stations to be simultaneously observing the SC's incoming signal. These measurements are limited by the same constraints exposed for range and Doppler. Finally, the two resulting ranges are combined, and an single range measurement, referenced to the baseline centre, as shown in Equation (4.5).

$$\hat{\rho}_{\Delta DOR} = \left\| (\boldsymbol{\rho}_1 + \boldsymbol{\rho}_2)/2 \right\| \tag{4.5}$$

4.1.2. Optical Measurements

Centroiding

Centroid measurements provide information of the line of sight to a body's location. The estimation is generally carried out by image processing algorithms. These algorithms receive a picture of a body and treat and process it until an estimation of the geometrical centre of the image's body is obtained. A performance model of the centroid determination process has been implemented. This model calculates the projection of the line-of-sight (LOS), as shown in Equation (4.6) to the computed centroid on the camera sensor, Equation (4.7).

$$\mathbf{LOS} = -\frac{\mathbf{r}_{SC}}{r_{SC}} \tag{4.6}$$

$$\mathbf{LOS}_{CF} = \mathbf{R}_{CF/BF}\mathbf{R}_{BF/J2000}\mathbf{LOS} \tag{4.7}$$

The camera sensor consists on 2D grid of pixels where the LOS is projected. The projection of the position in Equation (4.10) is then calculated combining Equation (4.8)-(4.9), as shown by Wertz (1978). Real performance noise and bias values are added to this measurement, properly simulating the performance of centroiding. Since an actual measurement of the camera consists on the coordinates of the illuminated pixel, which can only be integers, the measurement is converted to integers.

$$\mathbf{LOS}_{CF} = \begin{pmatrix} -\sin\phi\cos\lambda \\ \cos\phi\cos\lambda \\ -\sin\lambda \end{pmatrix} \tag{4.8}$$

$$\begin{aligned} \tan\phi &= px_i \cdot px_{size} \\ \tan\lambda &= px_j \cdot px_{size}\cos\phi \end{aligned} \tag{4.9}$$

$$\begin{aligned} px_i &= -\frac{1}{px_{size}}\frac{LOS_y}{LOS_z} \\ px_j &= -\frac{1}{px_{size}}\frac{LOS_x LOS_z}{\sqrt{1-LOS_x^2}\sqrt{LOS_y^2+LOS_z^2}} \end{aligned} \tag{4.10}$$

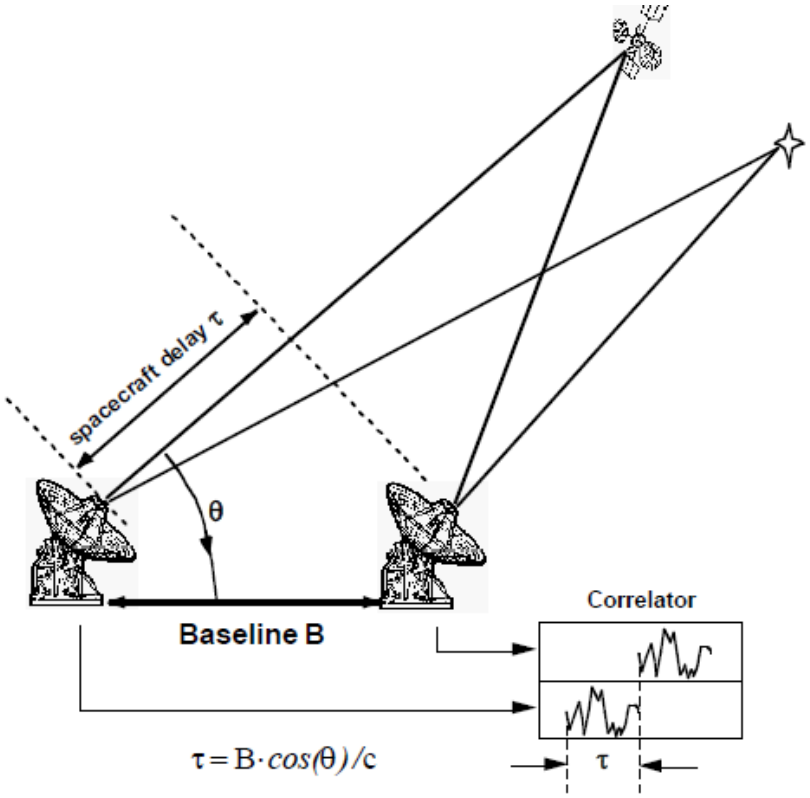

Figure 4.2: Delta-DOR working-principle schematic, by NASA (2009)

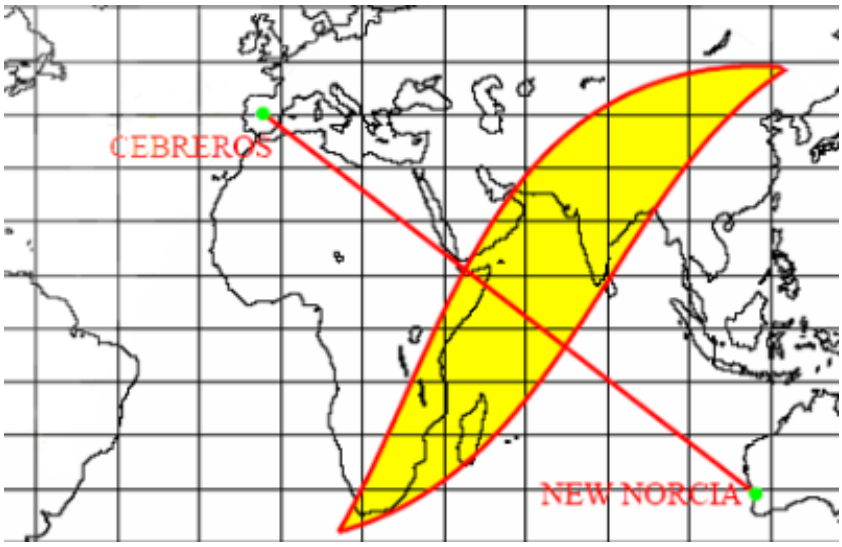

Figure 4.3: Delta-DOR visibility window by Iess et al. (2006)

Landmarks

Landmarks (LM) are fixed features on a surface which can be recognised and tracked. Landmark tracking has proved to be key for navigation in highly perturbed environments, such as those around asteroids. Landmark identification has long been done by operators in the ground-operations teams. They are selected on pictures taken by the navigation cameras on a spacecraft and subsequently tracked on each posterior image.

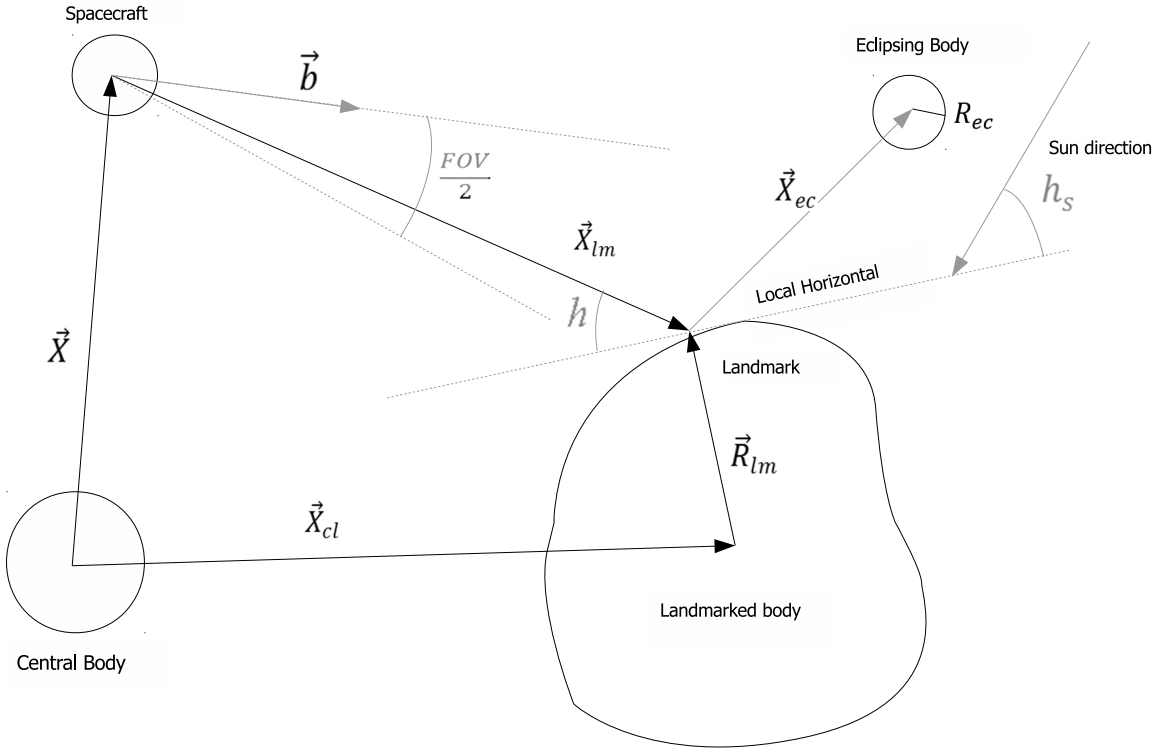

Figure 4.4: Landmark computation, based on [AD04]

These camera readings were simulated via a performance model. This model computes the line of sight from the camera, as can be seen in Figure 4.4, to the landmark and converts it into pixel positions on the camera sensor.

The generation of landmark positions is computed using the following algorithm:

- First, points are distributed on an unity sphere. These points can be randomly scattered or evenly distributed. Zonal point-density can also be modified, thus, landmarks can be clustered onto one of the hemispheres, the equator, one of the poles, etc.
- Second, landmark positions are obtained by the intersection of those unity vectors with a shape model for Didymain.
- Third, normals at those positions are computed.

Then, the readings of the position of each landmark by the landmark matching algorithms are simulated. The position of the landmark with respect to the spacecraft is computed as shown in Equation (4.11). This position is transformed to LOS in the camera frame as was performed for the centroiding algorithm in Equation (4.6) and Equation (4.7). Then, the landmarks which cannot be

recognised by the algorithm are discarded. The first condition consists on the elevation on which the landmark is being observed from the SC.

$$\mathbf{X}_{lm} = \mathbf{X}_{cl} + \mathbf{R}_{lm} - \mathbf{X} \tag{4.11}$$

If the elevation angle of the spacecraft to the LM is too low, the necessary conditions for the landmark to be recognised by the algorithm could not be met, thus a minimum elevation angle is established, as shown in Equation (4.12).

$$\sin(h_{min}) \leq \frac{-\mathbf{X}_{lm} \cdot \mathbf{n}_{es}}{\mathbf{X}_{lm}} \tag{4.12}$$

The following condition, shown in Equation (4.13) represents the illumination conditions of the LM. The LM can only be recognised if its illumination is sufficient for the camera to recognise it. This is translated into a mathematical condition by stating that the incident light on the landmark must have a minimum elevation angle, above which the landmark can be recognised.

$$\sin(h_{smin}) \leq -\mathbf{s} \cdot \mathbf{n}_{es} \tag{4.13}$$

And the last condition states that the landmark must be inside the field of view of the camera for it to be observed.

$$\frac{FOV}{2} \geq \arccos \frac{\mathbf{X}_{lm} \cdot \mathbf{b}}{X_{lm}} \tag{4.14}$$

4.2. Navigation Algorithms

Navigation filters are in charge of the reconstruction of the trajectory of a body by mixing information about its dynamics and measurements. Sequential filters perform this estimation by dividing this process into two parts: the dynamical propagation and the measurement update. Typical navigation filters are the Kalman-family of filters and the square root information filter (SRIF), as described by Tapley et al. (2004). Measurements are incorporated into the filter as soon as they are collected, one by one or in small batches. The main advantage of these filters is the ability to generate time ordered solutions based on a minimum amount of data and the information from previous estimations (from covariance or from information matrices).

The main disadvantage is the sensitivity to locally bad conditioned data that can eventually cause the filter divergence and require a certain stabilisation period to recover a stable solution. To minimise this effect one can implement a local batch process for the new dataset to detect bad conditioned data before the observations are incorporated into the estimation process. This will be implemented according to the work by Genova et al. (2012) and Parisi et al. (2012) in Section 6.2.

Other relevant navigation filters to be considered, apart from the widespread extended Kalman Filter (EKF) and the SRIF, are the unscented Kalman filter (UKF) and the H-infinity filter (HKF), as described by Simon (2006). The UKF uses a non-linear propagation of some points, called sigma-points. This non-linear propagation produces best results than the EKF, however, this comes with a higher computational load. On the other hand, the H-infinity filter was designed to increase the robustness of the filter against miss modelling. Nevertheless, the character of the miss-model has to be programmed into the filter, whereas, regular filters can absorb these uncertainties by simply tuning the correlated noise.

An schematic summary of the performance of each filter is shown in Table 4.3. With respect to all Kalman filters, the SRIF is computationally more complex because the state vector estimate is not a direct result of the estimation process, but it must be inferred from a new computed information matrix. This aspect limits partially the frequency with which the state vector can be outputted; for example, the SRIF filter would be probably less suitable than the Kalman filter for an on-board computer. However, this direct availability constraints do not impose a real problem for on-ground navigation. The SRIF

Table 4.3: Navigation Filter Comparison

Criteria	KF	EKF	UKF	HKF	SRIF
Robustness	Low	Good	High	Good	Good
Numerical precision	Good	Good	Good	Good	Best
Computational Cost	Lowest	Low	Medium	Low	Medium
Direct availability	Yes	Yes	Yes	Yes	No

has also been proven as the most precise and preferred solution for asteroid missions by Miller et al. (2002) and Godard et al. (2015).

This said, both algorithms are used for their respective strong areas. For on-board navigation, especially attitude that is mostly controlled autonomously, an EKF/UKF is preferred. This solution has long been used, as depicted in the work by Kawaguchi (2006), Kubota et al. (2006), and Shuang and Pingyuan (2008). Whereas, for increased numerical precision, the SRIF is used for ground navigation. This distinction has long been used, besides, Gil-Fernández et al. (2008) assessed this configuration this for a very similar scenario to that of the AIM mission. Nevertheless, since the current analysed scenario will only deal with ground navigation, the SRIF is selected.

4.2.1. The Square Root Information Filter

Commonly used navigation filters, such as the Kalman filters, work by propagating a covariance matrix of the estimating parameters. If the standard deviation of a component is, in magnitude, much higher than that of another, numerical problems arise when it is inverted.

This problem is increased because a covariance matrix is composed of the squares of the standard deviations, which directly doubles the condition number of this matrix. The matrix could become numerically singular due to the floating value precision, despite being perfectly analytically reversible.

This problem is palliated by propagating a pseudo square-root of the covariance matrix, $\mathbf{R}$, which is decomposed using the Cholesky factorisation. One of these methods is the square root information filter (SRIF), which corresponds with the below exposed formulation, extracted of the work by Tapley et al. (2004), where the $\mathbf{P}^{-1}$ in Equation (4.15) is the a-priori information matrix of the estimated parameters. The SRIF state vector can be particularised for the case where process noise, constant parameters, and variables are estimated. This is shown in Equation (4.16), where $\mathbf{p}$ is the correlated process noise, $\mathbf{x}$ the state vector, and $\mathbf{c}$ the bias array.

$$\mathbf{R}_{k-1}^{T}\mathbf{R}_{k-1} = \mathbf{P}_{k-1}^{-1} \tag{4.15}$$

$$\hat{\mathbf{X}}_{k-1} = \begin{pmatrix} \hat{\mathbf{p}} \\ \hat{\mathbf{x}} \\ \hat{\mathbf{c}} \end{pmatrix}_{k-1} \tag{4.16}$$

The information is then propagated to the next epoch when a new information batch is available. This data batch contains the information of all sensors from the previous epoch up to the new one. The state vector is propagated using the current best estimate of the dynamics, whereas the information matrix undergoes a more complicated update. The state transition matrix between the two epochs, as shown in Equations (4.17) and (4.18), is computed and the information matrix propagated accordingly, depending on the character of the propagated parameters.

Process noise variables are propagated as shown in Equation (4.20) while constants do not undergo any propagation. The complete process is shown on the left side of Equation (4.21). However, the actual propagation occurs when the resulting information matrix is triangularised by householder transformations, which has been schematised in Equation (4.21). Thus, the new triangularised matrix, depicted in Equation (4.22) becomes the a-priori information matrix at the new epoch.

$$\bar{\mathbf{x}}_k = \boldsymbol{\Phi}(t_k, t_{k-1})\bar{\mathbf{x}}_{k-1} \tag{4.17}$$

$$\boldsymbol{\Phi}(t_k, t_{k-1}) = \frac{\partial \mathbf{x}_k}{\partial \mathbf{x}_{k-1}} \tag{4.18}$$

$$\bar{\mathbf{X}}_k = F(\hat{\mathbf{X}}_{k-1}, t_{k-1}, t_k) \tag{4.19}$$

$$M_i = e^{-\frac{\Delta t}{\tau_i}} \tag{4.20}$$

$$\mathbf{T}\begin{bmatrix} -\mathbf{R}_w\mathbf{M}_k & \mathbf{R}_w & 0 & 0 \\ \mathbf{R}_p - \tilde{\mathbf{R}}_{px}\boldsymbol{\Phi}_{p_k} & 0 & \tilde{\mathbf{R}}_{px} & \mathbf{R}_{pc} - \tilde{\mathbf{R}}_{px}\boldsymbol{\Phi}_{c_k} \\ -\tilde{\mathbf{R}}_x\boldsymbol{\Phi}_{p_k} & 0 & \tilde{\mathbf{R}}_x & \mathbf{R}_{xc} - \tilde{\mathbf{R}}_x\boldsymbol{\Phi}_{c_k} \\ 0 & 0 & 0 & \mathbf{R}_c \end{bmatrix}_k = \begin{bmatrix} \mathbf{R}_p^* & \mathbf{R}_{pp}^* & \mathbf{R}_{px}^* & \mathbf{R}_{pc}^* \\ 0 & \bar{\mathbf{R}}_p & \bar{\mathbf{R}}_{px} & \bar{\mathbf{R}}_{pc} \\ 0 & 0 & \bar{\mathbf{R}}_x & \bar{\mathbf{R}}_{xc} \\ 0 & 0 & 0 & \bar{\mathbf{R}}_c \end{bmatrix}_k \tag{4.21}$$

$$\bar{\mathbf{R}}_k = \begin{bmatrix} \bar{\mathbf{R}}_p & \bar{\mathbf{R}}_{px} & \bar{\mathbf{R}}_{pc} \\ 0 & \bar{\mathbf{R}}_x & \bar{\mathbf{R}}_{xc} \\ 0 & 0 & \bar{\mathbf{R}}_c \end{bmatrix} \tag{4.22}$$

The a-priori transformed augmented state vector and the pseudo square-root of its information matrix are chosen as the reference for the computation of the observables, the difference between the real measurements and their filter predictions. Then, these two are placed together with the batch of observations, $\mathbf{y}$, and the design matrix $\mathbf{H}$, which links the measurements to the state vector. These two matrices are composed by their respective sub-matrices with respect to all parameters in the augmented state vector, as depicted in Equation (4.25).

This division facilitates the updating process. Since the constant parameters do not change with time, by definition, but the state vector and the process noise do, the process is divided into two sequential updates. Firstly, as shown in Equation (4.26), the changing parameters are processed and then, the resulting data is used to compute the estimation update of the constant parameters, in Equation (4.27). These two updates are also carried out by householder transformations.

$$\begin{aligned} \mathbf{X}_{ref} &= \bar{\mathbf{X}}_k \\ \bar{\mathbf{x}}_k &= 0 \\ \bar{\mathbf{z}}_k &= \bar{\mathbf{R}}_k\bar{\mathbf{x}}_k = 0 \end{aligned} \tag{4.23}$$

$$\begin{bmatrix} \bar{\mathbf{R}} & \bar{\mathbf{z}} \\ \bar{\mathbf{H}} & \bar{\mathbf{y}} \end{bmatrix}_k \tag{4.24}$$

$$\mathbf{H} = \begin{bmatrix} \mathbf{H}_p & \mathbf{H}_x & \mathbf{H}_c \end{bmatrix} = \frac{\delta \mathbf{y}_k}{\delta \mathbf{x}_k} \tag{4.25}$$

$$\mathbf{T}\begin{bmatrix} \bar{\mathbf{R}}_p & \bar{\mathbf{R}}_{px} & \bar{\mathbf{R}}_{pc} & \bar{\mathbf{z}}_p \\ 0 & \bar{\mathbf{R}}_x & \bar{\mathbf{R}}_{xc} & \bar{\mathbf{z}}_x \\ \mathbf{H}_p & \mathbf{H}_x & \mathbf{H}_c & \mathbf{y} \end{bmatrix}_k = \begin{bmatrix} \tilde{\mathbf{R}}_p & \tilde{\mathbf{R}}_{px} & \tilde{\mathbf{R}}_{pc} & \tilde{\mathbf{z}}_p \\ 0 & \tilde{\mathbf{R}}_x & \tilde{\mathbf{R}}_{xc} & \tilde{\mathbf{z}}_x \\ 0 & 0 & \tilde{\mathbf{H}}_c & \mathbf{y} \end{bmatrix}_k \tag{4.26}$$

$$\mathbf{T}\begin{bmatrix} \bar{\mathbf{R}}_c & \bar{\mathbf{z}}_c \\ \tilde{\mathbf{H}}_c & \mathbf{y} \end{bmatrix}_k = \begin{bmatrix} \tilde{\mathbf{R}}_c & \tilde{\mathbf{z}}_c \\ 0 & \mathbf{e} \end{bmatrix}_k \tag{4.27}$$

The vector $\mathbf{e}$ in Equation (4.27) already represents an approximation of the residuals, thus eliminating the necessity of an a-posteriori residual calculation. If the residuals are too large, the new state can be fed back into the updating process to improve the estimation. The new pseudo-square-root of the information matrix and the information vector can be used to compute the new state vector and the new covariance matrix, as shown in Equation (4.29). However, this is not necessary. These two can directly be put back into the loop for the next iteration.

$$\begin{aligned} \tilde{\mathbf{z}}_k &= \begin{pmatrix} \tilde{\mathbf{z}}_p \\ \tilde{\mathbf{z}}_x \\ \tilde{\mathbf{z}}_c \end{pmatrix}_k \\ \hat{\mathbf{x}}_x &= \tilde{\mathbf{R}}_k \tilde{\mathbf{z}}_k \end{aligned} \tag{4.28}$$

$$\hat{\mathbf{X}}_k = \overline{\mathbf{X}}_k + \hat{\mathbf{z}}_k \tag{4.29}$$

$$\hat{\mathbf{P}}_k = (\tilde{\mathbf{R}}_k^T \tilde{\mathbf{R}}_k)^{-1} \tag{4.30}$$

4.3. Guidance Algorithms

The high-level objective of guidance systems is to compute the necessary trajectory and corrections to arrive at a target. This is represented in Figure 4.5, where the continuous line represents the nominal trajectory and the dashed line the trajectory that allows the SC to arrive at the desired location.

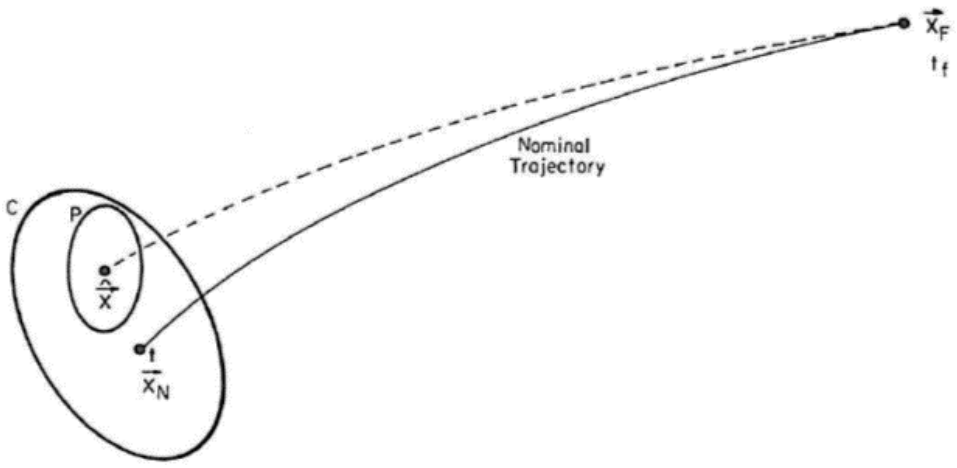

Figure 4.5: Schematic of the guidance problem as per [AD05]

This is done regarding the fact that the SC state is known neither with infinite precision nor with the dispersion from the nominal trajectory. This is represented by the $\mathbf{C}$ and $\mathbf{P}$ matrices in Equation (4.31), where $\mathbf{C}$ is the dispersion matrix, which represents the deviation from the nominal trajectory $\mathbf{x}$, and $\mathbf{P}$ the covariance matrix, representing the knowledge on the state of the spacecraft.

Due to the properties of these matrices, $\mathbf{C}$ is always greater or equal than $\mathbf{P}$, in other words, the knowledge of the spacecraft position cannot be worse than the expected deviation from the nominal trajectory. Thus, if the dispersion errors are too close to those of the SC state, the deviation directly falls in the uncertainty region, where the SC is very likely to be, and the capability of correcting the spacecraft trajectory is null.

$$\begin{aligned} \mathbf{C} &= \mathrm{E}[\mathbf{x} \cdot \mathbf{x}^T] \\ \mathbf{P} &= \mathrm{E}[(\hat{\mathbf{x}} - \mathbf{x}) \cdot (\hat{\mathbf{x}} - \mathbf{x})^T] \end{aligned} \tag{4.31}$$

4.3.1. Guidance Law selection

These corrections on the SC state are computed by guidance laws. These guidance laws yield the necessary ΔV to carry the SC from its current position to a determined target, with the possibility of fixing an arrival time. A comparison between three considered guidance laws in shown in Table 4.4.

Simple algorithms such as the fixed-time of arrival (FTOA), as depicted by Tempelman (1986), have long been used to compute manoeuvres. These algorithms have a high TRL since they have been fligh-proven for high-thrust manoeuvre corrections. Their implementation is easy, since they are based on linear models with few elements. Large correction manoeuvres are possible using this algorithm. Despite the fact that it is based on a linear model, a simple iterative process can be used to accommodate these type of manoeuvres.

Other models such as the Model Predictive Control (MPC) or receding horizon, developed by Gil-Fernandez and Gomez-Tierno (2010), and already implemented in FEST, software that will be introduced in Chapter 6 and further described in Appendix C. This algorithm aims to reach a waypoint at a specific epoch. The distribution of these waypoints help the SC to stay close to the reference trajectory during the transfer arc. This algorithm was developed using optimal guidance and control laws that can accommodate thrust constraints in both magnitude and direction. The algorithm is based on the assumption that all corrections are small. However, for the working case-scenario, manoeuvres are constrained to four nodes, where the trajectory is completely deviated from the natural path it would follow without guidance.

Differential algebra algorithms, as described by Di Lizia (2008), are based on n^{th} order solutions to a system of ODEs with boundary conditions. As an example of these algorithms, a low-degree guidance law for the two-body problem is the Lambert's problem. The algorithm can be accommodated to both high-thrust and low-thrust solutions, and be applied to both small and large corrections. Nevertheless, the complexity of the algorithm escalates with the complexity of the SC dynamics.

Thus, the FTOA algorithm is observed to comply with the requirements for the analysed mission: large correction manoeuvres, high thrust, and flight-proven, thus representative of actual guidance solutions.

Table 4.4: Guidance algorithms

Guidance Law	Advantages	Disadvantages
Fixed-time of Arrival	Simple Flight-proven Mature	High fuel consumption in low-thrust
Model Predictive Control	Based on optimal control Small computational load	Not optimal for large correction manoeuvres Complex formulation
Differential Algebra	Suitable for low-thrust	Low Maturity Hard to implement

4.3.2. Fixed-time of Arrival Guidance Law

Guidance laws have the objective of reducing the deviation of the SC from the nominal trajectory, thus, in mathematical terms, minimising the $\mathbf{C}$ matrix. This is generally done by computing Δ V manoeuvres which are a function of the starting deviation. For this MSc. Thesis, the Fixed-Time of Arrival (FTOA) algorithm was selected.

This particular algorithm consists on finding the trim manoeuvre, $\mathbf{u} = \mathbf{\Lambda}\hat{\mathbf{x}}$ that makes the SC arrive at a particular position at a desired time. This was explained by Battin (1968) and Leondes (1968), and the formulation has been adapted from the latter. The initial state of the spacecraft, as shown in Equation (4.32), is composed of the three components of its position and the three components of its velocity, a 1x6 vector.

$$\hat{\mathbf{x}}(t_0) = \begin{pmatrix} \delta\mathbf{r}(t_0) \\ \delta\mathbf{V}(t_0) \end{pmatrix} \tag{4.32}$$

Following the linear theory, in Equation (4.33), there is a transition matrix, which depends on the initial and final time that transforms the initial state into the final state. Where the transition matrix represents the relation in Equation (4.34).

$$\hat{\mathbf{x}}(t_f) = \mathbf{\Phi}(t_f, t_0)\hat{\mathbf{x}}(t_0) \tag{4.33}$$

$$\mathbf{\Phi}(t_f, t_0) = \left[\frac{\partial \mathbf{x}(t_f)}{\partial \mathbf{x}(t_0)}\right]_{6x6} \tag{4.34}$$

Imposing the guidance law, taking into account that the final deviation must be 0, and solving for the correction in velocity, $\mathbf{u}$, as exposed in Equation (4.35), we get the following expression in Equation (4.36), from which the guidance matrix can be extracted, as well as the correction in velocity. Where the sub-matrices $\mathbf{\Phi}_1$ and $\mathbf{\Phi}_2$ represent the partial matrices of the complete transition matrix, as shown in Equation (4.37).

$$\begin{aligned} \mathbf{u} &= \mathbf{\Lambda}\check{\mathbf{x}}(t_0) \\ \hat{\mathbf{x}}(t_f) &= \mathbf{\Phi}(t_f, t_0)\begin{pmatrix} \delta\mathbf{r}(t_0) \\ \delta\mathbf{V}(t_0) + \mathbf{u} \end{pmatrix} \\ \delta\mathbf{r}(t_f) &= 0 \end{aligned} \tag{4.35}$$

$$\begin{aligned} \mathbf{u} &= -\mathbf{\Phi}_2^{-1}\mathbf{\Phi}_1\delta\mathbf{r}(t_0) - \delta\mathbf{V}(t_0) \\ \mathbf{\Lambda} &= \left[-\mathbf{\Phi}_2^{-1}\mathbf{\Phi}_1 \quad \mathbf{I}\right]_{3x6} \end{aligned} \tag{4.36}$$

$$\begin{aligned} \mathbf{\Phi}_1(t_f, t_0) &= \left[\frac{\partial \mathbf{r}(t_f)}{\partial \mathbf{r}(t_0)}\right]_{3x3} \\ \mathbf{\Phi}_2(t_f, t_0) &= \left[\frac{\partial \mathbf{r}(t_f)}{\partial \mathbf{V}(t_0)}\right]_{3x3} \end{aligned} \tag{4.37}$$

4.3.3. Mechanisation Error Model

When manoeuvres are carried out, errors are introduced. These mechanisation errors depend on the character of the actuator carrying out the manoeuvre. In the case of thrusters, which is exactly the type of actuators that AIM will be carrying, a simple model can be developed. The error is characterised into two types: an error in the magnitude of the thrust and an error in its direction. This characterisation can be seen in Figure 4.6.

Thus, the actual manoeuvre experienced by the SC $\Delta\mathbf{V}$ is a combination of the commanded manoeuvre $\mathbf{u}$ and its error $\boldsymbol{\eta}$, as seen in Equation (4.38). The covariance matrix of the commanded manoeuvre is a function of the correction in the dispersion matrix and the guidance matrix itself, as shown in Equation (4.39). And the mechanisation error matrix is defined as per Equation (4.40).

$$\Delta\mathbf{V} = \mathbf{u} + \boldsymbol{\eta} \tag{4.38}$$

$$\mathrm{E}[\mathbf{u} \cdot \mathbf{u}^T] = \mathbf{\Lambda}(\mathbf{C} - \mathbf{P}))\mathbf{\Lambda}^T \tag{4.39}$$

$$\mathbf{M} = \mathrm{E}[\boldsymbol{\eta} \cdot \boldsymbol{\eta}^T] \tag{4.40}$$

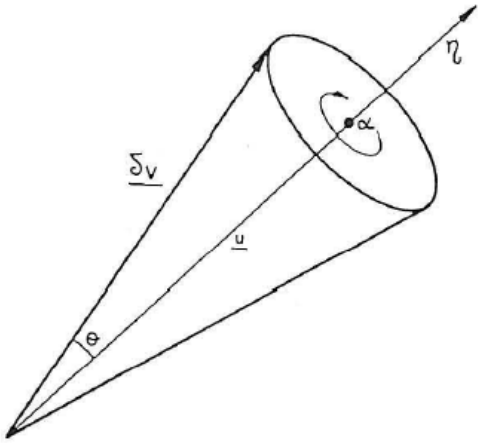

Figure 4.6: Mechanisation error model as per [AD05]

The mechanisation error modelled for this analysis consists on the nominal correction manoeuvre and the two previously mentioned parameters, magnitude and direction. The direction error is modelled with two extra parameters, representing the angle of the cone and the phase around the nominal manoeuvre.

- Gaussian error for the modulus of the manoeuvre $\eta = \mathrm{N}(0, \sigma_\eta)$
- Gaussian error in a cone angle $\theta = \mathrm{N}(0, \sigma_\theta)$
- Uniform distributed error in the phase angle $\alpha = \mathrm{U}(0, 2\pi)$

The expression of the mechanisation error as a function of these three error variables is shown in Equation (4.41), and its expectancy is shown in Equation (4.42). Only two of the three variables are Gaussian. Thus, the error cannot be described as the sum of all normal contributions, with zero mean and a characteristic sigma. A sign of this phenomenon is the error expectancy, which is not zero.

$$\boldsymbol{\eta} = \mathbf{u} - \Delta\mathbf{V} = \begin{pmatrix} (u+\eta)\cos\alpha\sin\theta \\ (u+\eta)\cos\alpha\sin\theta \\ (u+\eta)\cos\theta \ - u \end{pmatrix} \tag{4.41}$$

$$\mathrm{E}[\boldsymbol{\eta}] = \begin{pmatrix} 0 \\ 0 \\ -\sigma_\theta^2 \mathrm{E}(u)\left(1 - \frac{\sigma_\theta^4}{4}\right) \end{pmatrix} \tag{4.42}$$

As has been mentioned before, not all errors are Gaussian. The overall error for the mechanisation is non-Gaussian, and the covariance matrix is complex to be obtained. If the mechanisation error is expressed as a function of the three error variables, η, θ, and α, its covariance matrix can be calculated as per Equation (4.43), where $\mathrm{E}(u^2) = \sigma_{u_1}^2 + \sigma_{u_2}^2 + \sigma_{u_3}^2$

$$\mathbf{M} = \begin{bmatrix} \frac{1}{2}\mathrm{E}(u^2)(\sigma_\eta^2 + (1-\sigma_\theta^2)) & 0 & 0 \\ 0 & \frac{1}{2}\mathrm{E}(u^2)(\sigma_\eta^2 + (1-\sigma_\theta^2)) & 0 \\ 0 & 0 & \mathrm{E}(u^2)((\sigma_\eta^2(1-\sigma_\theta^2) + \frac{3}{4}\sigma_\theta^4) - \frac{1}{4}\sigma_\theta^2) \end{bmatrix} \tag{4.43}$$

Since the mechanisation error behaves in a non-Gaussian way, the complete manoeuvre is also non-Gaussian and the analytic methods fail to describe it when high errors are introduced. Therefore, Monte Carlo simulations are used to compute the covariance matrix and the mean value for the manoeuvre. A sample of errors is computed and then, the covariance of the sample is calculated.

Chapter 5
Numerical Methods

The following chapter summarises the numerical methods to be used in this MSc. Thesis as per Chapter 4. In this previous chapter, the necessity of having a set of numerical methods was exposed. These methods allow to perform certain numerical tasks, which are key in the development of an engineering simulator. Among these are: the selection of a numerical integrator, to integrate the equations of motion, a numerical interpolator, to discretise variables and use them afterwards, and two numerical operators for matrices, which are the core of the SRIF algorithm, described in Section 4.2.

5.1. Numerical Integrator

Numerical-integration methods are in charge of the integration of the equations of motion. This integration process entails the transformation from a continuous to a discrete problem. The ordinary differential equations (ODE) are transformed into finite-difference equations, which are their discrete equivalent. The mathematics behind these two are based on very different fields with separate working principles and properties. Thus, the proper selection of a numerical method becomes essential, since the properties of the method will influence the solution for which it was used.

These methods, as described by Hahn (1967), are characterised by some properties such as consistency, convergence, and zero-stability, which will be described later. Montenbruck (1992) analysed and compared the computational performance of several high-order methods for orbital integration, such as Adams-Bashford/Moulton methods and variable-step Runge-Kutta methods.

Adams-Bashford/Moulton methods offer a great numerical stability, but they carry an important drawback. Since equations in finite differences offer as many numerical solutions as roots the equation has, and these methods are multi-step, thus multi-root, there would appear as many fictitious solutions as extra steps in the numerical method. For an eight-step integration method, seven spurious/fictitious solutions would pollute the actual solution.

Montenbruck (1992) also assessed variable-step Runge-Kutta methods and the number of function evaluations for achieving a certain accuracy, as can be seen in Figure 5.1. Montenbruck and Gill (2000) also unveiled that despite the smaller number of function calls of the higher-order and variable-step methods for a given precision, the computational load could be higher. This was due to the internal calculations for the error and step-size control. These accounted for at least a 20% of the total amount, if not higher, while when these methods discarded the step-size control, that amount was reduced to a 5%. Thus, the use of a higher-order method does not really imply more precision at a shorter computational load.

Two types of numerical integration will be performed in the simulator. One type consists on short-time propagations, used for the integration of the SC dynamics and the computation of the state transition matrix. These numerical integrations are performed many times and will yield states at every analysed epoch. Thus, a lower order method with a lower computational load such as the DOPRI5 fits perfectly this task.

The second type consists on the propagation of the last known state of the SC during a two-day hyperbolic arc, for manoeuvre computation. Since only the last state of this long integration arc is to be obtained, longer time-steps are preferred. For higher accuracy, the Dormand and Prince's eighth order method (DOPRI8), as developed by Prince and Dormand (1981), performs astonishingly well when compared to the rest of the analysed numerical methods.

5.1.1. The Runge-Kutta Numerical-Integration Method

The Runge-Kutta is a set of multistage numerical integration methods where the function is evaluated several times in between two time-steps, which are called stages. Then these evaluations are used to compute the value for the next time step. The first derivative of the variable to be integrated has to be coded as a function which depends on the integrating variable itself and time, as shown in Equation (5.1)

$$\frac{du}{dt} = F(u,t) \tag{5.1}$$

The generic structure of a Runge-Kutta (RK) method includes the evaluations at the different stages of the integrating function, shown as k_1 in Equation (5.2), and represents the following expression in Equation (5.3). The coefficients used to combine and compute the next time step are shown as, a, b, and c. The difference between two RK methods is the value of these coefficients. However, not all values result in usable numerical schemes. For a Runge-Kutta method to be consistent, and zero-stable, the coefficients must obey the following rules in Equation (5.4).

$$u_{n+1} = u_n + \Delta t \sum_{i=1}^{s} b_i k_i \tag{5.2}$$

$$k_i = F(u_n + \Delta t \sum_{j=1}^{s} a_{ij} k_i, t_n + \Delta t c_i) \tag{5.3}$$

$$\sum_{j=1}^{s} a_{ij} = c_i \sum_{i=1}^{s} b_i = 1 \tag{5.4}$$

Where a numerical integration method is said to be consistent when its truncation error, which appears due to the discretisation of the problem, becomes smaller one order faster than the discretisation itself. This can be seen in Equation (5.5), where the time discretisation is represented by Δt and the truncation error by the difference between the numerical and real solutions. In order words, if the error made in a single time-step tends to zero faster than the time step, the method is consistent. The order of a numerical method is then defined as seen in Equation (5.6), where p is the order of the numerical method.

$$\lim_{\Delta t \to 0} \frac{u_n - \mathrm{u}(t_n)}{\Delta t} = 0 \tag{5.5}$$

$$\frac{u_n - \mathrm{u}(t_n)}{\Delta t} = u'_n + o(\Delta t^{p+1}) \tag{5.6}$$

The remaining numerical property mentioned before, the zero-stability of a numerical method, as defined by Hahn (1967), is its ability to sustain numerical perturbations. If two small perturbations very close to each other produce two numerical solutions that are bounded and close to each other, the numerical method is said to be zero-stable. It is a property of the numerical method, rather than the problem that that method is trying to solve.

If a numerical scheme is both consistent and zero-stable, it is said to be convergent. Where convergence implies that the difference between the numerical and real solutions becomes tends to zero when the discretisation is refined, in order words, when the solution is sapled at a higher rate.

$$\lim_{\Delta t \to 0} \frac{u_n - \mathrm{u}(t_n)}{\Delta t} = 0 \tag{5.7}$$

Then, a complete Runge-Kutta method is defined by its coefficients. These are ordered in a matrix, called Butcher's tableau, defined by Butcher (1987), where general characteristics and properties of the method can be inferred. The most distinct property that can be inferred from the Butcher's tableau is whether the method is explicit or implicit. If the matrix is both lower triangular and all the terms in its diagonal are zero, the method is explicit, since no data from posterior stages is used for the current stage.

Table 5.1: Butcher's tableu, as defined by Butcher (1987)

c_1	a_{11}	$\cdots$	a_{ss}
$\vdots$	$\vdots$	$\ddots$	$\vdots$
c_s	a_{s1}	$\cdots$	a_{ss}
	b_1	$\cdots$	b_s

Variable-step methods are numerical integration methods where the time discretisation changes over time, which turns out to be quite useful when numerical instabilities show up. The increasing error is detected by the integrator and the time step is reduced accordingly. The general formulation for the variable time-step assignation, as shown in Equation (5.8), uses the truncation error between to time-steps to estimate whether the current solution is converging or diverging. If the numerical scheme, as explained before, is convergent, a reduced time-step would reduce the truncation error. This truncation error is usually estimated by computing two solutions of two different orders. Their difference is then used for the truncation error estimation and then, the new time step is computed.

$$\Delta t_{n+1} = n \Delta t_n \left(\frac{T_{err_n}}{T_{err_{n+1}}} \right)^{\frac{1}{p+1}} \tag{5.8}$$

Concerning the two numerical-integration methods to be implemented in the software, the Butcher's tableau that describes the DOPRI5 algorithm is shown in Table 5.2. The DOPRI8 Butcher's Tableau can be consulted in the papers by Prince and Dormand (1981) or in the book by Montenbruck and Gill (2000).

5.2. Chebyshev Polynomials

The Chebyshev polynomials are a set of polynomials that minimise the interpolation error when they are used to interpolate a set of data. They are commonly used for the computation of the ephemeris. The problem lies on the fact that these data are usually provided at evenly distributed epochs. A least squares fit is used to transform the data coefficients to the desired distribution for the Chebyshev polynomials.

The n^{th} order polynomial is defined with the following expression in Equation (5.9).

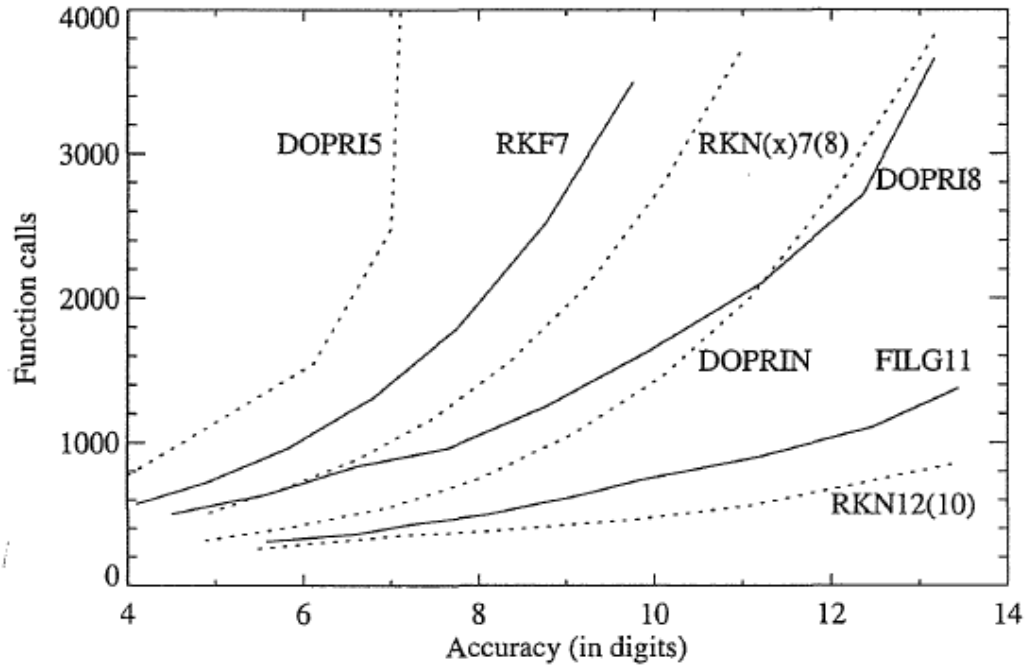

Figure 5.1: Comparison of RK Methods by Montenbruck (1992)

Table 5.2: RKDP5(4)7 Butcher's tableau, by Prince and Dormand (1981)

0	0	0	0	0	0	0	0
$\frac{1}{5}$	$\frac{1}{5}$	0	0	0	0	0	0
$\frac{3}{10}$	$\frac{3}{10}$	$\frac{9}{40}$	0	0	0	0	0
$\frac{4}{5}$	$\frac{44}{45}$	$-\frac{56}{15}$	$\frac{32}{9}$	0	0	0	0
$\frac{8}{9}$	$\frac{19372}{6561}$	$-\frac{25360}{2187}$	$\frac{64448}{6561}$	$-\frac{212}{729}$	0	0	0
1	$-\frac{9017}{3168}$	$-\frac{335}{33}$	$\frac{46732}{5247}$	$\frac{49}{176}$	$-\frac{5103}{18656}$	0	0
1	$\frac{35}{384}$	0	$\frac{500}{1113}$	$\frac{125}{192}$	$-\frac{2187}{6784}$	$\frac{11}{84}$	0
4^{th}	$\frac{35}{384}$	0	$\frac{500}{1113}$	$\frac{125}{192}$	$-\frac{2187}{6784}$	$\frac{11}{84}$	0
5^{th}	$\frac{16}{135}$	0	$\frac{7571}{16695}$	$\frac{393}{640}$	$-\frac{92097}{339200}$	$\frac{187}{2100}$	$\frac{1}{40}$

$$T_n(\tau) = \cos(n \arccos(\tau)) \tag{5.9}$$

An interesting property is the fact that the Chebyshev polynomials can be recursively computed, avoiding the trigonometrical functions, using the following recursive law stated in Equation (5.10).

$$\begin{aligned} T_0(\tau) &= 1 \\ T_1(\tau) &= \tau \\ T_{n+1}(\tau) &= 2tT_n(\tau) - T_{n-1}(\tau) \end{aligned} \tag{5.10}$$

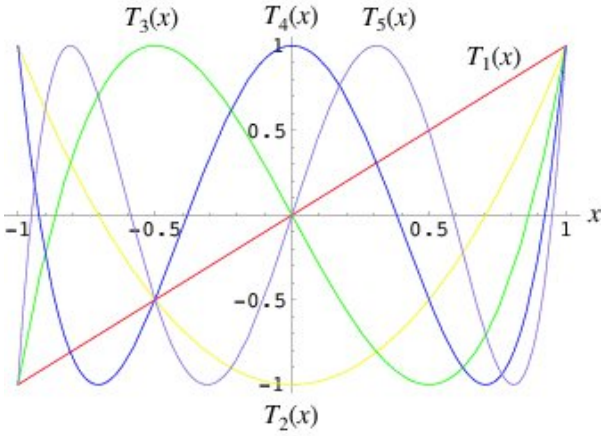

Figure 5.2: Plot of the first five Chebyshev polynomials

The interesting property of these polynomials lies on their behaviour in the $[-1, 1]$ interval. The roots of the Chebyshev polynomials, which can be calculated using the formula in Equation (5.11), concentrate to the ends, as seen in Figure 5.2.

$$\tau_k^n = \cos\left(\frac{\pi(2k+1)}{2n}\right) \text{ for } k = 0, ..., n-1 \tag{5.11}$$

Chebyshev nodes bound the maximum values of the pi function in the chosen interval to a certain value. Different choices of the interpolation nodes lead to uneven distributions of the maxima of this function. This property ensures that the whole interpolation error is evenly distributed along the complete interpolated interval. The interval, in which the polynomials are used, is simply stretched/shorten to fit the interesting $[-1, 1]$ interval, were t_f and t_0 are the ends of the interpolated arc.

$$\tau = \frac{t - \frac{1}{2}(t_f + t_0)}{\frac{1}{2}(t_f - t_0)} \tag{5.12}$$

Then, the ephemeris can be approximated in the desired arc using the recursive function stated in Equation (5.10). The number of arcs and the degree of precision are two parameters that must be defined before the interpolation. The derivative of the interpolated ephemeris can be approximated by a simple expression and the derivatives of the Chebyshev polynomials, as shown in Equation (5.13), which results in a simple expression for the velocity, shown in Equation (5.14). This avoids performing the fitting of the nodes for the velocity as well.

$$\begin{aligned} \dot{T}_0(\tau) &= 0 \\ \dot{T}_1(\tau) &= 1 \\ \dot{T}_{n+1}(\tau) &= 2T_n(\tau) + 2t\dot{T}_n(\tau) - \dot{T}_{n-1}(\tau) \end{aligned} \tag{5.13}$$

$$\dot{x}(t) \approx \frac{2}{t_f - t_0} \sum_{j=1}^{N} a_j \dot{T}_j \tag{5.14}$$

5.3. Cholesky Decomposition

The Cholesky decomposition, as described by Tapley et al. (2004), is a property of the definite positive symmetric matrices discovered by the mathematician André-Luis Cholesky, in which these kinds of matrices can be decomposed into a pair of triangular matrices. It is of key importance for the SRIF algorithm, described in Section 4.2, since the algorithm propagates the pseudo-square-root of the information matrix. This pseudo-square-root is computed by the Cholesky decomposition, whose internal dependencies can be used to recompose the information matrix and thus, the covariance matrix.

$$\begin{aligned} \mathbf{M} &= \mathbf{R}^T \mathbf{R} \\ \mathbf{M}^{-1} &= \mathbf{S}\mathbf{S}^T \\ \mathbf{S} &= \mathbf{R}^{-1} \end{aligned} \tag{5.15}$$

The main use of this decomposition is for covariance propagation in navigation filters, as shown in Section 4.2. Since the propagated matrix is a pseudo-square-root of the covariance matrix, and in case the covariance matrix is badly conditioned, the numeric performance is increased. The $\mathbf{M}$ matrix is decomposed into a upper triangular matrix $\mathbf{R}$, as it can be seen in Equation (5.15), and the complete algorithm is shown in Equation (5.16).

$$\begin{aligned} r_{11} &= \sqrt{M_{11}} \\ r_{ii} &= \sqrt{M_{ii} - \sum_{k=1}^{i-1} r_{ki}^2} \\ r_{ij} &= \frac{\sqrt{M_{ii} - \sum_{k=1}^{i-1} r_{ki} r_{kj}}}{r_{ii}} \text{ for } j = i+1, \ldots, n \end{aligned} \tag{5.16}$$

In case the inverse is preferred over the standard decomposition, the elements of the S matrix are obtained from the expansion of SR=I and are shown in Equation (5.17). This method requires fewer operations than the regular matrix inversion. The $\mathbf{S}$ matrix is needed when the final covariance matrix is outputted.

$$\begin{aligned} s_{ii} &= \frac{1}{r_{ii}} \\ s_{ij} &= -s_{jj} \sum_{k=1}^{i-1} r_{kj} s_{ik} \text{ for } j = i+1, \ldots, n \end{aligned} \tag{5.17}$$

5.4. Givens Orthogonal Transformation

Givens transformations are a set of orthonormal matrix rotations that turn a matrix into upper triangular, as described by Montenbruck and Gill (2000). These transformations are core of the information updates in the SRIF algorithm, as described in Section 4.2. The transformations follow the next structure, $\mathbf{TA} = \mathbf{A}'$,where $\mathbf{A}$ is the matrix to be transformed by $\mathbf{T}$, and $\mathbf{A}'$ is the transformed upper triangular matrix.

The working principle of the transformation consists on rotations, which are applied to the working matrix. These rotations are selected so that in the new coordinate system the transforming matrix becomes triangular. The actual rotation, shown in Equation (5.18), does not need to be estimated. The resultant matrix can be obtained without computing the rotation that transforms the original matrix into the desired one, as shown in Equation (5.19).

$$\begin{pmatrix} A'_{ij} \\ A'_{kj} \end{pmatrix} = \begin{bmatrix} \cos\theta_{jk} & \sin\theta_{jk} \\ -\sin\theta_{jk} & \cos\theta_{jk} \end{bmatrix} \begin{pmatrix} A_{ij} \\ A_{kj} \end{pmatrix} = \begin{pmatrix} \sqrt{A_{ij}^2 + A_{kj}^2} \\ 0 \end{pmatrix} \tag{5.18}$$

$$\begin{pmatrix} \cos\theta_{jk} \\ \sin\theta_{jk} \end{pmatrix} = \frac{1}{\sqrt{A_{ij}^2 + A_{kj}^2}} \begin{pmatrix} A_{ij} \\ A_{kj} \end{pmatrix} \tag{5.19}$$

The complete transformation is done sequentially, zeroing row by row. Since this transformation is sequential, the complete Givens transformation can be expressed the matrix product of all individual rotations, as depicted in Equation (5.20). A schematic of this process, extracted from Montenbruck and Gill (2000), is shown below in Equation (5.21).

$$(\mathbf{T}_N \mathbf{T}_{N-1} \ldots \mathbf{T}_2 \mathbf{T}_1)\mathbf{A} = \mathbf{A}' \tag{5.20}$$

$$\begin{bmatrix} x & x & x \\ x & x & x \\ x & x & x \end{bmatrix} \xrightarrow{\mathbf{T}_1} \begin{bmatrix} x & x & x \\ 0 & x & x \\ x & x & x \end{bmatrix} \xrightarrow{\mathbf{T}_2} \begin{bmatrix} x & x & x \\ 0 & x & x \\ 0 & x & x \end{bmatrix} \xrightarrow{\mathbf{T}_3} \begin{bmatrix} x & x & x \\ 0 & x & x \\ 0 & 0 & x \end{bmatrix} \tag{5.21}$$

Chapter 6
Software Design, Verification, and Validation

The following chapter describes the design, implementation, and validation and verification of the software tool, on which the work of this MSc Thesis will be carried out. The chapter starts by describing the architecture of the software tool in Section 6.1. The main block, into which the software can be divided, are described and the major interactions among them are stated, e.g., inputs, outputs, and parameters.

The description of the algorithm implementation will follow in Section 6.2. These algorithms have already been discussed on Chapter 4 and Chapter 5, but some particularities have to be taken into consideration for their implementation. These will be stated and described. This chapter will end with the validation and verification of the software in Section 6.3. The most relevant tests and results will be depicted and discussed.

6.1. Software Design

This MSc Thesis deals with navigation analyses which are carried out in a software environment. This software shall be in charge of the simulation of the SC dynamics around Didymos and the navigation parameter estimation. This software was built using the architecture of a pre-existing GMV software framework, called Filtering and Estimation Toolbox (FEST). It also incorporates the know-how of another two GMV software tools, SBNav and INTNAV, whose results were exposed by Branco et al. (2016). These toolboxes and what has been reused from them is further described in Appendix C.

A general schematic of the software is shown in Figure 6.1. The architecture of the software is organised into four main blocks and an extra block where all libraries have been included.

Input which makes up the interface between the software and the used. This interface is composed of two files. The mission configuration files, which describes the scenario to be run and loads all constants to be used. And secondly, the filter configuration file, where, among other things, the parameters to be estimated are selected and the navigation filter is selected and pre-configured. The list of sensors to be used in this simulation is also present in the input files. These are selected and fed into the simulator.

Pre-processing is layer of the software that is in charge of handling the data in the configuration files, and adapt it to readable variables for the simulator. As an example of what is done: flags which activate or deactivate sections of the code are constructed, landmarks are generated and pre-processed, etc.

Simulator which comprises the core of the software. It follows a circular data flow. First the SC trajectory in the real world is computed. Then, the sensor measurements are simulated. This information enters the navigation filter, which uses this information to reconstruct the trajectory and estimate various parameters. Lastly, if a manoeuvre is required it is computed and fed back into the loop.

Post-processing in charge of gathering the internal information in the simulator, and process it to an understandable format. Navigation error, residuals, covariance analysis, among other parameters, are calculated and plotted.

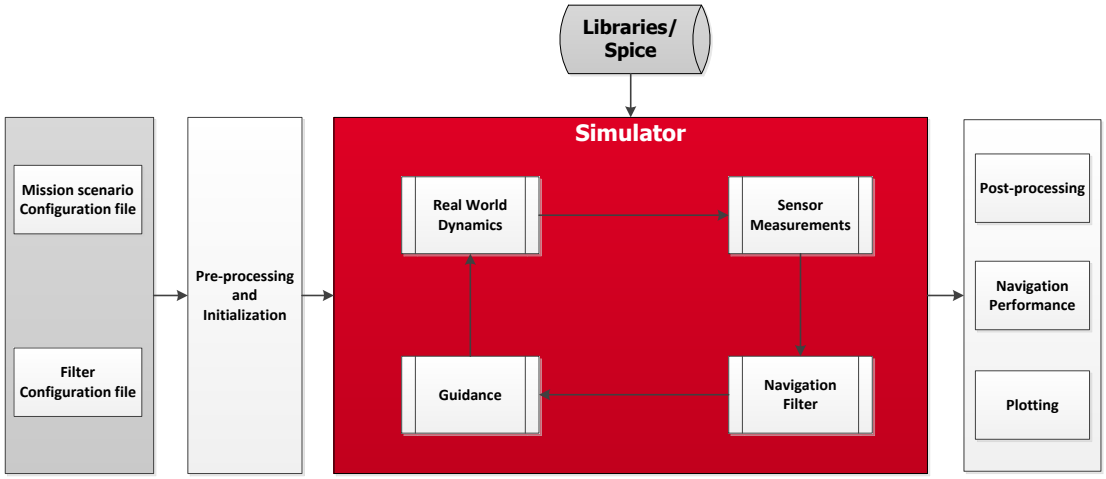

Figure 6.1: High-level structure of the Simulator

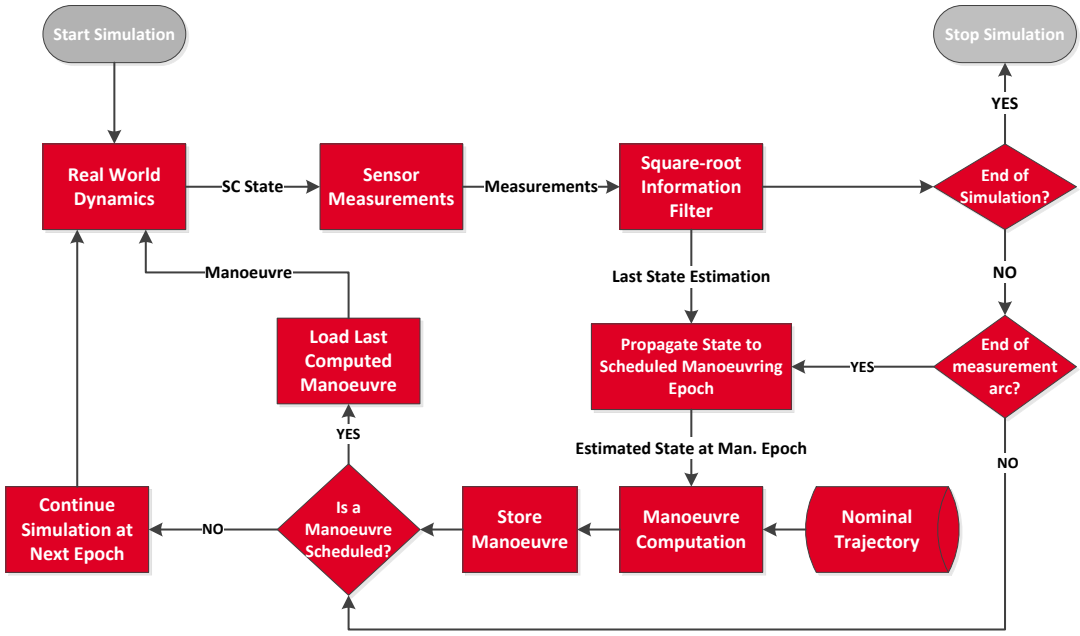

Figure 6.2: Mid-level structure of the Simulator

The most complex and extensive part of the software is the simulator. The simulator is mainly composed of four parts: the real world, the sensors, the filter, and the guidance; which connect to each other forming an information loop, which is repeated until the simulation is finished. These blocks are summarised below, and a schematic of the information flow can be seen in Figure 6.2.

- Real World

  Inputs epoch, previous SC state and manoeuvres.

  Parameters dynamical constants and ephemerides.

  Description the real world block is in charge of simulating the complete environment in the Didymos system that rule the dynamics of the AIM SC, and reproduces its trajectory.

  Outputs SC real state.

- Sensors

  Inputs epoch and SC real state.

  Parameters noise, biases, and parameters for each sensor.

  Description the sensors block simulates the output of all selected sensors and feeds these computed measurements to the navigation filter.

  Outputs measurements with and without errors.

- Navigation Filter

  Inputs epoch, previous SC state estimate and covariance and measurements.

  Parameters filter configuration parameters.

  Description the navigation filter oversees the estimation of the whole state of the spacecraft and the dynamical parameters of the system. Measurements and dynamics are used to reconstruct the trajectory and filter and remove errors.

  Outputs SC state estimate and covariance and estimated parameters.

- Guidance

  Inputs epoch and SC state estimate.

  Parameters manoeuvre schedule and reference trajectory.

  Description the manoeuvre block receives the SC estimate and performs the necessary calculations to compute a correction manoeuvre.

  Outputs manoeuvre with and without errors.

6.2. Software Development and Implementation

In Chapters 3, 4, and 5 the theoretical basis of all algorithms to be implemented has been exposed. Here in this chapter, the design and implementation of the software is displayed and discussed.

6.2.1. Real World

The real world has been implemented by making a function which models the dynamics of the AIM spacecraft. This function expresses the acceleration on the vehicle as a function of the current SC state and the epoch, as shown in Equation (6.1). This function is converted into a set of six ordinary differential equations (ODE), as can be seen in Equation (6.2), three for the position and the remaining three for the velocity. Then, these equations are integrated using a numerical integrator, as discussed in Section 5.1.

$$\frac{d\mathbf{x}}{dt} = F(\mathbf{x}, t) \tag{6.1}$$

$$\begin{aligned}\frac{d\mathbf{r}}{dt} &= \mathbf{V} \\ \frac{d\mathbf{V}}{dt} &= \mathbf{a}_{CBF} + f_{SRP}\mathbf{a}_{SRP} + f_{3BS}\mathbf{a}_{3BS} + f_{3Bd}\mathbf{a}_{3Bd} + \dots \\ &\quad \dots + f_{NSGD}\mathbf{a}_{NSGD} + f_{NSGd}(\mathbf{a}_{NSGd} - \mathbf{a}_{NSGd/D})\end{aligned} \tag{6.2}$$

6.2.2. Sensors

The sensor measurements are computed accordingly to the models exposed in Section 4.1. These models are in charge of simulating the performance of the real sensors and observations. These real measurements always carry errors, which come from many sources and behave in different ways. Two typical error sources have been included in these performance models, as shown in Equation (6.3). These are: biases, shown as b, and white noise, n, modelled as Gaussian noise with zero expectancy and σ standard deviation.

$$Y_{meas} = Y_{real} + b + n \tag{6.3}$$

6.2.3. Navigation Filter

The mathematics and working principles of the selected navigation filter, the square root information filter, have been described and analysed in Section 4.2. The filter was adapted to work as a hybrid batch-sequential estimator, to reproduce the work by Parisi et al. (2012) and Genova et al. (2012), where ordinary sequential and batch estimators are understood as the following:

Sequential Measurements are incorporated into the filter as soon as they are collected, one by one or in small batches. The main advantage of these filters is the ability to generate time ordered solutions based on a minimum amount of data and the information from previous estimations (from covariance or from information matrices). The main disadvantage is the sensitivity to locally bad conditioned data that can eventually cause the filter divergence and require a certain stabilisation period to recover a stable solution. To minimise this effect one can implement a local batch process for the new dataset to detect bad conditioned data before the observations are incorporated into the estimation process.

Batch All measurements are incorporated simultaneously and a one-shot solution is obtained after an iterative algorithm over the whole dataset. The advantage of the process the fact that all data can be relatively weighted and processed together with high robustness. The main disadvantage is the need to wait until all data has been collected before the process can start. Additionally, bad conditioned portions of the data can degrade the solution of the whole process if not edited out efficiently. The best way to improve the processing is by providing initial conditions as close as possible to the final expected solution to minimise the number of iterations. However, bad conditioned data can take the filter away from the solution and increase the number of iterations until the bad data has been removed.

Batch-sequential estimators are, by definition, a middle solution between these two types of estimators. Measurements are organised in small batches which are processed as if it were a complete batch estimation. Then, the updated state is propagated, as in sequential estimator, to fill for the next batch of measurements. As with the batch estimators, the disadvantage of having to wait until all measurements for the batch have been collected is present, nevertheless, this is mitigated. The state can be outputted much frequently, while keeping the robustness of the batch estimator.

Two main working modes are established for the filter. The first one, resembling closely to sequential estimators, consists on using the state update, once the measurement batch has been processed, directly for the next batch. The second mode, closer to the working principles of batch estimators, the update is fed back into the same batch, until a convergence criteria is met. Then, this new update is propagated for the next batch of measurements.

Derivative calculation

Partial derivatives of a function $\mathbf{F}$, with respect to one of the parameters it depends on, are computed numerically. These derivatives are computed using a centred finite differences method, as shown in Equation (6.4). The step used for the computation, $\Delta\beta$ as shown in Equation (6.5), is proportional to the scale of the parameter β by a factor α, which was selected to be between 10^{-3} and 10^{-5}, with 10^{-4} as the most typical value. Central finite differences are chosen over backward and forward finite differences because the truncation error is of a higher order, second vs first order, which improves a lot the preciseness of the method, using the exact same amount of function evaluations.

$$\frac{d\mathbf{F}}{d\beta} = \frac{\mathbf{F}(\beta + \Delta\beta) - \mathbf{F}(\beta - \Delta\beta)}{2\Delta\beta} \tag{6.4}$$

$$\Delta\beta = \alpha\beta_{scale} \tag{6.5}$$

These derivatives are later combined to make the observation and transition matrices. In the case of the transition matrices, the previously mentioned generic vectorial function, $\mathbf{F}$, is the propagated state $\mathbf{x}(t_f)$. Thus, the complete calculation consists on introducing a perturbation $\Delta\mathbf{x}_i(t_0)$ on one of the state coordinates, x_i, and propagate this new state into the new epoch t_f. This results on a vector, as shown in Equation (6.6), which is composed of the partial derivatives of all state coordinates with respect to the x_i parameter. The matrices are constructed column by column, computing all derivatives with respect to all variables in the state vector in the way shown in Equation (6.7).

$$\frac{d\mathbf{x}(t_f)}{dx_i(t_0)} = \frac{\mathbf{x}(t_f)(\mathbf{x}(t_0) + \Delta\mathbf{x}_i(t_0)) - \mathbf{x}(t_f)(\mathbf{x}(t_f) - \Delta\mathbf{x}_i(t_0))}{2\Delta x_i(t_0)} \tag{6.6}$$

$$\mathbf{\Phi}(t_f, t_0) = \left[\frac{d\mathbf{x}(t_f)}{dx_1(t_0)} \quad \cdots \quad \frac{d\mathbf{x}(t_f)}{dx_n(t_0)}\right] \tag{6.7}$$

The same schematic is followed to construct the observation matrix, as shown in Equation (6.8), where the derivatives of each measurement with respect to the state are computed, and Equation (6.9), where the complete matrix is constructed.

$$\frac{d\mathbf{Y}}{dx_i} = \frac{\mathbf{Y}(\mathbf{x} + \Delta\mathbf{x}_i) - \mathbf{Y}(\mathbf{x} - \Delta\mathbf{x}_i)}{2\Delta x_i} \tag{6.8}$$

$$\frac{\partial\mathbf{Y}}{\partial\mathbf{x}} = \left[\frac{d\mathbf{Y}}{dx_1} \quad \cdots \quad \frac{d\mathbf{Y}}{dx_n}\right] \tag{6.9}$$

Measurement processing

The measurements are processed in the filter via the inclusion of the a-priori residuals and the observation matrix. These two are computed as depicted in Equation (6.10). These are, in turn, weighted by the square root of the a-priori inverse covariance matrix of the measurements, $\mathbf{R}_Y$. This weighting is performed to both increase the influence of the most precise measurements and to provide weighted residuals whose standard deviation is 1. This last is one of the most important properties of the statistical basis of the SRIF algorithm, as described by Tapley et al. (2004). The function $\overline{\mathbf{Y}}$ is the internal filter estimation of what the measurements should be if the SC state were the a-priori state estimate.

$$\begin{aligned} \mathbf{y} &= \mathbf{R}_Y\left(\mathbf{Y} - \overline{\mathbf{Y}}(\overline{\mathbf{X}}, t))\right) \\ \mathbf{H} &= \mathbf{R}_Y\frac{\partial\mathbf{Y}}{\partial\mathbf{x}} \end{aligned} \tag{6.10}$$

House-holder transformations have the property of processing rows either all together or in whatever possible order, remaining the result unaffected by any of these possibilities. This commutability is key for the measurement update in the SRIF algorithm. Thus, all measurements can be processed in one single batch, as shown in Equation (6.11), without any change in the resulting updated state.

$$\begin{bmatrix} \mathbf{H}_1 & y_1 \\ \mathbf{H}_2 & y_2 \\ \vdots & \vdots \\ \mathbf{H}_n & y_n \end{bmatrix} = \begin{bmatrix} \mathbf{H} & \mathbf{y} \end{bmatrix} \tag{6.11}$$

These measurements are processed in one single batch by constructing the the matrix in Equation (6.12). This structure is analogous to that used by Genova et al. (2012) and Parisi et al. (2012) for the navigation of the Bepicolombo mission. Three distinctive areas can be identified. The one on the left, containing only elements along the diagonal, which represents the local parameters at each epoch in the complete batch. The following area, to the right, is composed of the so called global parameters, in this case represented by all constant parameters which are common for the complete batch, and thus, affect all epochs equally. The remaining column is composed of all information vectors at all epochs and the measurements.

$$\begin{bmatrix} \overline{\mathbf{R}}_{px_1} & 0 & 0 & \overline{\mathbf{R}}_{pxc_1} & \overline{\mathbf{z}}_{px_1} \\ 0 & \ddots & 0 & \vdots & \vdots \\ 0 & 0 & \overline{\mathbf{R}}_{px_n} & \overline{\mathbf{R}}_{pxc_n} & \overline{\mathbf{z}}_{px_n} \\ \mathbf{H}_{px_1} & 0 & 0 & \mathbf{H}_{c_1} & \mathbf{y}_1 \\ 0 & \ddots & 0 & \vdots & \vdots \\ 0 & 0 & \mathbf{H}_{px_n} & \mathbf{H}_{c_n} & \mathbf{y}_n \end{bmatrix} \tag{6.12}$$

These global parameters are later processed in the same way as described in Section 4.2, as shown in Equation (6.13) using the processed data in Equation (6.12). The resulting estimated residual vector $\mathbf{e}$ in Equation (6.14) is evaluated to assess whether another iteration is necessary and the new update must be fed back to compute a new observation matrix and residuals. Since, due to the before mentioned property dealing with the standard deviation of the residuals, the magnitude of a converged residual vector is known beforehand, the convergence is easily assessed by just looking at the final values of the $\mathbf{e}$ vector. Thus, no extra calculation of the a-posteriori residuals is needed.

$$\begin{bmatrix} \overline{\mathbf{R}}_c & \overline{\mathbf{z}}_c \\ \tilde{\mathbf{H}}_{c_1} & \mathbf{y}_1 \\ \vdots & \vdots \\ \tilde{\mathbf{H}}_{c_n} & \mathbf{y}_n \end{bmatrix}_k \tag{6.13}$$

$$\begin{bmatrix} \tilde{\mathbf{R}}_c & \tilde{\mathbf{z}}_c \\ 0 & \mathbf{e} \end{bmatrix}_k \tag{6.14}$$

6.2.4. Guidance

The guidance block is mainly composed of the FTOA algorithm described in Section 4.3. Its objective is to compute a manoeuvre that corrects the trajectory of the spacecraft. These manoeuvres are scheduled beforehand, thus, the epochs at which the manoeuvres will occur are initialised with the complete simulation. A reference trajectory is uploaded to the simulator. The algorithm calculates the ΔV needed at the manoeuvre epoch to arrive at a certain point in a certain amount of time. These points are selected to be the next manoeuvre nodes, so that the spacecraft arrives with the minimum possible error to the next manoeuvring point.

Since the algorithm is based on linearised equations, the resulting ΔV will not modify the trajectory as expected. Thus, an iterative approach is used and the new starting point is fed back into the FTOA algorithm, which returns a smaller ΔV which further corrects the deviations. This is done until a certain convergence criteria is met.

This ΔV is converted into a acceleration by a simple approximation. Since these manoeuvres are approximated as an instantaneous change in velocity, the total ΔV would be computed as shown in Equation (6.15), which can be simplified into Equation (6.16).

$$\Delta \mathbf{V} = \lim_{\Delta t \to 0} \int_0^{\Delta t} \mathbf{a}_T \, \mathrm{d}t \tag{6.15}$$

$$\mathbf{a}_T \approx \frac{\Delta \mathbf{V}}{\Delta t} \tag{6.16}$$

Thus, at the end of the integration step, the ΔV will have been applied to the velocity, but errors, due to the non-instantaneous manoeuvre, will be present. This solution is preferred, over an instantaneous change in the velocity, because this acceleration can be introduced into the filter as an acceleration measured by the SC's IMU.

Once the manoeuvre has been computed, the errors associated to its mechanisation are simulated. Firstly, the linear approximation is conducted. If the computed covariance matrix has one negative eigenvalue, a Monte-carlo run is executed to recompute it.

6.3. Software Validation and Verification

In this section, the Validation and Verification plan and its execution for this MSc Thesis software will be outlined and described. The methodology used is based on the European cooperation for space standardisation (ECSS), summarised in document ECSS-E-ST-40C[1], which describes what a software validation and verification plan should be like.

6.3.1. Validation and Verification Plan

The validation and verification process is approached in three different manners, depending on the character of the functions to be validated. The first set of functions corresponds to those, which are generally used by the engineer to build and test the GNC system designs, and, more or less, compose the core of the simulator by themselves. These are:

Real world SC dynamics around Didymos, DOPRI5, DOPRI8, Didymoon ephemeris generation and storage, etc.

Sensors Range, Doppler, DDOR, centroiding, landmark matching, altimeter, operational availability, etc.

Navigation Filter SRIF algorithm, Cholesky decomposition, House-holder transformation, partial-derivatives calculation, etc.

Guidance FTOA algorithm, manoeuvre calculation, dispersion propagation, ground-knowledge propagation, operations, etc.

Post-processing measurement residuals, navigation error, LM-post processing, nav-camera live-views, LM visualisation.

These functions are characterised to be built from the scratch. Thus, its treatment towards the validation and verification of the software is much different from those from the second category. This following category comprises those that are not in charge of any simulation, and its purpose is to facilitate the work with the simulator, in other words, those functions in charge of the interaction with the user:

[1] can be consulted on http://wwwis.win.tue.nl/2R690/doc/ECSS-E-ST-40C(6March2009).pdf

- Building functions (scenario definition)
- Executing functions
  - Single Run
  - Monte Carlo
- Storage functions

This set of functions mainly correspond to the building architecture of the software, which are mostly inherited from the FEST simulator. Only minimal modifications were done on them to accommodate the new simulator into the old architecture. Last, but not least, a third group of functions were included in the simulator. These are the external libraries, e.g., Spice Kernel, which have long been validated and do not need to undergo any validation process. Nevertheless, verification is still needed, to check whether these functions comply with that is needed of them.

Five Validation and Verification methods will be combined to ensure the proper functioning of the software. Among the five of them, test would be the preferred option. However, design tests for all the designed modules is not optimal. Thus, this technique will be reserved for the most critical parts of the software, leaving for the others quicker validation methods. These are described below:

Inspection the simplest of all methods. It consists on the visual identification of the code.

Review the design of the software is revisited and checked against the implemented code.

Analysis it consists on applying theoretical knowledge to evaluate the performance of the software.

Demonstration the software is run with all its input parameters, and the results are checked to observe any anomalies in the expected output.

Test which consists on the most extensive validation method. The software undergoes a set of specific test scenarios which are representative of the simulated function and whose results are known. Thus, the software is said to be validated if those results are reproduced.

The validation and verification process underwent three stages. Verification was run along all phases, checking that all tests were relevant and truly verify the software. The stages, into which the validation was divided, are depicted below in Figure 6.3. This started at the lowest level, where the unitary validation of the functions was carried out. This was done parallel to the implementation process, which was intended to mitigate the effect that errors could have on the schedule. Due to the fact that the sooner errors were detected, the less their impact was.

Figure 6.3: Validation sequential planning

The functional validation followed, for which unitary-level validation was carried out as well, but not as extensively as in the previous stage. This was intended to verify that the behaviour did not change during the integration of the higher-level functions. The same philosophy will be applied once the integration has been completed, for the complete validation of the software.

This transition between the low and high levels was done in all three validation stages, and it is shown in Table 6.1, where the later stages contain validation on all lower levels. The last validation test will replicate FASTMOPS CCN AIM's navigation assessment, based on the work by Branco et al. (2016), for the final acceptance test of the software. A complete schematic of the V&V process is shown in Figure 6.4.

Table 6.1: Schematic of the validation process

	Unitary Validation	Functional Validation	Software Validation
Unitary Level	x	x	x
Functional Level		x	x
Software Level			x

6.3.2. Unitary Validation

In the lowest level of the software, the unitary functions can be found. These describe a very specific role, from force models to the simplest mathematical operations (cross product of vectors, matrix multiplication, etc.). Most of these models were built over the years and have been inherited from former toolboxes where they were validated. Their continuous use is understood as a proof of their validity. Nevertheless, a proper verification process was carried out, where the reusability of each model was checked.

For most of these inherited functions, simple tests such as 90 degree rotations were carried out, to verify that they work as expected. On the contrary, for functions built from the scratch, test were designed to validate them. Among these, to validate and verify the integrators, a simple harmonic oscillator, such as the one in Equation (6.17), was coded. Since a analytic solution to this equation can be obtained. Three initial conditions were tested, and the difference between the analytic solution and the solution after 10 whole periods is shown in Table 6.2.

$$\ddot{x} = -x \tag{6.17}$$

Table 6.2: Integration error

Error	Scenario 1	Scenario 2	Scenario 3
DOPRI5	$1.132 \cdot 10^{-14}$	$5.520 \cdot 10^{-11}$	$-1.132 \cdot 10^{-14}$
DOPRI8	$8.209 \cdot 10^{-13}$	$-7.157 \cdot 10^{-13}$	$-8.209 \cdot 10^{-13}$

Other important test that were carried out on key functions, such as House-holder transformations, tested with MATLAB functions such as QR and, and the computation of manoeuvre-execution errors. The manoeuvre-execution error covariance calculation was described in Subsection 4.3.3, there an analytic approximation was depicted.

To ensure the validity of this model, whose results are depicted in Table 6.3, 1000 Monte-Carlo simulations were performed for a typical acceleration profile of $7 \cdot 10^{-7}$ [km/s^2] and 3% 3-sigma error in magnitude and 1 deg 3-sigma in direction. The covariance between all runs is shown in Table 6.4. Their close values are taken as a proof of the validity of the model.

Table 6.3: Analytic manoeuvre execution covariance in [km^2/s^4]

$8.07 \cdot 10^{-18}$	0	0
0	$1.18 \cdot 10^{-18}$	0
0	0	$1.18 \cdot 10^{-18}$

Table 6.4: Monte-Carlo manoeuvre execution covariance in [km^2/s^4]

$8.77 \cdot 10^{-18}$	$-3.5 \cdot 10^{-20}$	$4.06 \cdot 10^{-20}$
$-3.5 \cdot 10^{-20}$	$1.18 \cdot 10^{-18}$	$-1.4 \cdot 10^{-20}$
$4.06 \cdot 10^{-20}$	$-1.4 \cdot 10^{-20}$	$1.17 \cdot 10^{-18}$

6.3.3. Functional Validation

The functional validation and verification can be further subdivided into four parts, each corresponding to the four main functional blocks of the simulator, namely: real world, sensors, navigation filter, and guidance.

The complete dynamics model was propagated for a complete DCP 3-day arc. Using the same initial conditions as the AIM's DCP, the difference between the the last position is shown in Table 6.5. An error of meters is observed in position, whereas the error in velocity is negligible. The error in position can be explained by the simple propagation of the error in velocity during the 3-day integration, while the velocity error is directly due to the differences in the dynamics model.

Table 6.5: Benchmark AIM-DCP/Simulator's Real World

Error	X	Y	Z
Position [km]	$3.692 \cdot 10^{-3}$	$3.683 \cdot 10^{-3}$	$-5.319 \cdot 10^{-4}$
Velocity [km/s]	$6.124 \cdot 10^{-10}$	$9.088 \cdot 10^{-9}$	$-5.844 \cdot 10^{-10}$

A noise model for the centroiding algorithm was provided for both DCP and ECP by GMV. Since the DCP model has been selected as the one on which the tests will be based, its noise was replicated using a moving average. Its period was set equal to that of the algorithm's, which in this case was 10 minutes. Using that method, a bias in the measurements and a covariance for each of the two signals was estimated. A comparison between the simulated sensor output and the actual centroiding algorithm error is shown in Figure 6.5. The red dots represent the real error of the algorithm along the four DCP arcs and the blue line is the error of the simulated measurements by the centroiding algorithm.

6.3.4. Acceptance Test

Lastly, as the acceptance test for the software, the complete AIM's Detailed Characterisation Phase (DCP) was replicated. The DCP is composed of four hyperbolic arcs of three, one, two, and one days long, which can be seen in Figure A.1, which is already the output of the simulation. For this simulation only centroiding measurements are used, according to the noise model in Figure 6.5.

In in Figure A.1, it can be seen that the manoeuvre computation algorithm, plus errors, works fine closing the arcs, making the end of the last arc match with the starting position of the first arc, thus validating the actual performance of the implemented guidance. The navigation error is shown in Figure 6.7 for the position and in Figure A.3 for the velocity. The blue line represents the actual error between the navigation estimate and the real position/velocity. The red line is the 1σ knowledge of the filter on the accuracy in position and velocity, respectively.

Some abrupt changes are observed between the third and fourth day of the simulation, which can be related to the manoeuvres that are performed at those epochs. Since the results are expressed in orbital axes and these manoeuvres change the direction of these axes very quickly, no actual abrupt change is present, simply the information in one axis becomes the information in the other.

When compared to the navigation data of the FASTMOPS AIM's Navigation Assessment for DCP, shown in Figure 6.6 for the position and Figure A.2 for the velocity, it can be seen that the output 1σ of the filter, depicted as updates in light blue, is of the same order as the output of this simulator. The filter has been tuned according to that will be exposed in Subsection 7.2.4, and shows a converged solution for a purely sequential estimation. The magnitude of the errors replicate the results in Figures 6.6 and A.2, which were extracted from the SBNav tool, and documented in during AIM's mission design in [AD01].

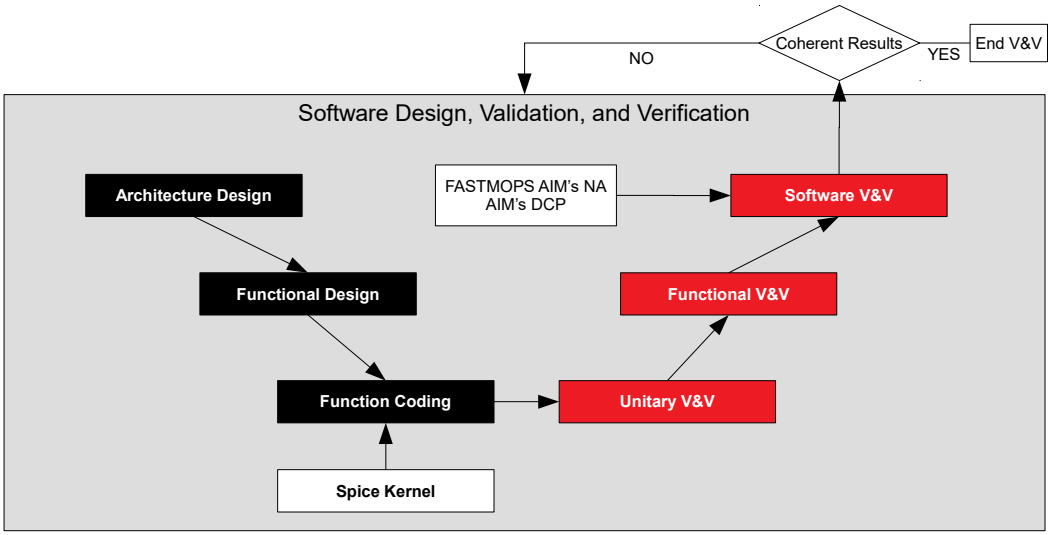

Figure 6.4: Complete DVV schematic of the software

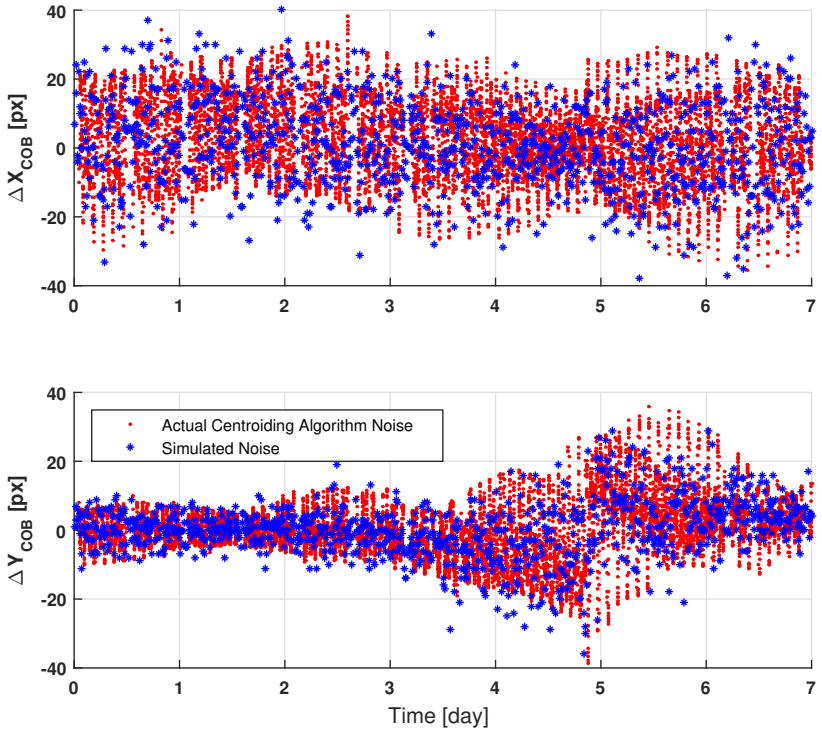

Figure 6.5: Simulated Centroiding Algorithm (Blue) vs Actual Algorithm Performance (Red)

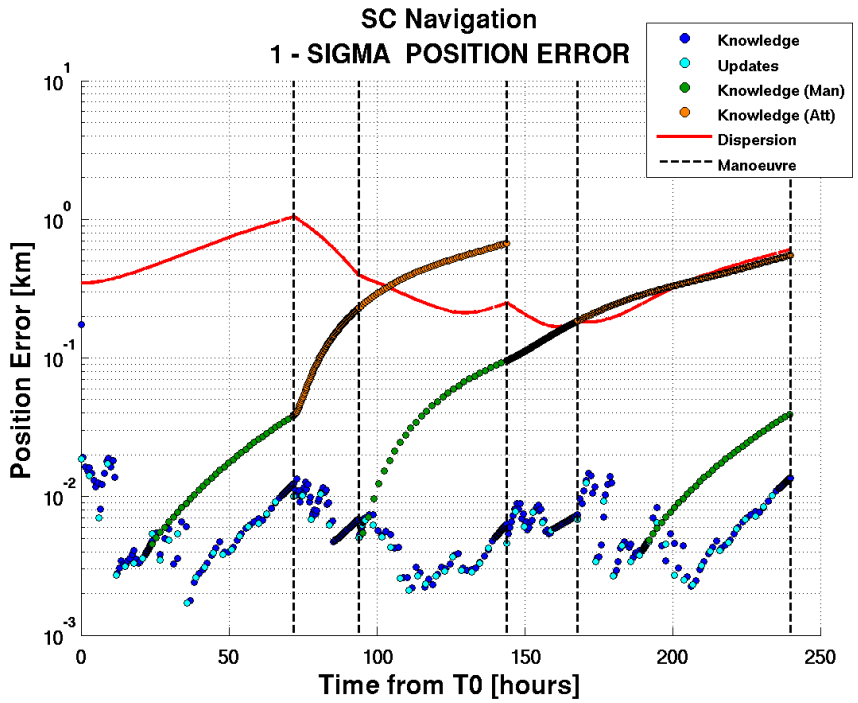

Figure 6.6: AIM's DCP Position Navigation and Guidance Performance for five DCP Arcs as per [AD05]

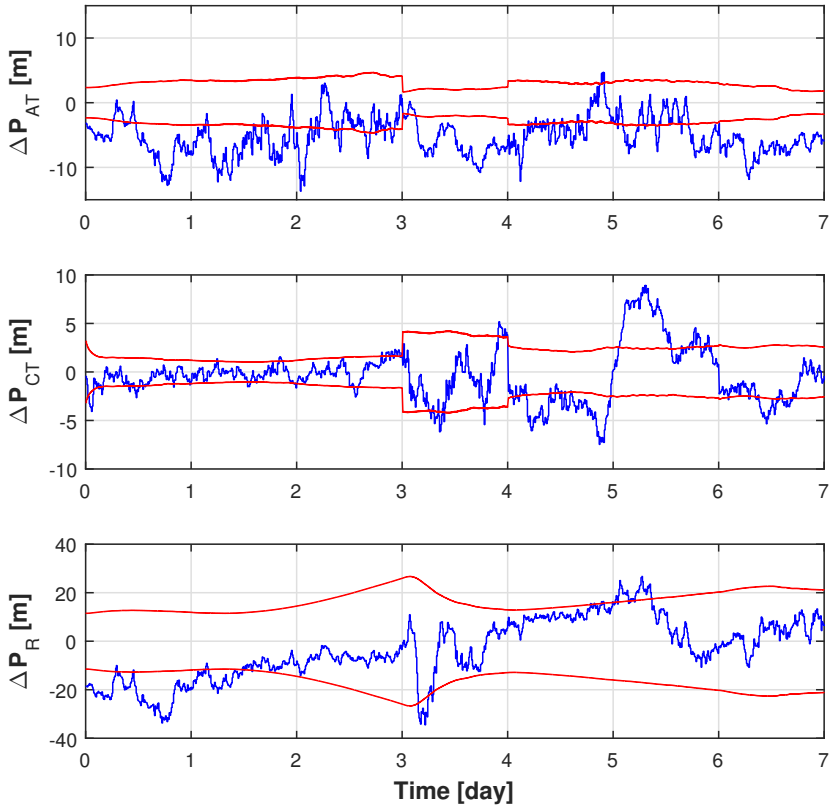

Figure 6.7: Position Navigation Performance for four DCP arcs

Chapter 7
Navigation Problem Analysis

This chapter will outline the MSc Thesis assignment and set the basis for the results, which will be presented in Chapter 8. Firstly, the research question and objective will be presented and explained. Then, the assumptions made for the analyses will be listed, set out, and their rationale will be justified. These assumptions have a direct impact on the navigation parameter estimation.

Thus, how the navigation is affected by the assumptions and constraints will be described. The parameters to be estimated will be listed and the particularities of each one will be discussed. This will result on a first approximation to a navigation strategy, which will be the starting point for all simulations in Chapter 8.

7.1. Research Problem

As it has been previously depicted in Chapter 2, the AIM mission has two heavily-impacting design constraints, which will dictate the complete design of the navigation. These are: the decision of not carrying a steerable HGA and instead opting for a fixed one, and the lack of an altimeter. In previous missions, such as NEAR Shoemaker, Hayabusa, and Rosetta, either of them were present. For NEAR and Hayabusa, a fixed HGA was used but both spacecraft carried an altimeter. On the other hand, an altimeter was not included for Rosetta but a steerable HGA, which guaranteed continuous communications. Thus, continuous measurements on which to reconstruct the orbit were available.

These constraints have a deep impact on the navigation. The lack of an altimeter causes a geometrical problem in the orbit determination, which is called the scale factor problem. The orbit determination cannot properly work with an under-determined and not-observable problem and solutions must be found to correct for it.

These solutions must be found as a part of the navigation strategy design. These are understood as the complete approach and plan for orbit and parameter estimation. Thus, the following question arises:

What navigation strategy delivers the best cost/performance for safe operations and the characterisation of the dynamics around the Didymos binary system with AIM's systems platform

Answering this question will constitute the base objective of this work. Nevertheless, the former can be further divided into more specific questions. These are easier to deal with and answer to. These are:

- *How can the optical-navigation scale-problem of landmark tracking be efficiently solved?*
- *How and to what precision can this scale factor be determined?*
- *To what precision can the unknown dynamical parameters of an asteroid system be estimated during the early characterisation phase of a mission.*
- *To what precision can the mass of the secondary component (Didymoon) be estimated?*
- *What filter parameters drive the performance of the navigation and how can they be optimised?*
- *How can the spacecraft navigate relative to the asteroid without an altimeter?*
- *Does either the fixed HGA or the lack of an altimeter incur in higher operational costs that override their savings?*
- *In what manner can the orbit determination be scheduled without incurring in extra man-hours, and thus cost?*

7.2. Assumptions and Operational Constraints

This section will deal with the assumptions and constraints that directly affect the current work. Firstly, the assumptions on the work scenario, the ECP, will be depicted. Then, the assumptions on the spacecraft's properties will be stated. The section will end with the identification of the to-be-estimated parameters and their classification, depending on how their estimation will be dealt with.

7.2.1. The Early-Characterisation Phase (ECP)

The early-characterisation phase (ECP) is the first of the two characterisation phases and the first proximity phase to Didymos. The ECP was designed with a tight design constraint on the orbital velocity: AIM's velocity could never fall under twice the local escape velocity, to ensure the SC's safety under the yet unknown dynamics. The mission design was carried out by GMV, structuring the phase into four hyperbolic arcs; resulting in an operations design that will repeat over week cycles.

Two four-day arcs will cover Didymain's poles, while the shorter 3-day arcs will go from high latitudes to very low latitudes, joining them two and forming a square shape, as observed in Figure 2.8. Thus, from now on, the arcs will be referred to as either horizontal or vertical arcs. The meeting points of all four arcs are called manoeuvre nodes. These have been listed in Table 7.1. Two arcs Thus, there are two groups of one four-day arc and a three-day arc. This way, the mission schedule can be easily fit into a working week, minimising operational cost.

In Figure 7.2, a frontal picture of the complete ECP is shown, where The Y-axis almost matches the Sun direction. Thus, this view approximately shows the system as seen by the Sun, which is evidenced in Figure 7.1. The spacecraft remains between the Sun and Didymos, which complies with the phase angle constraint. The position of all ECP nodes is shown in Table B.1, but to better understand the characteristics of each one, these data has been converted into more significant variables, as shown in Table 7.1. Two nodes, 1 and 4, are located at high latitudes, while the remaining two are located at low latitudes. The same simetry is observed in longitude, two nodes are located east of the X_{DMJ200} axis, and the remaining two west. The phase-angle of all nodes falls in the safe region.

7.2.2. Constants and assumptions

The assumptions and parameter values used in the simulations are listed in Table 7.2. There, common parameters can be found together with those more particular of the Didymos system.

The gravitational force of each component of the Didymos system, Didymain and Didymoon is characterised by their gravitational parameter μ, which is 34.9 km^3/s^2 for Didymain and 0.328 km^3/s^2 for Didymoon. However, during the simulations, the system will be characterised by its total mass, Didymain plus Didymoon, depicted as Didymos's mass, and the mass of the secondary itself.

Table 7.1: ECP Manoevure nodes

	Node 1	Node 2	Node 3	Node 4
Latitude [deg]	38.46	-50.88	-44.67	41.21
Longitude [deg]	39.34	31.01	-68.32	-49.58
Phase angle [deg]	56.42	61.55	70.93	55.12
Distance [km]	30.00	25.90	30.00	26.52

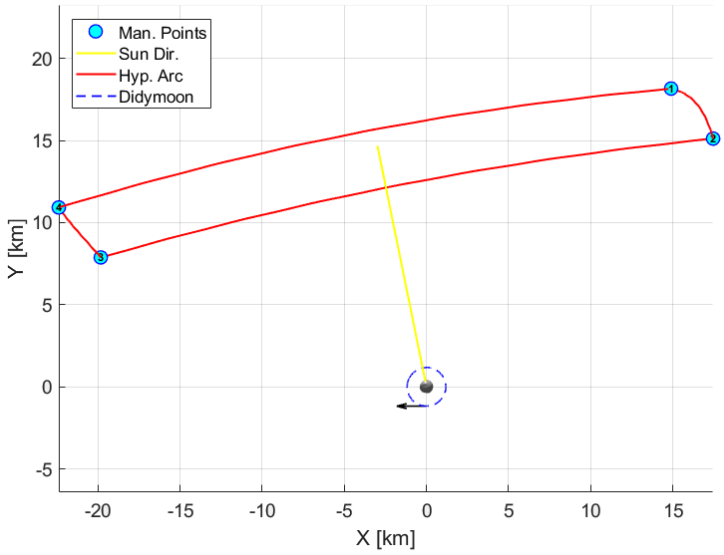

Figure 7.1: Upper view of four ECP hyperbolic arcs in Didymos Ecliptic J2000

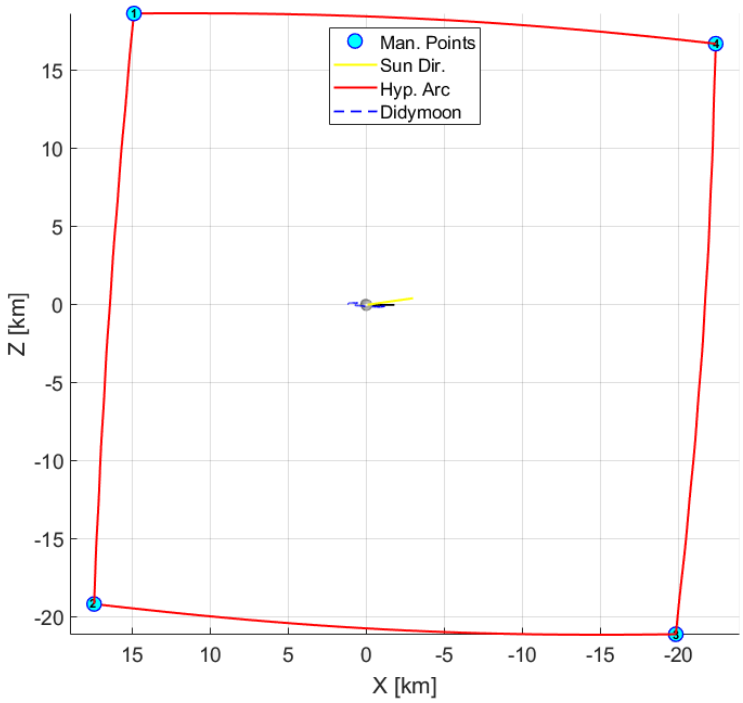

Figure 7.2: Frontal view of four ECP hyperbolic arcs in Didymos Ecliptic J2000

This selection is motivated by the fact that from very far distances the two bodies behave like a single body with the total mass of the system. It is only when the SC approaches the system that these two forces can be differentiated. Thus, since this work deals with the first characterisation stage of the system, the proposed approach has been recognised as the most representative of a first estimation. The terms mass and gravitational parameter will be used interchangeably, since they represent the same quantity scaled by Newton's gravitational constant. The spherical harmonics are derived from a given shape model for Didymain and an ellipsoid for Didymoon, as explained in Chapter 3.

Didymain's rotation axis has a declination of $310°$. Thus, Didymain seems to rotate clockwise when observed from the Didymos Ecliptic-J2000 reference frame. Didymoon's orbit is assumed circular, tidally locked, and contained in the equatorial plane of Didymain, thus rotating in the same direction as the primary. The rotation of Didymain is quite fast, completing a revolution in 2.26h, while Didymoon's translation and rotation period lasts for almost half an Earth-day, 11.92h. These values are extracted from the Didymos Reference Model, as provided by ESOC (2014).

Spacecraft parameters such as mass, reflection coefficient, and cross-section area are also included. These last two parameters are not observable. They always show up in the equations as their product. Thus, they cannot be estimated separately, and an effective area, whose value is 7.5 m^2, replaces them in the estimation process.

7.2.3. Navigation parameter estimation

Regarding the navigation, and as explained in Section 4.2, the estimated variables are worked by the filter in three different ways. Several parameters have been identified and classified according to how the filter performs its estimation. These are:

Correlated process noise are the variables which depend on their previous value. An exponential correlation factor with an auto-correlation time τ is used to model them. These are mainly used to model unknown parameters and noise:

- Solar radiation pressure's reference area.
- Non-gravitational accelerations on the spacecraft.
- Uncertain acceleration on Didymos barycentre.

Dynamic variables are those parameters which continuously vary in time, having a discrete value for each epoch, usually linked to a dynamic model.

- Spacecraft position and velocity.
- Didymos system's ephemeris around the Sun.
- Didymoon's ephemeris around Didymain.

Constants whose values do not vary and stay the same for the complete simulation.

- Gravitational parameter of the Didymos system and Didymoon.
- Didymoon's orbital elements.
- Non-spherical gravity - spherical harmonics.
- Landmark positions.
- Scale factor.
- Rotational state (Rotation axis and rotation rate).
- Sensor biases.

The auto-correlation time τ measures how much the modelled process noise depends on its previous state, in other words, it measures the characteristic time/periodicity/delay of a stochastic variable. Parameters such as the solar radiation pressure are highly unknown and this treatment allows to absorb that high uncertainty. Their assumed auto-correlation times will be selected by looking at their time-variation scales.

7.2.4. Filter tuning

Before any navigation analysis is carried out, a tuning of the filter parameters must be done both to adequate it to the modelled dynamics and to come up with what initial guesses make the filter converge. The filter has some configuration parameters that preset how the filtering process is going to be carried out. These are listed below

Batch-size represents the portion of batch-processing in the batch-sequential filter, as described in Subsection 6.2.3. It measures how many epochs are processed at the same time. A value equal to one transforms the filter into a purely sequential estimator. A value that minimises the navigation error was found. This value matches the frequency of range measurements, in other words, all Doppler and a single range measurement are processed at the same time. Thus, the solution for each of these arcs becomes more monotonous and the residuals are

Maximum number of iterations is the limit in successive iterations of a single batch until convergence is assumed. Low numbers such as two and three iterations have been observed to improve the solution without increasing too much the computation time. Thus, three is selected as the maximum number of iterations.

Relative step size for numerical differentiation is the spatial discretisation used for the computation of all partial derivatives. The lower the number the more precise the estimation of these derivatives is. However, a very small number can cause the derivatives to fall into the numeric precision of the computer, thus, yielding a null derivative. A scale factor of 10^{-5} was observed to be able to compute all partial derivatives without failing because of numerical precision.

All variables and parameters have a confidence level, which indicates to what precision the initial values are known. The nominal assumptions on these variables are listed in Table 7.3, which will be used as the starting navigation knowledge, unless otherwise stated. The remaining assumptions will depend on the particular character of each analysis. These values have been obtained by both reviewing the heritage of the AIM mission and probing the values. Some particularities were discovered, the filter does not converge if no uncertain acceleration is considered on the Didymos's barycentre and the uncertainty along one axis is one other larger than the remaining two.

7.2.5. Operational Schedule and Communication Links

Orbit determination and manoeuvre computation are carried out at ground control centres until more autonomy is given to deep space missions. As a low-cost mission, operations are to be carried during normal daytime working hours and the more expensive overtime work is to be avoided at all costs. In order to promote this low-cost philosophy, the different mission phases duration are designed to be a multiple of one day.

Values in Table 7.4[1] describe the characteristic times of operations that are relevant for ground-SC communications. At the distances at which Didymos will be from Earth during the ECP, the one-way light-travel (OWLT), the time it takes for light to travel from Didymos to Earth, is of the order of five minutes. Slew manoeuvres, to change pointing attitudes and thus, shifting from navigation to communications mode, or to point the RCS thrusters into an advantageous direction to perform a manoeuvre, are estimated to take five minutes. The download time for each image is also estimated to take five minutes. These values have no connection among them.

Cut-off communications time, understood as the time the SC and ground cannot establish communications, proves critical for the navigation. During the mission design, a maximum duration of 16 hours was set. This permits that in case of critical operations are needed, the schedule does not have to be changed, and between the last and next contact, ground can come with a command to send to the spacecraft. These 16 hours are dedicated to all SC operations but communications; being navigation and science among them.

[1] EN01 - AIM Mission Analysis Report 2017

Table 7.2: Dynamical parameters and assumptions used in the simulations

Parameter	Units	Value
Solar Radiation Pressure	[Pa]	4.65E-9
AU	[km]	149597870.7
S/C Reflection Coefficient	[-]	1.5
S/C Cross Section	[m^2]	5
S/C Mass	[kg]	400
Didymos System Mass	[kg]	5.278E11
Mass Ratio	[-]	0.0093
Sun's Gravitational Parameter	[km^3/s^2]	132712440041.9394
Didymain's Radius (Sphere)	[m]	780
Didymoon's Semi-Axes (Ellipsoid)	[m]	103 x 79 x 66
Sun's Radius (Sphere)	[km]	695990
Didymain's Rotation Period	[h]	2.26
Didymoon's Rotation Period	[h]	11.92
Didymoon's Orbital Period	[h]	11.92
Didymain's Orbital Elements (SMA, ECC, INC, RAAN, OMG, MEAN0, REF EPOCH J2000)	[-]	[1.18 km, 0, 0, 0, 0, 0, 0]
Didymain Pole Ecliptic Direction	[deg]	λ = 310 β = -84
Didymain's Harmonic Coefficients	[-]	Computed from body's polygonal shape
Didymoon's Harmonic Coefficients	[-]	Derived from ellipsoid shape

Table 7.3: Initial error assumptions for the navigation

Initial parameter-knowledge assumptions	Units	1-Sigma
Didymos-barycentre ephemeris position error	km	10
Didymos-barycentre ephemeris velocity error	m/s	0.1
Didymoon ephemeris position error	m	100
Didymoon ephemeris velocity error	m	0.001
Didymain gravity parameter error	%	10
Didymoon gravity parameter error	%	50/3
Didymain rotation axis angles error (uniform)	deg	3
Didymoon rotation axis angles error (uniform)	deg	1
Non-gravitational accelerations	m/s2	1x10-12
Didymos uncertainty acceleration	m/s2	[1 10 1]x10-7

Table 7.4: Operational schedule and communication links characteristic times

Operation	Time	Comments
OWLT	5 min	One Way Light Travel time between S/C and ground.
Slew Manoeuvre	5 min	Slew manoeuvre to change the S/C attitude.
Image D/L Time	5 min/image	Image download time from the S/C to ground.
Critical Operations Cut-off Time	16 h	Minimum time between data-cut off and a ground commanded manoeuvre execution by the S/C on Critical Operations.
Normal Operations Cut-off Time	48 h	Minimum time between data-cut off and a ground commanded manoeuvre execution by the S/C on Normal Operations.

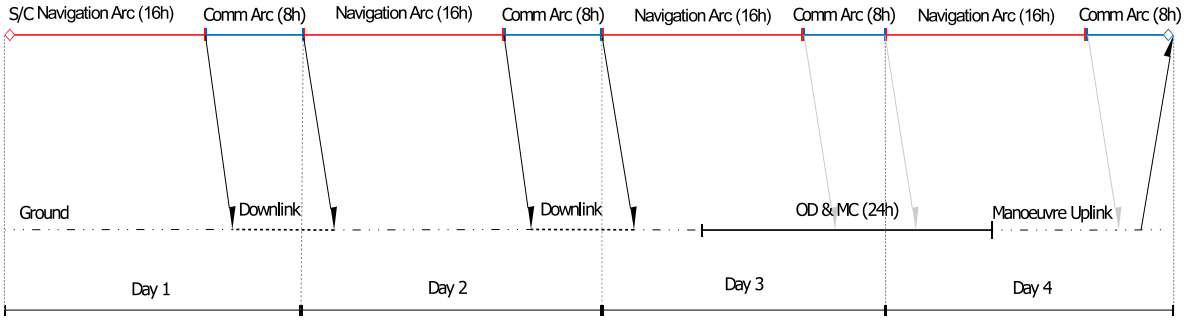

Figure 7.3: Operational schedule and communication links for a 4-day ECP arc

All information gathered during the navigation arcs must be downloaded to process the information at the ground-control centres. The remaining eight hours in a day are assigned to this task. Since only ground navigation is being assessed, a time between pictures of 1 hour is set. However, despite not being the topic of this work, for autonomous navigation, a higher frequency would be needed.

By using the aforementioned data and assumptions, a generic schedule of a hyperbolic arc can be made. In Figure 7.3 the schematic for the first ECP arc can be seen. The schematic is divided into two parts, one corresponding to the schedule for the SC on top, and below is the schedule for ground operations. The SC schedule is divided evenly between the navigation (red lines) and communication arcs (blue lines). Four groups of two of each, one for each Earth day, can be made. Ground establishes communications only during the communication arcs. These communications have a delay, caused by light travel time, plus, image and data download times are added to this delay to account for fluctuations on the operational turnaround times.

A manoeuvre must be computed before the end of the arc. Thus, the manoeuvre must have been uploaded to the SC before the end of the last communication arc, after which, the manoeuvre will be executed. During normal operations, ESA has established that the complete process of measurement processing, orbit determination, and manoeuvre computation takes 24h. This process is heavily optimised and follows a tight schedule. These 24 hours only correspond to the data processing at the ground-operation centres. The information must be first downloaded, transmitted, and then, prepared and scheduled for uplink. This uplink, due to the previously mentioned arc division, can only be finished after 48h after the last contact. Thus, the effective time between the last sent message and the execution of a manoeuvre is 48h.

This implies a huge constraint on the navigation and guidance, since a manoeuvre is computed using data at least 48h old. The data must be propagated to the manoeuvring point. For this propagation, no measurements are available, thus, the uncertainty on their value heavily increase with time. Once the manoeuvre has been carried out and data about these epochs are retrieved, the actual error can be computed.

7.3. Parameter estimation

In this section, the particularities of the parameter estimation process will be discussed. The main relations between the sources of information (measurements) and the parameters estimated from them will be outlined. When problems arise, ways to solve them will be sought and their rationale will be exposed.

The navigation for the considered analyses uses information from the following set of sensors:

- Optical Measurements
  - Centroiding (Didymain + Didymoon)
  - Landmarks
- Radiometric measurements
  - Range
  - Doppler
  - Delta DOR

First, as explained before, an indetermination problem appears when orbit determination is done only by the means of optical measurements and no range-measuring instruments are present. This problem is called the scale factor indetermination. The scale factor problem is a mathematical indetermination of the orbit determination (OD) caused by a poor observability. The observability is a property that relates how well a parameter can be estimated by one measure derived from it.

Second, the problem appears when only line-of-sight (LOS) measurements are available to estimate three-dimensional positions. These LOS measurements physically represent directions. Directions in 3D space are determined by two coordinates; often two angles are used for it. The remaining third coordinate would represent a point along that direction. Thus, the complete 3D state cannot be totally inferred from only LOS measurements.

Last, another particularity of the optical measurements will be discussed. Besides the scale factor indetermination, the other noteworthy difference between optical and radiometric measurements is whether they offer relative or absolute measurements. Optical measurements can only be processed to estimate the relative position of the spacecraft to the reference on which the measurements are taken. Whereas radiometric measurements provide information of both the spacecraft and the system that it is referenced to.

7.3.1. Scale-factor problem

Two types of line-of-sight (LOS) measurements are obtained by the camera sensor. These are, centroiding and landmarks, which come from quite different algorithms and their measuring mechanisms are completely unlike. Nevertheless, the mathematics behind both types of measurements is almost identical, since they both are LOS measurements. Thus, if applied directly, the solution to the equations that relate the position of the measured quantity to the measurement, $[p_i, p_j] = \mathrm{f}(r_x, r_y, r_z)$, is a set rather than a particular solution.

This can geometrically be observed in Figure 7.4, where it can be seen that the same shape distribution of tracked points at two different distances produces the same measurements, thus removing the uniqueness of the solution. The set of similar shapes are all solutions to this parameter estimation, thus an extra measurement is needed to solve for which solution of the set is the correct one, and to eliminate this indetermination.

As it was depicted before, the complete 3D state cannot be estimated only by the use of LOS measurements. Two angles cannot be used to compute a position in three dimensions. An extra measurement is needed to cope with this lack of information. This new measurement should carry information about distance.

The scale factor cannot be solved by taking successive measurements either. As observed in Figure 7.5, the problem remains unsolved for two consecutive measurements, when the dynamics are

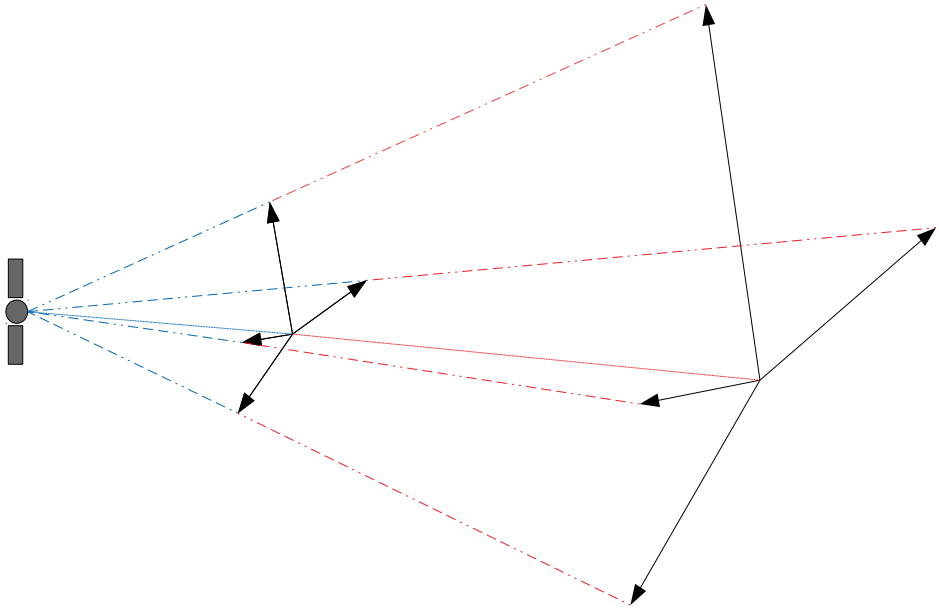

Figure 7.4: Scale indetermination for LOS measurements

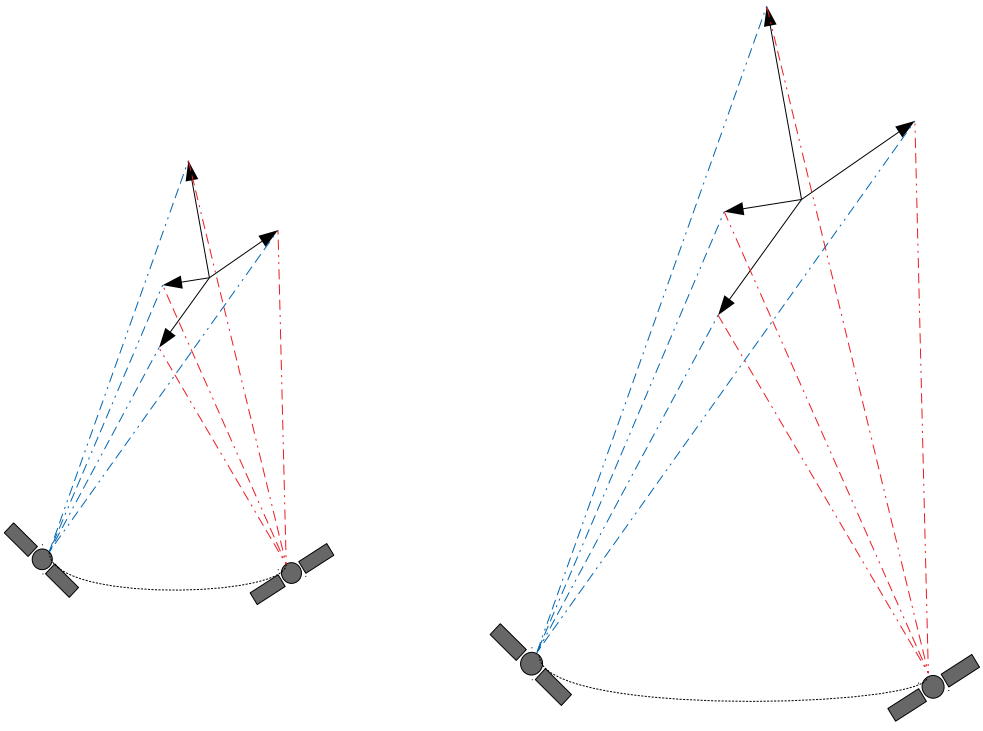

Figure 7.5: Scale-factor problem schematic for the orbit determination

unknown. Two measurements taken at two different positions scale to the same scale factor than before. These sets of measurements only solve the problem for the non-dimensional shape. This shape can be completely determined but lacking a quantity that defines the size of the complete set. However, once the dynamics are known, the size of the arc between the points is determined, and thus the scale of the system.

One possible information source could be an altimeter. An altimeter provides a slant range measurement. These slant ranges measure the distance from the spacecraft to the body's surface. Thus, the altimeter's measurement exactly provides the missing distance. Nevertheless, no altimeter is present in AIM, and other information sources must be searched for.

The only possible source of information are radiometric measurements: Range and Doppler. They provide range and LOS velocity measurements from a ground station. This information is used to reconstruct the orbit. Once the orbit is determined, the distance between two points at two epochs is known. Thus, as seen in Figure 7.5, once the distance between two consecutive measurements is known, the scale factor is determined.

Nevertheless, due to AIM's lack of a steerable HGA, radiometric and LOS measurements are mutually exclusive. This phenomenon takes place because AIM must be pointing to Earth to establish communications. If AIM's antenna points towards Earth, the asteroids would not fall in the FOV of the navigation camera, in general. Thus, both information sources are not present at the same time.

This leads to a big issue, the scale factor cannot be solved for until radiometric measurements are available. Moreover, when radiometric measurements are available, and the orbit is reconstructed, LOS measurements are not. Thus, strategies on how to solve this issue are to be probed.

Scale-factor modelling

Thus far, the scale-factor has been dealt with as if it were a physical parameter in the complete navigation problem. Nevertheless, the scale-factor is an abstract concept that shows up for LOS measurements, and has nothing to do with the dynamics. The actual modelling of these measurements impacts directly on how this factor is estimated. To properly model this phenomenon, the scale factor has to be taken off from the measurements; in this case landmark positions.

Landmarks are features on the asteroid's surface that are tracked for navigation purposes. These features rotate with the asteroid and are tracked along the SC's orbit. The position of the spacecraft can be extrapolated by tracking how these landmarks have moved in between successive pictures.

The model, followed for the navigation analyses, consists on the non-dimensionalisation of the asteroid's shape. A scalar factor is selected, and all distances in the asteroid model are non-dimensionalised. When the LM positions are expressed in Cartesian coordinates, thus, they are composed of three independent distances. Since each of these distances must be taken into account for the non-dimensionalisation, a spherical coordinates model is preferred. A change in the scale-factor induces changes in all three Cartesian coordinates of a LM, as seen in Equation (7.1), whereas only one of them is affected in spherical coordinates, see Equation (7.2).

$$\mathbf{LM}_{car_{pos}} = scale \cdot \begin{pmatrix} x \\ y \\ z \end{pmatrix} \tag{7.1}$$

$$\mathbf{LM}_{sph_{pos}} = \begin{pmatrix} scale \cdot r \\ \phi \\ \lambda \end{pmatrix} \tag{7.2}$$

Thus, the shape model, and subsequently all landmark positions, are described as a set of three spherical coordinates: a radius, a longitude, and a latitude. Then, all radii are non-dimensionalised, which decouples the size from the shape. This factor is chosen to be physically representative, thus the radius of the asteroid is selected. This way, all non-dimensional distances of the landmarks have unity characteristic order of magnitude.

Two approaches can be followed to further implement the effects of this scale indetermination. The first approach is to isolate the scale-factor with the measurements from which it came. In other

words, the scale factor only affects the estimated parameters of the measurements, in this case the landmarks position. No other variable in the estimation process is affected by it. This is the preferred approach, since one of the objectives of this work is to offer real navigation strategies, and this is the most representative method of actual orbit determination processes. This is the most representative solution since it is commonplace for actual ground navigation teams to decouple the orbit determination from the relative optical navigation, as explained by Godard et al. (2015), Takeishi et al. (2015), Delpech et al. (2015), and Miller et al. (2002).

The second approach tries to extend the physical influence of the factor to the complete system. All distances in the model are non-dimensionalised by this scale-factor, thus extending the shape-size separation to all estimated variables. This way, all size indetermination effects are extended to the SC position as well, giving closer physical relation to the root of the scale-factor problem. However, this method has not been used in asteroid navigation. For all former asteroid missions, the first approach has been used. Nevertheless, it offers an interesting approach to address the problem, and thus, it will be assessed.

7.3.2. Didymos ephemeris estimation

As stated in this section's introduction, optical measurements carry no information on the absolute position and velocity of the target they are referenced to. The only information they carry is the relative state between the measured object and the spacecraft. Thus, no camera measurements can be used to determine the ephemeris of the Didymos system. Only by means of the radiometric measurements position and velocity of Didymos can be estimated.

Nevertheless, the calculus of the absolute spacecraft position is not as precise as that obtained from the relative orbit determination. Since a displacement of Didymos's centre of mass produces the same effect as the individual displacement of the spacecraft, the problem is rank deficient. Thus, when solving for the spacecraft state with respect to the asteroid when the asteroid's ephemeris are known with poor precision, the estimates cannot be as accurate as those of the relative navigation.

Being a rank deficient problem, where there is no direct observation of Didymos's centre of mass, the estimation of the ephemeris of the asteroid system is foreseen to yield very high uncertainties, thus, a very poor accuracy when compared to the SC's position and velocity.

7.3.3. Didymoon mass estimation

One of the main constraints for the navigation is the estimation of Didymoon's mass. There is no direct measurement that is linked to the moon's gravitational parameter. Centroiding measurements which track the moon's movement along its orbit are not a helpful for the moon's mass estimation by themselves. The gravitational parameter, as stated by Grieger and Küppers (2017), can only be extrapolated from the oscillation the moon exerts on the spacecraft. This oscillation can be seen in Figure 7.6 in all three components of the velocity. The oscillation has an amplitude of 0.01 mm/s in velocity and 10 m in position.

The tiny gravitational pull of Didymoon makes it extremely difficult to estimate the moon's mass. Since this estimation relies on the previously mentioned effect, the accuracy of the navigation should yield estimates more precise than the amplitude of the oscillation. If the estimates are less accurate, the oscillation is absorbed by the global estimation noise and no information can be extracted. However, if the position estimate is precise enough and the position of the moon is known, the oscillation is translated into the moon's mass.

7.4. Strategy preselection

In this section, a first navigation strategy will be selected. All facts stated above will be used in the strategy selection. Further simplifications will be made and their rationale explained. The navigation analyses will be divided into two types. The first type, single-arc navigation, will consist on analysing a complete ECP arc, without taking into consideration manoeuvres and their effects. The second type is multiple-arc navigation, where manoeuvres are taken into account. Extra considerations are needed to properly simulate the impact of the manoeuvres on the navigation and guidance systems.

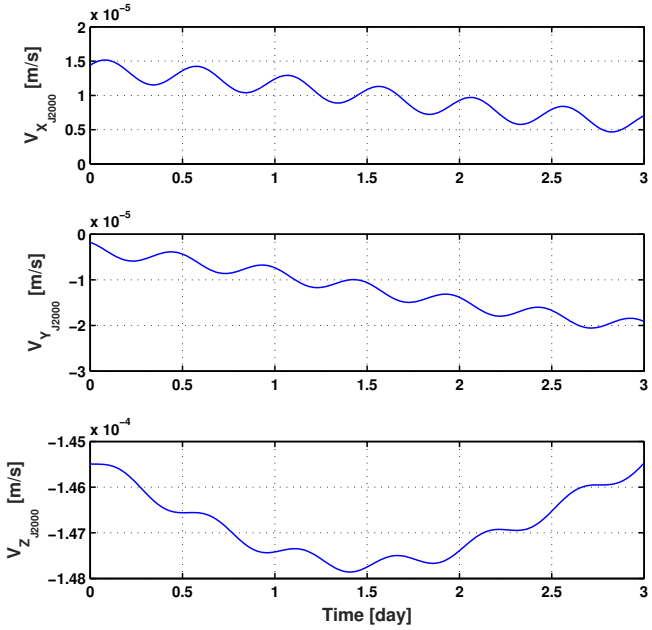

Figure 7.6: Oscillation effect on the SC Velocity caused by Didymoon

The single-arc navigation is the first step on which navigation strategies will be built. This division will help to optimise the parameter estimation process for the ECP. These analyses will consist on the orbit reconstruction of a single arc, without taking into account manoeuvre computation and its schedule. The SC trajectory is propagated, and measurements are computed by using this trajectory. These measurements are fed into the navigation filter, and the parameter estimation is carried out. Then, the results are later processed and plotted.

The first arc of the early-characterisation phase will be used for these analyses. This arc's duration is three days, which are further divided into two working modes, as explained in the previous sections. Each mode entails the use of either the navigation camera or the SC-Ground communications for the measurements. This is further schematised in Table 7.5.

Table 7.5: Schematic arc division of the first ECP hyperbolic arc

Mode	Navigation	Comm.	Navigation	Comm.	Navigation	Comm.
Measurements	NAC	Radiometric	NAC	Radiometric	NAC	Radiometric
Duration	16h	8h	16h	8h	16h	8h

Thus, optical and radiometric measurements are not present at the same epochs. The scale factor has to be solved for progressively, instead of directly. The parameter estimation is split. Some parameters with easy convergence are estimated first. Then, their resulting estimations are fed back, and the navigation is refined. Different kind of measurements are incorporated into the loop at different stages.

Thus, due to all these considerations, a first approach is outlined:

1. Centroiding measurements, of Didymain and Didymoon, are used to obtain a first estimate of the system and secondary's masses.
2. This first estimation on the masses is used as the starting point for the next simulation. Radiometric measurements are included, and the ephemeris of Didymos are calculated.
3. Once these last parameters have been estimated with their physical scale, landmark tracking is introduced in the loop.

Chapter 8
Results

In Chapter 7, the navigation problem to be addressed was reviewed, together with the most relevant issues that affect the navigation. These will prove key for the analyses to be performed and discussed in this chapter. Thus, the simulations that were carried out will be described, their results will be analysed and their conclusions discussed.

First, in Section 8.1, the navigation analyses will be limited to one hyperbolic arc. These analyses will be focused on searching for optimal ways to solve for the scale factor, without compromising the performance of the navigation.

Second, in Section 8.2, the analyses will be extended to the complete early-characterisation phase and its four arcs. Manoeuvres and the consequent thrusting errors they carry will be included, and their impact on the navigation will be assessed.

Third, in Section 8.3, once these analyses have been carried out, the variables that drive the navigation performance will be identified. This identification will lead to the quantification of their impact, for which sensitivity tests to some parameters will be performed. Most of these tests will provide information to construct navigation performance models. These are useful to quickly assess the overall output of the navigation.

Finally, this chapter will end in Section 8.4 all this information will subsequently allow for the proper shaping of navigation strategies, which are the objective of this MSc Thesis.

8.1. Single-arc Navigation Strategy

As stated in the previous chapter and in this section's introduction, the first set of analyses will consist on a single navigation arc. The parameter estimation process will be segmented into several stages. Some parameters will be estimated at the first stage.

The resulting estimation is used as the starting value for the next stage. More measurements will be added to the filtering process, further refining the estimates. This iterative process is intended to strengthen the robustness of the estimation process, and yield a more precise estimations.

Thus, the estimation process, properly justified in Section 7.4, has been divided into the following stages:

1. Navigation performance with centroiding
2. Navigation performance with radiometric measurements
3. Navigation performance with landmark matching

It is important to denote that during this stage, the analysed navigation performance will consist on the orbit reconstruction. In other words, the final knowledge on the SC trajectory when all measurements in one arc become available. Opposite to the reconstruction is the propagation. The propagation, depicted as the uncertainty on the future SC state, used to compute the manoeuvres beforehand, will be assessed only in Section 8.2.

8.1.1. Navigation Performance with Centroiding

This first step for the navigation analysis will only make use of centroiding measurements. The main objective of this stage is to achieve a reasonable estimation of both gravitational parameters. For this process to take place, a good estimation of the Didymoon's is needed.

As it was explained in the preceding Chapter 7, on Section 7.3, the mass of Didymoon is estimated by filtering the oscillation it exerts on the spacecraft. This oscillation strongly depends on the asteroid moon's distance to the spacecraft and has the same period as Didymoon's rotation around Didymain. Since the ECP was designed in such a way that both Didymain and Didymoon always fall in the FOV of the navigation camera, there are measurements on which the ephemeris can be constructed. This information source is the centroid-tracking data of Didymoon.

- Dynamical variables to be estimated:
  - Spacecraft position and velocity
  - Didymoon's ephemeris
- Dynamical parameters that are to be estimated:
  - Gravitational parameter of Didymos
  - Gravitational parameter of Didymoon
- Measurements which are incorporated into the filter:
  - Centroid-tracking of Didymain
  - Centroid-tracking of Didymoon

The initial guesses on the parameters's values and their level of confidence for this stage have already been listed on Table 7.2 and Table 7.3. An initial 1-sigma error on the initial guess of every variable has been considered.

The resulting SC trajectory is rotated into the orbital frame, since more physical conclusions can be inferred from the errors in each orbital frame than those in the Didymos J2000 RF. Since the effects on the navigation error are decoupled, this visualisation helps to understand the causality. This can be seen in Table 8.1, and as the navigation error evolution in Figure 8.2a. The error in the radial direction is observed to be one order of magnitude higher than the error in the remaining two axes.

This is caused by the character of the line-of-sight (LOS) measurements that are being used. Since Didymain's centroid is being tracked, and by definition it lies in the radial direction, no information is provided along this direction. However, it is still possible to solve for the SC position along the radius because the spacecraft rotates about Didymain. This rotation causes the radial axis to rotate as well. This way, the information gathered on the two perpendicular directions is transferred to the instantaneous radial axis. Thus, the quality on the cross and along-track axes is unachievable for the radial axis, mostly due to the lack of information on the LOS measurement.

This first estimation stage had the objective of obtaining a first estimate of the system's mass. An initial 10% 1-sigma on the system mass and a 16% 1-sigma were considered, as shown in Table 7.3. As it can be seen in Table 8.3 and in Figure 8.2c and Figure 8.2c, the filter achieves a precision of 0.7% and 6% for Didymos and Didymoon, respectively. However, these values are not accurate and a 5.6% and 11% deviation from the real solution is encountered. This occurs due to the scale factor indetermination. The system converges to a solution which is scaled w.r.t. the real trajectory. The same behaviour is observed in Table 8.1, where a very good knowledge is achieved with a very poor accuracy.

Table 8.1: Position estimation errors

	RMS [m]	1-sigma knowledge[m]
Along-track position	11.0	1.60
Cross-track position	9.82	1.18
Radial position	53.8	22.1

Table 8.2: Velocity estimation errors

	RMS [mm/s]	1-sigma knowledge[mm/s]
Along-track velocity	1.1	$2.09 \cdot 10^{-1}$
Cross-track velocity	1.0	$9.94 \cdot 10^{-2}$
Radial velocity	1.8	$1.55 \cdot 10^{-1}$

Table 8.3: Gravitational parameter estimation error

	RMS [%]	1-sigma knowledge [%]
Didymos μ	5.62	0.73
Didymoon μ	11.2	6.10

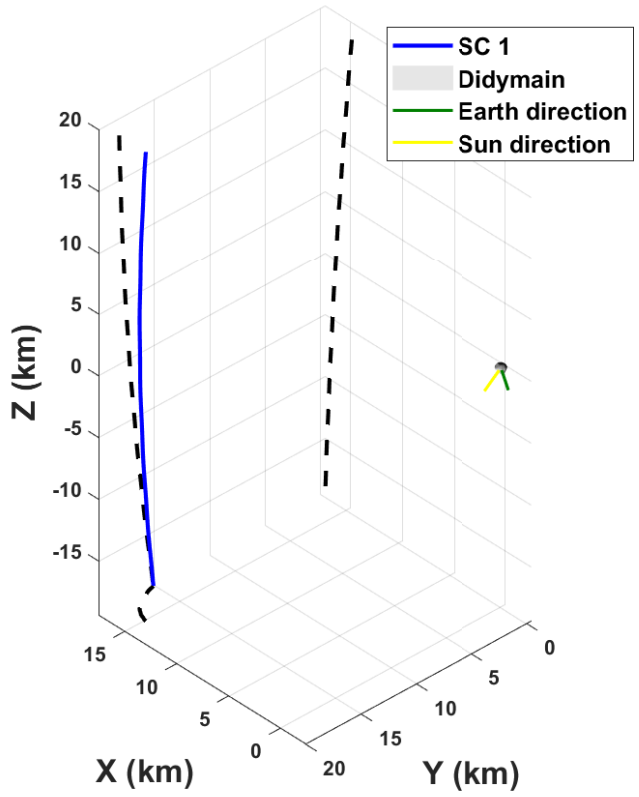

Figure 8.1: 3D ECP trajectory

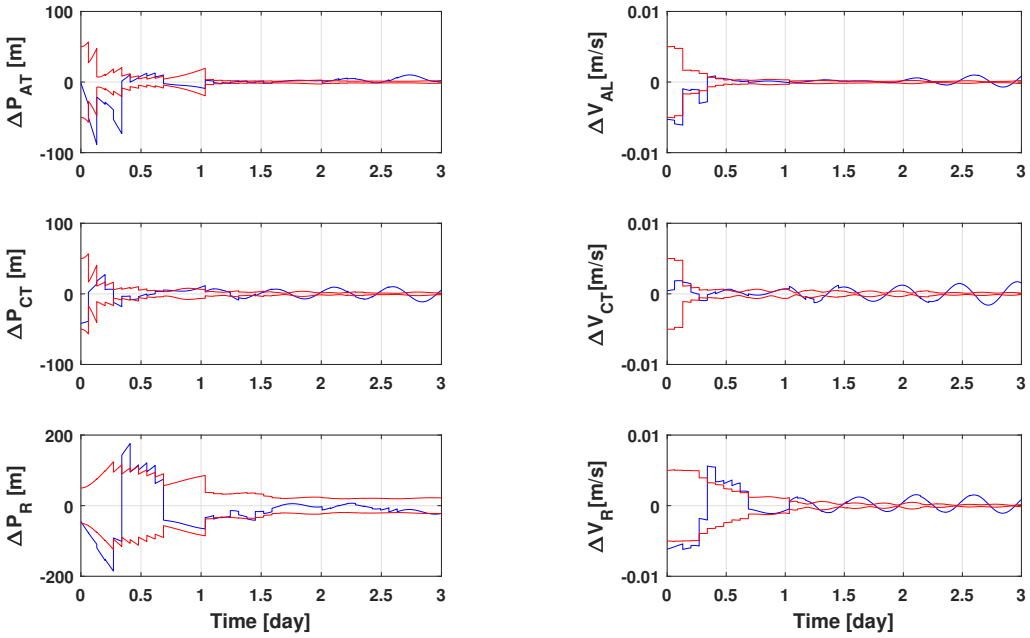

(a) SC Position

(b) SC Velocity

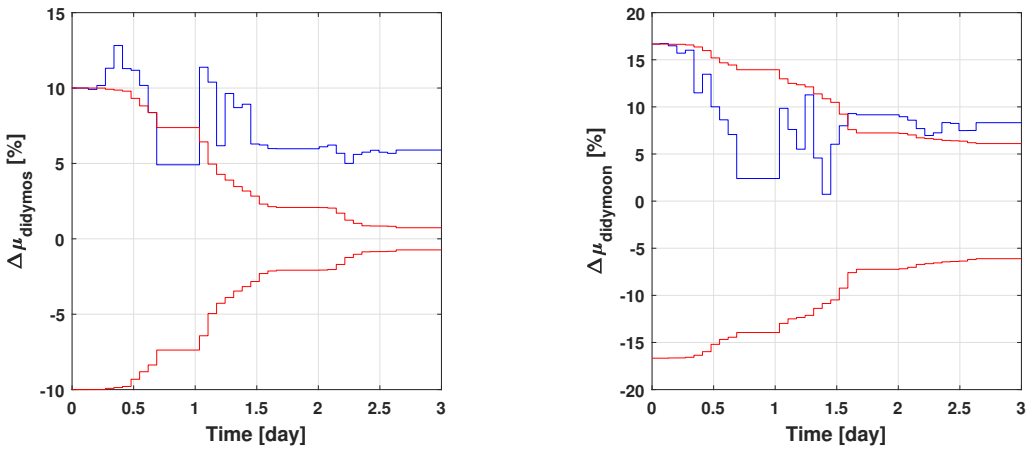

(c) Didymos's mu

(d) Didymoon's mu

Figure 8.2: Navigation error with centroiding measurements

8.1.2. Navigation Performance with Radiometric Measurements

Once a first estimate of the system's dynamics have been obtained, the next batch of measurements are incorporated to the navigation. These are the radiometric measurements: Range, Doppler, and DDOR. These contain information on the position of the Didymos system. Thus, the ephemeris of the system are to be estimated.

- Dynamical variables to be estimated:
  - Spacecraft position and velocity
  - Didymos system's ephemeris
  - Didymoon's ephemeris
- Dynamical parameters that are to be estimated:
  - Gravitational parameter of Didymos
  - Gravitational parameter of Didymoon
  - SRP Effective cross-sectional area
- Sensor parameters to be estimated:
  - Measurement biases
- Measurements which are incorporated into the filter:
  - Centroid-tracking of Didymain
  - Centroid-tracking of Didymoon
  - Range radiometric measurements
  - Doppler radiometric measurements
  - DDOR radiometric measurements

The availability of information on absolute distances, due to the radiometry, improves the estimation of both the SC state and the system mass. As it has been previously discussed, radiometry does not provide precise solutions when compared to the OD obtained from sensors that provide relative data. Here, relative is understood as referred to the central body, which, in this case, is Didymain.

The centroiding provides good solutions in all axes but the radial, along which these type of measurements provide no information. Thus, the overall performance of the navigation in the estimation of the SC state only improves along that axis, as seen in Table 8.4 and Table 8.5. The increased accuracy in the orbit determination allows to increase the knowledge on the secondary's mass as seen in Table 8.6, whose accuracy vs precision has been improved w.r.t. Table 8.3, thanks to the availability of information about the scale of the system.

The ephemeris of Didymos are estimated to an accuracy of 10 km in position and 10^{th}s of mm/s in velocity, as observed in Figure 8.3a and Figure 8.3b. In Figure 8.3c, the filtered empirical accelerations on the Didymos barycentre are shown. A bias in the Y axis is found. This axis corresponds to the direction of the Sun. This bias can be identified with the under-modelling of the dynamics of Didymos in the Solar System. The ephemeris are obtained using the Spice kernel while the considered dynamical model for Didymos consists on a simple central body gravitational attraction with a μ associated to it. Thus, the bias could be easily filtered out by modifying the considered μ_{Sun}. Nevertheless, third body perturbations would still be present.

During the considered epochs, there is visibility from only two of the three deep-space stations, Cebreros and New Norcia. A representation of the residuals of both Range and Doppler measurements is shown in Figure 8.4a and Figure 8.4b. Green dots/line represent the actual error carried by the measurement while light and dark blue represent the residuals of the computed measurements in the filter. The pink lines represent the assumed 1-sigma confidence level on the measurements, in other words, the weight of the measurements in the estimation. Lastly, the red line represents the 1-sigma level of confidence on the filtered residuals.

The range measurements, as explained in the assumptions, are modelled with a white noise and a bias on both the measurement and the position of the deep-space antenna. It can be noticed that the bias has been effectively filtered out in Figure 8.4a (green vs blue dots), since the real error on the measurements is biased while the computed residuals are not. Since Doppler measurements are not modelled with a bias, this behaviour does not appear in Figure 8.4b.

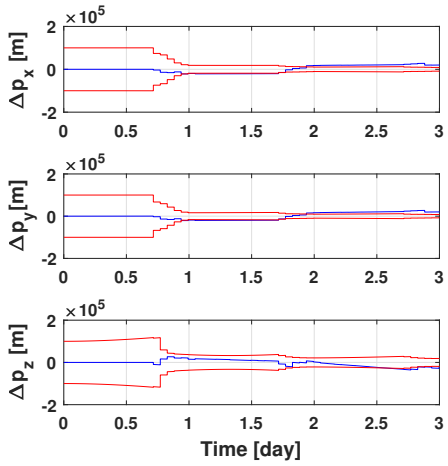

(a) Didymos Barycentre Position

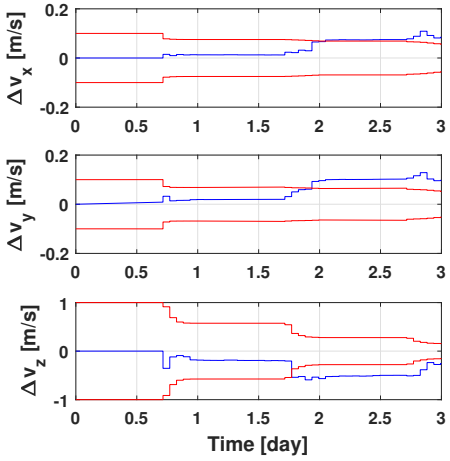

(b) Didymos Barycentre Velocity

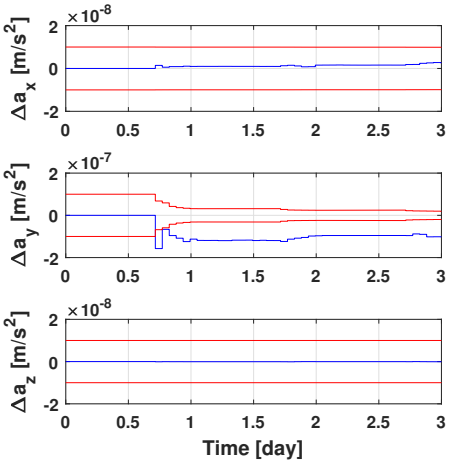

(c) Didymos's Empirical Accelerations

Figure 8.3: Navigation error with radiometry

Table 8.4: Position estimation errors

	RMS [m]	1-sigma knowledge [m]
Along-track position	2.08	0.54
Cross-track position	1.53	0.33
Radial position	8.70	4.54

8.1.3. Navigation Performance with Landmark Matching

The incorporation of the radiometric measurements has allowed to get an estimation on all variables related to the scale of the system, in other words, its size. This is present on the orbit determination and parameters such as the gravitational parameter of the system, all containing information on the distances. This allows to introduce landmark measurements on the filtering loop.

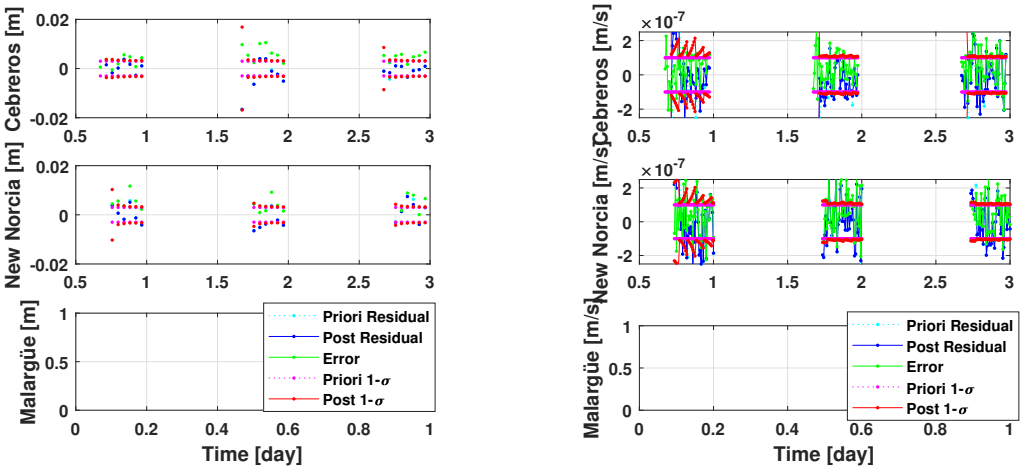

(a) Range Residuals

(b) Doppler Residuals

Figure 8.4: Radiometry Residuals

Table 8.5: Velocity estimation errors

	RMS [mm/s]	1-sigma knowledge [mm/s]
Along-track velocity	$1.00 \cdot 10^{-1}$	$2.09 \cdot 10^{-2}$
Cross-track velocity	$8.88 \cdot 10^{-2}$	$2.36 \cdot 10^{-2}$
Radial velocity	$1.65 \cdot 10^{-1}$	$1.69 \cdot 10^{-2}$

Table 8.6: Gravitational parameter estimation error

	RMS [%]	1-sigma knowledge [%]
Didymos	2.70	0.070
Didymoon	2.79	0.87

Table 8.7: Didymos Barycentre Position errors

	RMS [km]	1-sigma knowledge [km]
Along-track position	7.16	8.24
Cross-track position	6.83	7.48
Radial position	10.1	18.6

Table 8.8: Didymos Barycentre Velocity errors

	RMS [m/s]	1-sigma knowledge [m/s]
Along-track velocity	$5.09 \cdot 10^{-3}$	$5.59 \cdot 10^{-2}$
Cross-track velocity	$5.20 \cdot 10^{-3}$	$5.22 \cdot 10^{-2}$
Radial velocity	$4.95 \cdot 10^{-2}$	$1.54 \cdot 10^{-1}$

The simulated arcs, as per Section 7.2, always begin with a navigation arc, where optical measurements are taken. Whereas communication arcs, where the radiometry is carried out, only occur immediately after the latter. Thus, if the orbit determination were to be carried out following the reversed order, no information on the scale of the system would be available, making this last strategy ineffective. Only once the OD with radiometry has been carried out, and parameters which depend on distances have been estimated, the solution can be further refined with landmark navigation.

Landmarks provide a very precise source of information on which the orbit can be reconstructed. Since landmarks are fixed features on the tacked-body surface, they also provide a very trustworthy source of information regarding its rotational state.

- Dynamical variables to be estimated:
  - Spacecraft position and velocity
  - Empirical accelerations on the SC and Didymos
  - Didymos's ephemeris
  - Didymoon's ephemeris
- Dynamical parameters that are to be estimated:
  - Gravitational parameter of Didymos
  - Gravitational parameter of Didymoon
  - SRP Effective cross-sectional area
  - Landmark positions
  - Didymain's rotational rate and state

  Sensor parameters to be estimated:
  - Measurement biases
- Measurements which are incorporated into the filter:
  - Centroid-tracking of Didymain
  - Centroid-tracking of Didymoon
  - Landmark-matching of Didymain
  - Range radiometric measurements
  - Doppler radiometric measurements
  - DDOR radiometric measurements

In Figure 8.5, two snapshots of Didymain at two consecutive simulation times are shown. A set of 20 landmarks on the surface of Didymain have been used, and they are displayed on their respective locations on the asteroid's surface. Those which are recognised by the camera are shown in green while those in red are in view but not recognised. It is important to notice that, in between these two snapshots, the asteroid has slightly rotated. This can be easily inferred from the position change in the tracked landmarks. Some of them are no longer visible while others have appeared. There are also some that were recognised by the camera that no longer meet the visibility conditions and vice-versa. The observed rotation of Didymain is clockwise due to the high declination of its rotation axis.

The OD solution is seen to be improved in all axes, as seen in Table 8.9 for the position and in Table 8.10 for the velocity. As explained before, the radiometry does not provide the sufficient accuracy to improve the solution, but Landmarks do. Since landmarks are being measured almost entirely along the radial direction, the angular resolution is poor and the performance along this axis is too.

The scale factor indetermination plays a role on this as well. This difference is quite noticeable when the navigation performance of the navigation arcs is compared to the communication arcs. The solution is quite stable during the navigation arcs, with a 1-sigma accuracy in the sub-metre level in position. Once landmark measurements cease to be available and only radiometry is used, the solution quickly worsens to tenths of metres. However, despite this quality deterioration of the orbit solution and due to the scale factor indetermination, it is during these arcs that the solution keeps its stability and allows the improvement in the parameter determination.

Thanks to the increased knowledge in the SC state, the estimation of Didymoon's mass is refined to 2% 3-sigma while a 0.2% 3-sigma is achieved for the mass of Didymos. Regarding the scale factor, which can now be extrapolated thanks to the landmarks reference, it has been observed that

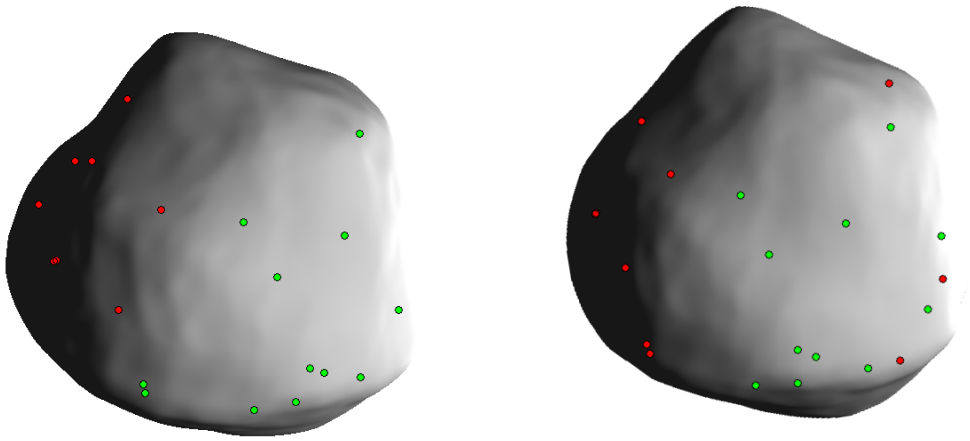

(a) Snapshot 1 (b) Snapshot 2

Figure 8.5: Landmarks on Didymain at two consecutive instants

the solution quickly converges for small initial errors in the scale, as seen in the top of Figure 8.6. High errors, 15% in magnitude and higher, lead the orbit determination to unstable regions where no convergence is achieved. However, actual causalities seem to be quite complex. Thus, it is only safe to extrapolate that the orbit determination solution is still too sensible to the scale factor and only small deviations are easily dumped out. Fine parameter-tuning seems to be of key importance for the convergence of the navigation with landmarks.

The rotational state of Didymain is very easily estimated, to a very precise knowledge, as seen in the bottom plot of Figure 8.6. This accuracy is due to the amount of information that the landmarks carry about the rotational state. Small modifications in the rotational rate of Didymain would produce large displacements of the observations. The same phenomenon occurs for the orientation of the rotation axis. Thus, these parameters converge easily and their knowledge is improved to a 3-sigma accuracy of 0.03 deg for the declination and a 0.20 deg 3-sigma for the right ascension of the rotation axis. On the other hand, these parameters are isolated from the scale factor, they are not affected by its indetermination since are size-less quantities that only depend on angles and angular rates. Thus, its determination benefits entirely from the dense information pool landmarks are, without incurring in any of their disadvantages.

As observed in Figure 8.7, the behaviour of the three different landmark-position coordinates varies widely. The radial distance is linked to the scale factor and behaves analogously. The latitude of the landmarks is very easily determined and shows a stable behaviour. Having a well determined rotational state, guarantees very precise knowledge on the latitude of the landmarks, since they only move in a plane perpendicular to the rotation axis, defined by their latitude. However, this effect is not seen in the longitude.

Its bad determination behaviour has been linked to two separate factors. The first factor being the uncertainty on the displacement between the actual centre of mass and the geometrical centre. The geometrical centre is used as the reference from which the landmark observables are computed. This displacement is seen to be in the order of metres, as observed in Table 8.12. The second factor is the knowledge on the measurements. Landmarks have long been proven to be tracked with sub-pixel accuracy. One pixel, at the working distances, translates into a resolution of a couple of meters.

Since the uncertainty on the landmark position is equal to that of the centre of mass displacement, its solution cannot be further improved. This joined with the uncertainty on the SC position, yields an error in the order of degrees for the landmark longitude.

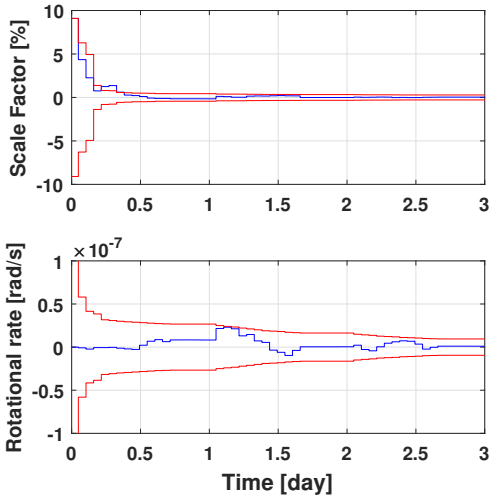

Figure 8.6: Scale Factor and Angular Velocity Navigation Error

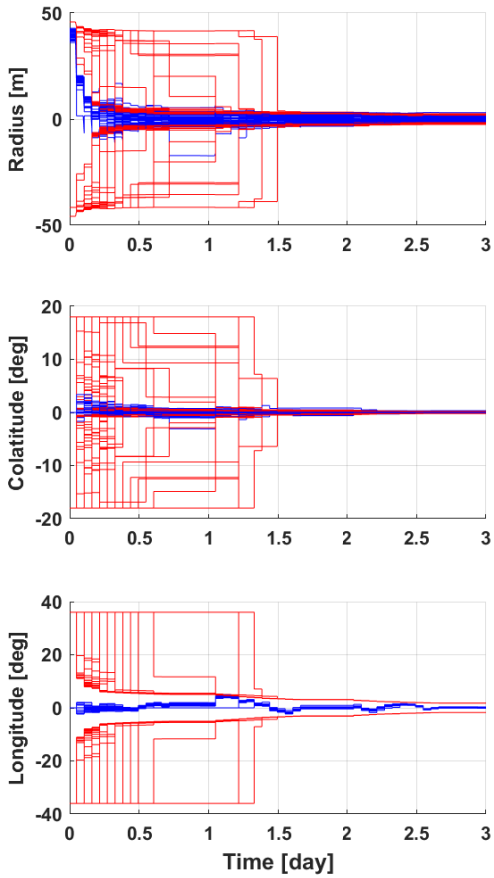

Figure 8.7: Landmark Position Navigation Error

Table 8.9: Position estimation errors

	RMS [m]	1-sigma knowledge [m]
Along-track position	1.11	0.57
Cross-track position	1.08	0.73
Radial position	5.03	4.05

Table 8.10: Velocity estimation errors

	RMS [mm/s]	1-sigma knowledge [mm/s]
Along-track velocity	$4.00 \cdot 10^{-2}$	$1.74 \cdot 10^{-2}$
Cross-track velocity	$4.91 \cdot 10^{-2}$	$1.88 \cdot 10^{-2}$
Radial velocity	$7.63 \cdot 10^{-2}$	$1.68 \cdot 10^{-2}$

Table 8.11: Gravitational parameter estimation error

	RMS [%]	1-sigma knowledge [%]
Didymos μ	0.069	0.042
Didymoon μ	0.72	0.52

Table 8.12: Centre of Gravity Offset Navigation Error

	RMS [m]	1-sigma knowledge [m]
$X_{Didymain}$	0.98	0.97
$Y_{Didymain}$	0.98	0.97
$Z_{Didymain}$	0.99	0.98

8.2. Multi-arc Navigation Strategy

The early-characterisation phase is divided into four hyperbolic arcs, which are connected at the manoeuvring points. These manoeuvres are calculated beforehand with the data sent by AIM to ground, and sent back to the spacecraft for their execution.

This causes issues such as the fact that the manoeuvres have been calculated with days-old data, as explained in Subsection 7.2.5. Thus, their accuracy is compromised and it must be assessed to know how to cope with these constraints.

The antiquity on the manoeuvre calculation data is not the only issue that the navigation must cope with. Manoeuvres are not executed perfectly, actuation errors are always present, causing a considerable impact on both the navigation and guidance. In terms of navigation, these actuation errors can worsen the quality of the estimates by introducing deviations that need to be estimated.

These new estimations can cause an already converged-solution to diverge, thus, effective ways to absorb that uncertainty are needed. And finally, in terms of guidance the error propagate through the entire arc and can only be corrected at the next manoeuvring point. This correction manoeuvre will also carry errors in its execution, thus, an analysis on its performance is necessary.

8.2.1. Navigation Performance without Actuation Errors

The first of the multi-arc analyses is performed without manoeuvre execution errors. Data is gathered and processed as explained in Subsection 7.2.5. For the first manoeuvre, data of only one third of the complete arc is used, with a 2-days old antiquity. Then, the manoeuvre is performed. The same schematic is followed for all four arcs. The executed thrust is measured by the IMU, becoming an input for the navigation.

As observed in Table 8.13 and Table 8.14, the final knowledge on the orbit determination improves in all three axes, but specially along the radial direction. This could be explained by the fact that not all landmarks are observable from all ECP arcs. Thus, during the progression of the ECP, more landmarks are being identified and incorporated into the navigation, further increasing the amount of information available to reconstruct the orbit. This occurs up to a level where a the maximum accuracy is achieved. This evolution can be observed both in Figure 8.8 and Figure 8.9. In both these figures, the dispersion, the knowledge on the deviation from the reference position, is plotted against the knowledge on the actual position. As it can be observed, for the position the dispersion always increases up to 100 metres at the end of the four ECP arcs. However, the dispersion on the velocity is bound and does not increase with time.

Table 8.13: Position estimation errors

	RMS [m]	1-sigma knowledge [m]
Along-track position	0.49	0.85
Cross-track position	0.82	0.87
Radial position	1.14	1.27

Table 8.14: Velocity estimation errors

	RMS [mm/s]	1-sigma knowledge [mm/s]
Along-track velocity	$2.89 \cdot 10^{-2}$	$3.76 \cdot 10^{-2}$
Cross-track velocity	$6.70 \cdot 10^{-2}$	$3.68 \cdot 10^{-2}$
Radial velocity	$5.22 \cdot 10^{-2}$	$5.63 \cdot 10^{-2}$

8.2.2. Manoeuvre Impact on Navigation Performance

Manoeuvres always carry execution errors that worsen the intended corrective effect they were calculated for. The error model, described in Subsection 4.3.3, has been used with listed assumptions on Table 2.2, a 3% error in magnitude and 1° in direction. The same scenario and assumptions have been used for the current analysis.

As it can be expected, the solution worsens in both navigation and guidance. This can be observed both in Table 8.15 and Table 8.16, where the final uncertainty on all three axis for both position and velocity is greater than in the preceding case. This deterioration is also seen in the dispersion. In Figure 8.10 the dispersion the manoeuvre errors cause the dispersion to grow far beyond the previous values, reaching to one kilometre uncertainty. Nevertheless, the biggest effect is observed in Figure 8.11, where the before-stable velocity dispersion, increases for each executed manoeuvre.

Table 8.15: Position estimation errors

	RMS [m]	1-sigma knowledge[m]
Along-track position	0.52	1.08
Cross-track position	0.90	1.28
Radial position	1.50	1.55

Table 8.16: Velocity estimation errors

	RMS [mm/s]	1-sigma knowledge[mm/s]
Along-track velocity	$2.96 \cdot 10^{-2}$	$4.55 \cdot 10^{-2}$
Cross-track velocity	$6.91 \cdot 10^{-2}$	$6.52 \cdot 10^{-2}$
Radial velocity	$5.34 \cdot 10^{-2}$	$4.32 \cdot 10^{-2}$

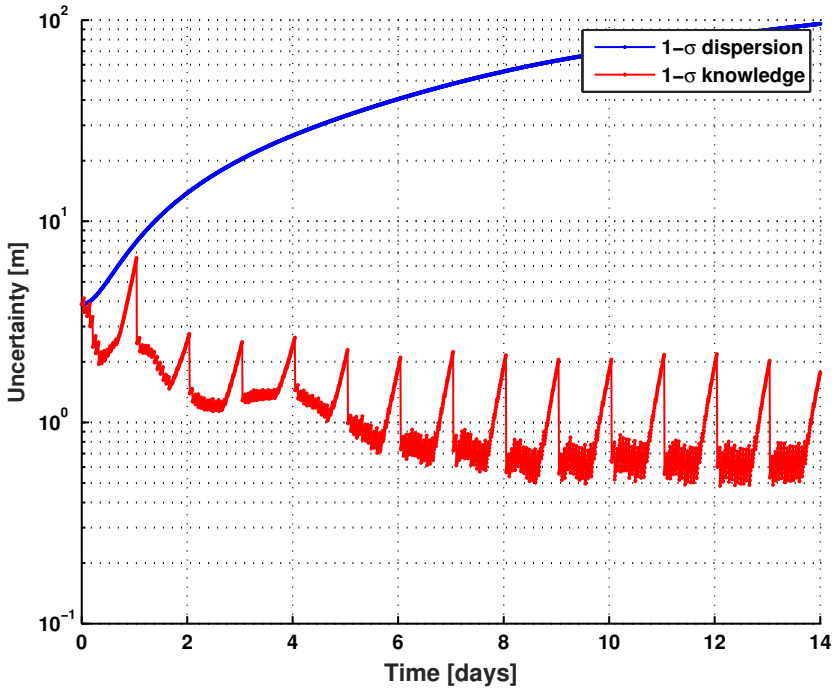

Figure 8.8: Dispersion and knowledge position evolution without manoeuvre errors

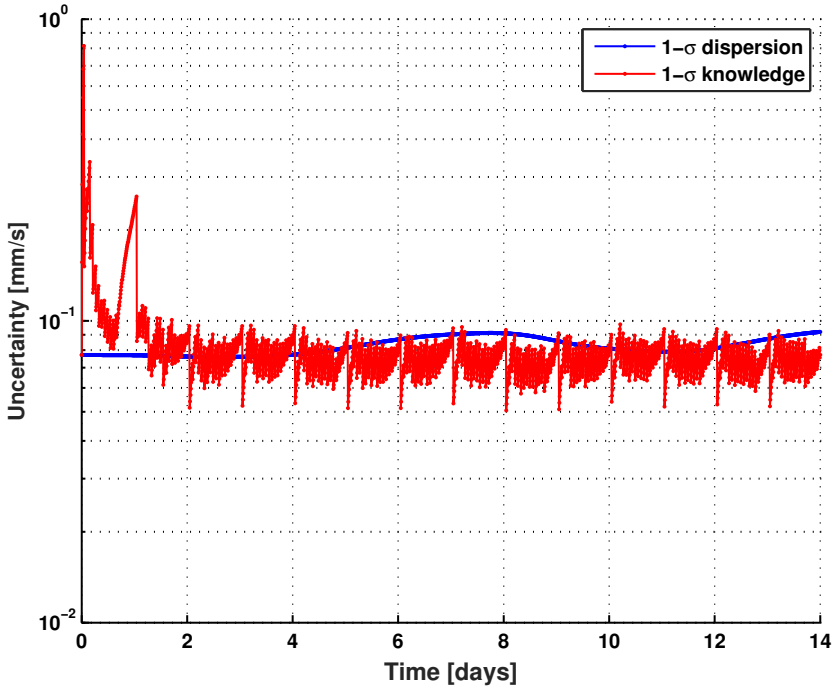

Figure 8.9: Dispersion and knowledge velocity evolution without manoeuvre errors

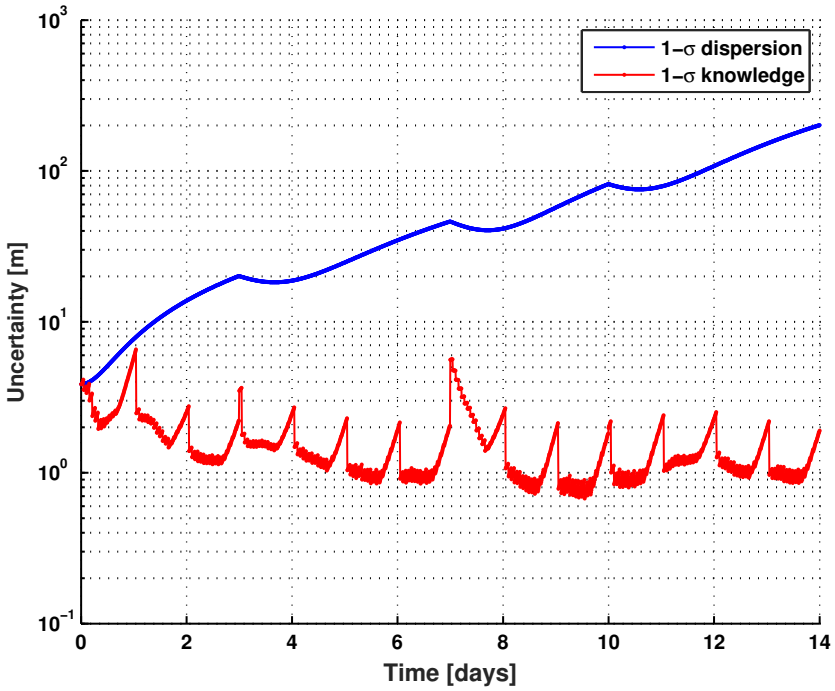

Figure 8.10: Dispersion and knowledge position evolution with manoeuvre errors

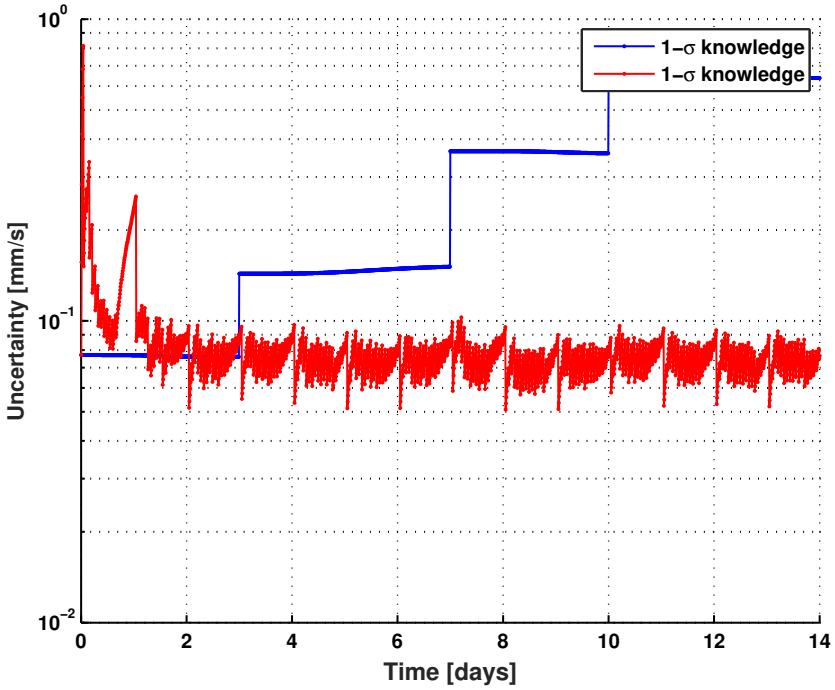

Figure 8.11: Dispersion and knowledge velocity evolution with manoeuvre errors

8.3. Sensitivity to ECP parameters

Once analysed all the nominal ECP cases, several parameters have been identified to be linked to the performance of the navigation. Sensitivity analyses were carried out to assess how strong their influence on the navigation performance is, and to characterise their dependencies. The results and considerations are exposed and discussed in this section.

8.3.1. Orientation of the Didymos System

For the analysed epochs during the ECP, both Earth and the Sun's positions w.r.t. the Didymos system vary very slightly. However, their relative orientation influences the quality of the radiometry and camera measurements. Thus, the most relevant parameters linked to their orientations are analysed: Earth's position on Doppler measurements and phase angle.

Earth Orientation - Doppler

The orientation of the Earth with respect to the asteroid system mainly influences the quality of the radiometry. Doppler measurements provide only information on the projection of the velocity along the LOS. The components of the velocity in the perpendicular plane are not measured. Thus, due to the quasi-planar trajectory of AIM during the ECP, a plane that contains AIM's trajectory can be defined. If Earth were to be located in a direction perpendicular to that plane most of AIM's velocity would be contained in the plane. Its projection along the Earth direction would be small enough for the noise to significantly worsen the quality of the Doppler measurements, leading to an ineffective filtering and poor results. However, this would only occur when the projection of the relative velocity between Didymos and the Earth along that direction is almost zero.

The SC trajectory has been reconstructed with only Doppler measurements. Two Earth orientations have been used to assess this phenomenon, as observed in Figure 8.12. There, the orientation perpendicular to the ECP plane is denoted as A in black, and another perpendicular to the latter is denoted as B in blue. These two orientations would have a different impact depending on the analysed arc. Thus, two different ECP arcs, one vertical (V) and one horizontal (H) arc have been analysed giving a total number of four cases, whose results are listed in Table 8.17. Of all four cases, three are unfavourable, since Earth is perpendicular to the arc during all its length. The only case where an improvement is observed is the horizontal arc with the B orientation. Here, the improvement is seen in both velocity and position.

Thus, a clear correlation between the orientation of an individual hyperbolic arc and the Earth is observed. Nevertheless, for an arbitrary orientation of the system, this phenomenon is cancelled. Only the worst oriented cases are observed to worsen the navigation solution.

Table 8.17: Navigation position and velocity performance for different orientations of the Didymos system with only Doppler measurements

		AV	BV	AH	BH
Along-track Position	RMS [m]	47.7	25.7	25.7	11.5
Cross-track Position	RMS [m]	115.2	159.2	159.2	14.2
Radial Position	RMS [m]	82.3	86.3	86.3	23.7
Along-track Velocity	RMS [mm/s]	0.55	0.32	0.32	0.28
Cross-track Velocity	RMS [mm/s]	1.6	2.1	2.1	0.21
Radial Velocity	RMS [mm/s]	1.2	1.1	1.1	0.35

Sun Orientation - Phase Angle

The phase angle, defined as the angle between nadir and the Sun direction, is one of the most important parameters for optical navigation. The illumination and observation conditions of the asteroid can be extrapolated by looking at its value. Five starting positions for a single vertical arc have been tested. The initial longitude of the arc has been modified in a 180° interval, centred on the nominal value. Longitudes close to 0°, imply a vertical passage in between the Sun and the asteroid. Longitudes close to -90° or 90° imply vertical passages where only half illuminated asteroid is been observed.

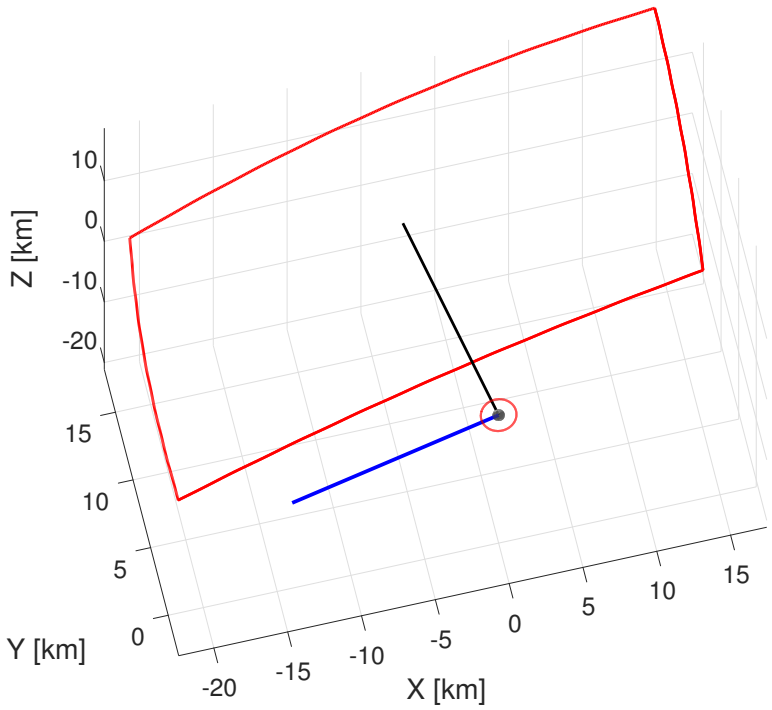

Figure 8.12: Earth directions used to assess the impact of the Doppler measurements - (A) Black - (B) Blue

Among the results, shown in Table 8.18 and Table 8.19, two main considerations can be made. Very high phase angles worsen the navigation performance in a significant manner. The illuminated portion seen by the SC is very small. Thus, very few landmarks can be identified and only for short periods of time. The same effect seems to take place for very small phase angles, where the current model for landmark matching also reduces its performance. This is due to the lack of shadows that delineate the features on the asteroid's surface, thus, failing to recognise the tracked landmarks. Nevertheless, this only occurs for a small arc of the complete trajectory, thus its importance is not as critical as that of a very high phase angle.

Table 8.18: Navigation performance for different starting positions with different phase angles (I)

Initial longitude	[deg]	-135	-90	-45	0
Phase angle	[deg]	127.16	94.82	60.39	37.67
Along-track Position	RMS [m]	1.14	0.92	0.91	1.02
Cross-track Position	RMS [m]	1.50	1.86	1.59	1.81
Radial Position	RMS [m]	3.01	1.92	1.94	2.61
Along-track Velocity	RMS [mm/s]	$6.6 \cdot 10^{-2}$	$4.0 \cdot 10^{-2}$	$5.2 \cdot 10^{-2}$	$4.7 \cdot 10^{-2}$
Cross-track Velocity	RMS [mm/s]	$1.2 \cdot 10^{-1}$	$1.4 \cdot 10^{-1}$	$1.2 \cdot 10^{-1}$	$1.5 \cdot 10^{-1}$
Radial Velocity	RMS [mm/s]	$1.3 \cdot 10^{-1}$	$5.7 \cdot 10^{-2}$	$7.8 \cdot 10^{-2}$	$9.8 \cdot 10^{-2}$

8.3.2. Distance to the Asteroid

The SC distance to the asteroid has been identified as one of the parameters leading the navigation performance. Five cases have been considered, in which the initial distance to the asteroid has been modified. The initial velocity has also been modified so the escape velocity is conserved.

Table 8.19: Navigation performance for different starting positions with different phase angles (II)

Initial longitude	[deg]	45	90	135	180
Phase angle	[deg]	50.63	83.44	117.63	139.58
Along-track Position	RMS [m]	0.79	0.90	0.93	1.68
Cross-track Position	RMS [m]	1.58	1.86	1.70	1.22
Radial Position	RMS [m]	1.70	1.93	2.18	7.32
Along-track Velocity	RMS [mm/s]	$3.9 \cdot 10^{-2}$	$3.6 \cdot 10^{-2}$	$5.5 \cdot 10^{-2}$	$1.1 \cdot 10^{-1}$
Cross-track Velocity	RMS [mm/s]	$1.3 \cdot 10^{-1}$	$1.4 \cdot 10^{-1}$	$1.3 \cdot 10^{-1}$	$8.6 \cdot 10^{-2}$
Radial Velocity	RMS [mm/s]	$5.3 \cdot 10^{-2}$	$5.7 \cdot 10^{-2}$	$8.2 \cdot 10^{-2}$	$2.7 \cdot 10^{-1}$

A clear correlation between the distance and the orbit determination precision is found. Since the precision of the radiometry does not depend on the SC-asteroid distance, the sole contributor to the navigation error are the optical measurements. Nevertheless, the highly uncertain dynamics around Didymos counterweight the increased performance of the optical navigation. The further the SC is from the asteroid, the smaller the impact of high degree gravitational terms is. However, the increased accuracy of the camera measurements eclipses the increasing uncertainty in the dynamics.

The closer the SC becomes to the asteroid, the better the angular resolution of each pixel is. One pixel has a resolution of a couple of meters at the nominal distance of 30 km. At the working distances, the behaviour of the pixel resolution is almost linear, doubling if the distance is doubled. However this is not the sole contributing factor to the observed improvement. The closer the SC is to the asteroid, the greater the angular resolution among the different landmarks is. This translates into a reduced uncertainty along the radial axis, for which more information is available from each tracked landmark, as observed in Table 8.20. Regarding the remaining two axes only an improvement in the cross-track direction is observed.

In terms of velocity, the observed effect is not as strong as that seen on the position. However, the same behaviour is seen for all three axes. The accuracy on the cross-track and radial velocity is improved when the distance to the asteroid is reduced, while no improvement is observed for the along-track velocity.

Table 8.20: Navigation position performance for different 3-day arcs at 5 different distances

Case	Along-track RMS [m]	Cross-track RMS [m]	Radial RMS [m]	Position RMS [m]
$\frac{1}{2}r_0$	1.6	2.0	2.7	3.7
$\frac{\sqrt{2}}{2}r_0$	1.4	2.2	3.1	4.1
r_0	1.3	2.4	3.7	4.7
$\sqrt{2}r_0$	1.3	3.0	5.3	6.2
$2r_0$	1.5	3.4	7.3	8.3

Table 8.21: Navigation velocity performance for different 3-day arcs at 5 different distances

Case	Along-track RMS [mm/s]	Cross-track RMS [mm/s]	Radial RMS [mm/s]	Velocity RMS [m]
$\frac{1}{2}r_0$	0.098	0.15	0.11	0.21
$\frac{\sqrt{2}}{2}r_0$	0.087	0.17	0.13	0.23
r_0	0.076	0.19	0.15	0.25
$\sqrt{2}r_0$	0.074	0.21	0.16	0.28
$2r_0$	0.085	0.22	0.17	0.30

8.3.3. Initial Navigation Error

An assessment on how the impact of the initial navigation error on the navigation performance has been carried out. This initial velocity error accumulates and deteriorates the estimation of the position, thus worsening the parameter estimation process.

This effect can be seen directly in Figure 8.13a and Figure 8.13b, where several initial errors in velocity have been propagated through a single ECP arc and plotted against the resulting RMS of the orbit determination solution. The resulting navigation performance behaves almost linearly in velocity for all three axes. However, in terms of position, the effect in the radial axis stands out.

The accuracy along the radius is heavily affected by the initial velocity error. This effect is due to the availability of sensor information along the radial direction, causing the greatest impact among all axes. Thus, it can be concluded that the initial knowledge on the position is key for the accuracy of the orbit determination, since there is a strong correlation between the initial and root-mean-square error residuals.

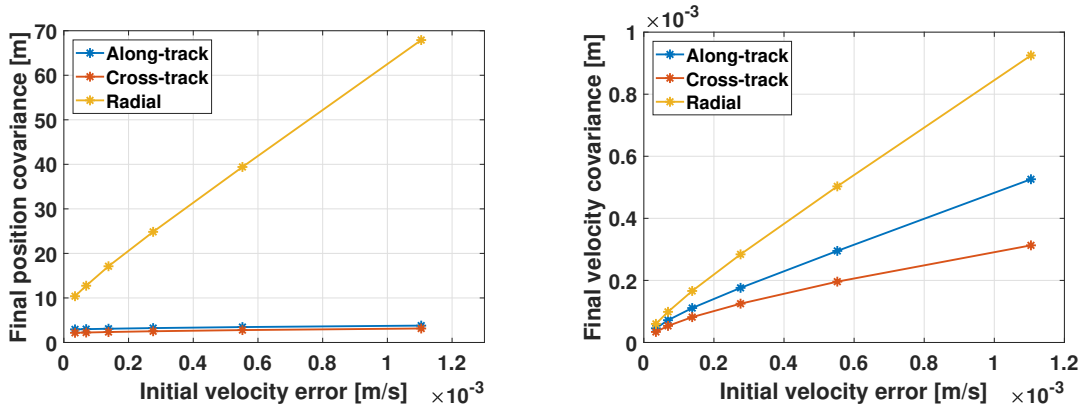

(a) Position (b) Velocity

Figure 8.13: Impact of initial velocity navigation errors on navigation performance

8.4. Monte-carlo Analysis

The complete orbit determination and parameter estimation process is a stochastic process, on which many random variables are intervening. Their complex connections and inter-dependencies make the whole process impossible to characterise analytically. To successfully characterise the behaviour of the complete ECP, a Monte-Carlo (MC) campaign has been carried out. This campaign uses the best results from previous sections as its starting point. Thirty five MC runs were carried out, and their results are shown below.

In Figure 8.10, for position, and Figure 8.11, for the velocity, the final knowledge on the parameters (red) is plotted against the final error in each of the MC runs (blue). Some simulations are seen to yield an error several times higher than that of the confidence level in the filter. Nevertheless, in the great majority of runs, the error approximates very well the 1-sigma knowledge of the filter. These show the final confidence level of the navigation, a 3-sigma 5.5 metres in position and 3-sigma 1.2 millimetres per second for the velocity.

In Figure 8.16, the final results for the estimation of the secondary's mass are shown. The final knowledge on the asteroid's mass by the filter (red) is plotted against the RMS of the estimate in each of the MC runs (blue). The RMS of the estimation in each of the simulations approximate very well the knowledge the filter had in each run. The same high deviations observed for the velocity and position also show up for the mass estimation. This is caused by the high correlation, as explained in Section 7.3, between the maximum accuracy in the SC state and the accuracy limit in the asteroid's mass estimation. It is also observed that the expectancy for the RMS (blue line) approximates very well the supposed accuracy inferred by the filter.

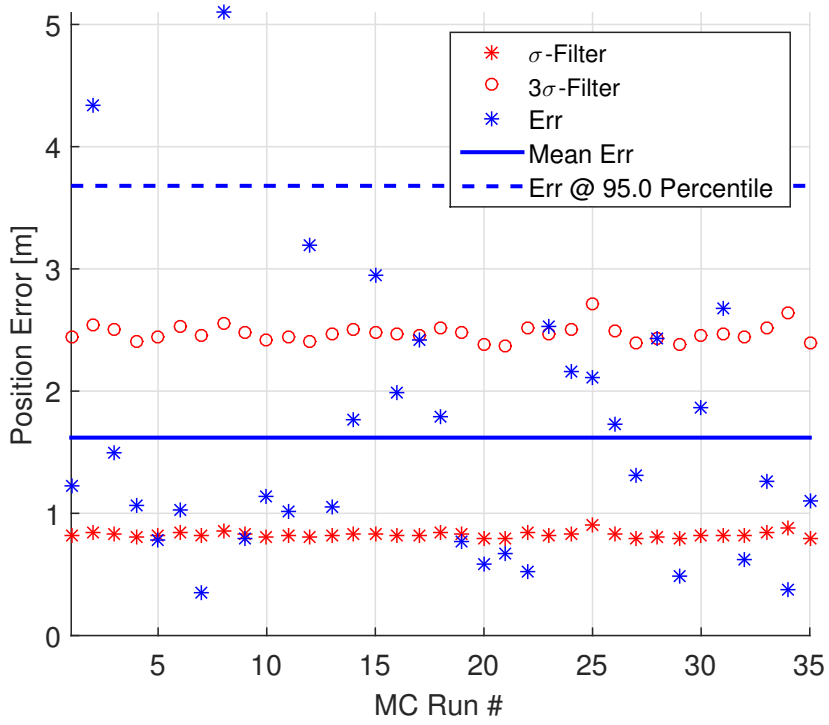

Figure 8.14: Final Monte-carlo results for the position

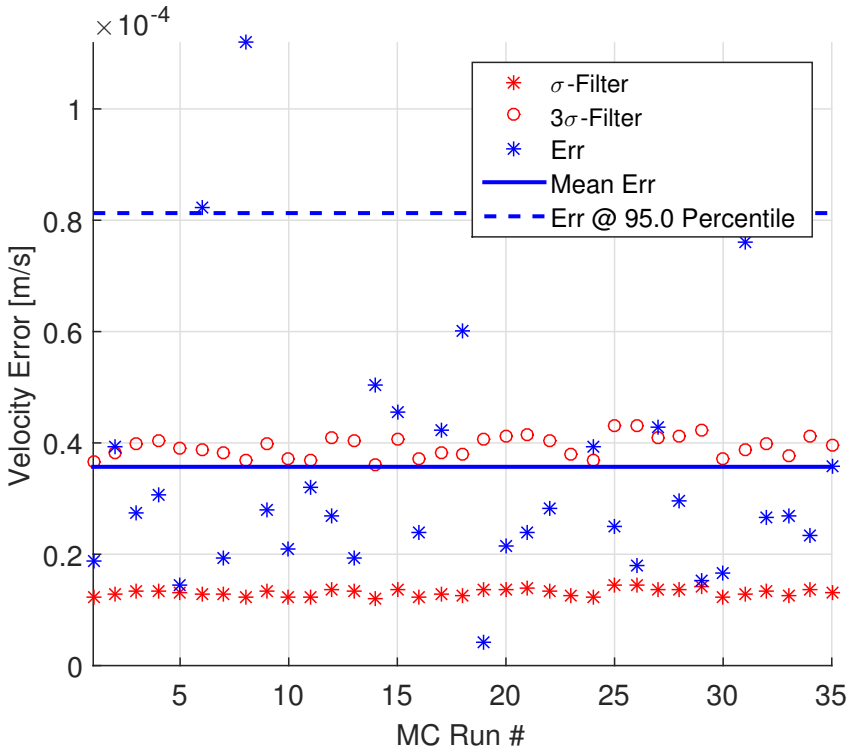

Figure 8.15: Final Monte-carlo results for the velocity

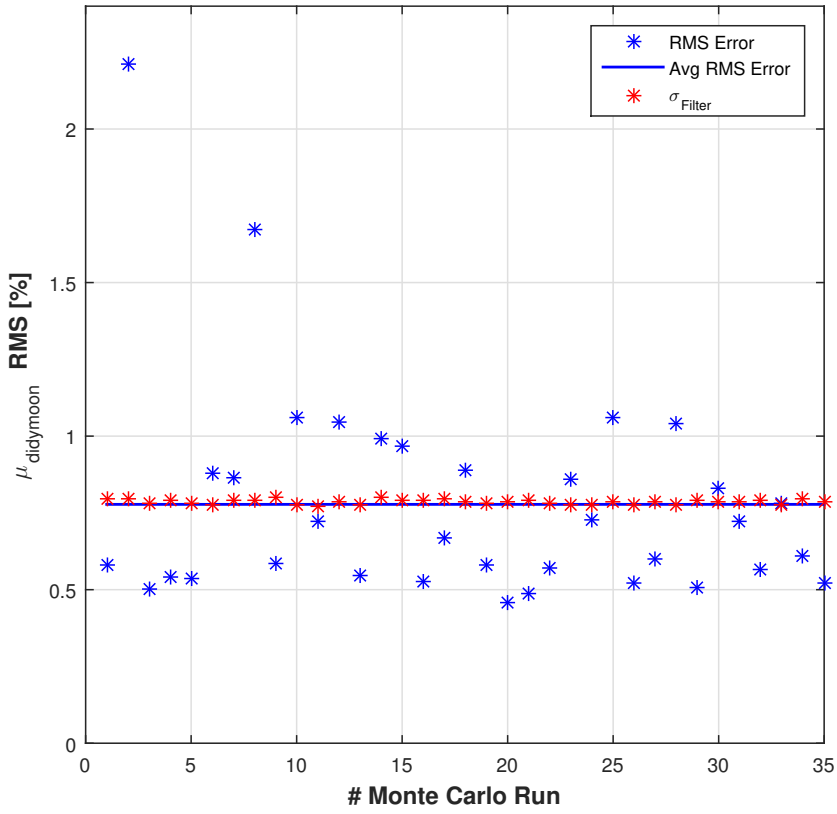

Figure 8.16: Final Monte-carlo results for the estimation of Didymoon's mass

Chapter 9
Conclusions and Recommendations

This chapter summarises the conclusions that can be extracted from the work of this MSc Thesis project, in particular those things which have been dealt with during Chapter 7 and Chapter 8. Firstly, a final navigation strategy for the orbit determination will be depicted. Then, all conclusions that can be extracted from the present work will be listed. This chapter will end with the outline for possible working areas that could follow the present work.

9.1. Navigation Strategy Selection

Bearing in mind the operational constraints, elaborated in Subsection 7.2.5, and all results in Chapter 8, two final navigation strategies are proposed. These strategies, depicted in Table 9.1 and Table 9.2, were thought to minimise operational costs, while maximising the quality of the orbit determination and parameter estimation.

The orbit determination is suggested to follow the following schematic to safely overcome the scale-factor indetermination and improve the final orbit solution:

- First phase
  - First estimate of Didymoon's trajectory by the use of centroid tracking.
  - Use of Didymoon's trajectory and Didymain's centroid tracking to obtain a first estimate of the asteroid masses.
- Second phase
  - Incorporation of the radiometry into the orbit determination
  - Computation of the ephemeris of the Didymos barycentre.
- Third and final phase
  - Incorporation of landmark tracking
  - Estimation of Didymain's rotational state
  - Final tuning of all dynamical parameters and final precise orbit solution.

Once the orbit determination of the available arcs is complete, the SC state is to be propagated two days up to the next manoeuvring node using the best and last estimation. The updated manoeuvre timeline is uplinked to the SC, which will carry out its execution and a new arc begins.

Table 9.1: ECP Orbit Determination Strategy #1: Nav - Navigation Arc, Sci - Science Arc, OD - Orbit Determination

Day	Wed	Thu	Fri	Sat	Sun	Mon	Tue	Wed	Thu	Fri	Sat	Sun	Mon	Tue
SC	Nav	Sci	Sci	Nav	Nav	Sci	Sci	Nav	Sci	Sci	Nav	Nav	Sci	Sci
Grnd	-	OD	OD	-	-	OD	OD	-	OD	OD	-	-	OD	OD

Table 9.2: ECP Orbit Determination Strategy #2: Nav - Navigation Arc, Sci - Science Arc, OD - Orbit Determination

Day	Sat	Sun	Mon	Tue	Wed	Thu	Fri	Sat	Sun	Mon	Tue	Wed	Thu	Fri
SC	Nav	Nav	Sci	Sci	Nav	Sci	Sci	Nav	Nav	Sci	Sci	Nav	Sci	Sci
Grnd	-	-	OD	OD	-	OD	OD	-	-	OD	OD	-	OD	OD

9.2. Conclusions

Here below, the conclusions, extracted from the this MSc. Thesis's work, are listed. Their rationale is briefly explained, and, if recommendations apply, they are included.

- The expected error of the orbit determination along the radial axis is several times larger than that along the along and cross-track axes, and it cannot be eliminated.
- The scale factor indetermination can be overcome and the asteroid's size can be estimated to an accuracy of several metres. It is impossible to solve for the scale factor without the inclusion of radiometric measurements.
- An overall accuracy (3-sigma) of 5.5 meters and 1.2 mm/s in the orbit determination can be guaranteed. While the precision of the propagated solution has a dispersion of tenths of metres in position and one tenth of millimetres per second in velocity that compromises the manoeuvre calculation.
- A 3% accuracy (3-sigma) on the secondary component's mass can be assured by the end of the early-characterisation phase.
- Manoeuvre execution errors have been seen to cause important trajectory deviations. However, their impact on the navigation performance is negligible.
- A weak correlation has been observed between the Earth's location w.r.t the system and the quality of the telemetry. Thus, these analyses could be generalised to all relative Earth-SC-Asteroid orientations.
- No correlation between navigation performance and the phase angle has been observed for values contemplated in the mission design requirements. However, for those values that do not meet the phase angle requirement, the performance of the navigation quickly deteriorates. It seems the mission constraint on the phase angle can be pushed to 90 degrees without compromising the SC safety.
- The navigation performance could be improved by either carrying an altimeter or a steerable high-gain antenna. The improvement in the navigation performance seems to be similar for both cases.

9.3. Future Work

The following section, gathers possible working areas, which open after the current work.

9.3.1. Hybrid and Fully-autonomous Navigation

During the past decades, autonomy has been gaining a more important role in deep-space missions. What was before a tedious task carried out by human operators, has become nowadays being automatised, where autonomous systems are being entrusted with increasingly important roles. In the past, budget costs have been manly done in all aspects of interplanetary missions but operation costs.

These problems together with increased mission capabilities are currently being addressed by the increasing share of automatisation. This entails new problems for which new analyses shall be performed. In this thesis, the complete ground orbit-determination process has been analysed, as a consequence of AIM's low budget. Nevertheless, in the near future, on-board image processing will become a trend.

The hybridisation of the still-entrusted to ground OD with the new automatised on-board algorithms shall be properly addressed. New interfaces will appear, were sensor data fusion together with the different estimates, of ground and on-board, will impose hard challenges that shall be solved. Thus, the following study areas in asteroid navigation assessments can be identified:

- On-board autonomous navigation
- Autonomous and ground-based navigation hybridisation
- Sensor-data fusion
- High-fidelity modelling

9.3.2. HERA mission

During the ESA Ministerial Council in Lucerne, 2016, AIM failed to get the necessary financial support to carry on with the mission. New concepts were assessed, where the tighter budget limited many mission capabilities of AIM. Finally, in November 2017 a new concept was presented. The 2022 joint mission with NASA's DART was rejected and a new mission scenario was projected. This new concept was called HERA[1].

HERA's main objectives remained the same that those of AIM. Thus, the HERA mission stands out for:

- First ever analysis of an impact crater of an asteroid deflection test.
  - Accurately measure the momentum transfer between the impactor and the asteroid, for which a precise estimation of the moon's mass is needed.
  - Impact model validation in terms of crater size and morphology, and scaling laws.
- First deep-space 6U CubeSat via inter-satellite link.
  - Allowing high-resolution close-up imaging of Didymos
  - Complementary science package with radio-science, mineralogy, seismology, and surface properties characterisation.
  - Close-up impact characterisation for DART (if delayed) and JAXA's impactor.
- First mission to a binary asteroid system.

The mission's target body was kept to Didymos, however, if new binary asteroids were to be discovered, their potential as targets will be assessed. Two new launch opportunities are being assessed, one in November 2023 and the other one in November 2024. The potential of including a different impactor, made by JAXA, with a total different impact energy to that of DART will be assessed.

In terms of navigation, which is the main concern of this thesis, the payload baseline was set to include a micro-LIDAR. As previously concluded, the presence of a ranging instrument is key for improving the accuracy of the navigation, and solving for the scale factor. Thus, the work of this thesis can serve as a staring point for future navigation assessments. These will need to deal with sensor-data fusion and the hybridisation of autonomous and ground-based navigation.

[1] Extracted from https://www.cosmos.esa.int/documents/336356/1503750/SMPAG09_HERA_Carnelli_2017-10-11.pdf/c2c0e63d-256f-6335-1229-7e1fea4cd733 on 28th November 2017

Annex A

Acceptance Test - Detailed Characterisation Phase (DCP)

Here below, some results on the software acceptance test are displayed.

Just as described in Subsection 6.3.4, the detailed-characterisation phase (DCP) was used to validate the complete functionality of the software. The overall performance of the navigation was compared to the FASTMOPS AIM's Navigation Assessment data, both in terms of SC position and velocity. In Figure A.2 the reference velocity navigation performance is shown and it is compared to the output of the software, in Figure A.3. The knowledge on the SC velocity is of the same order for both cases.

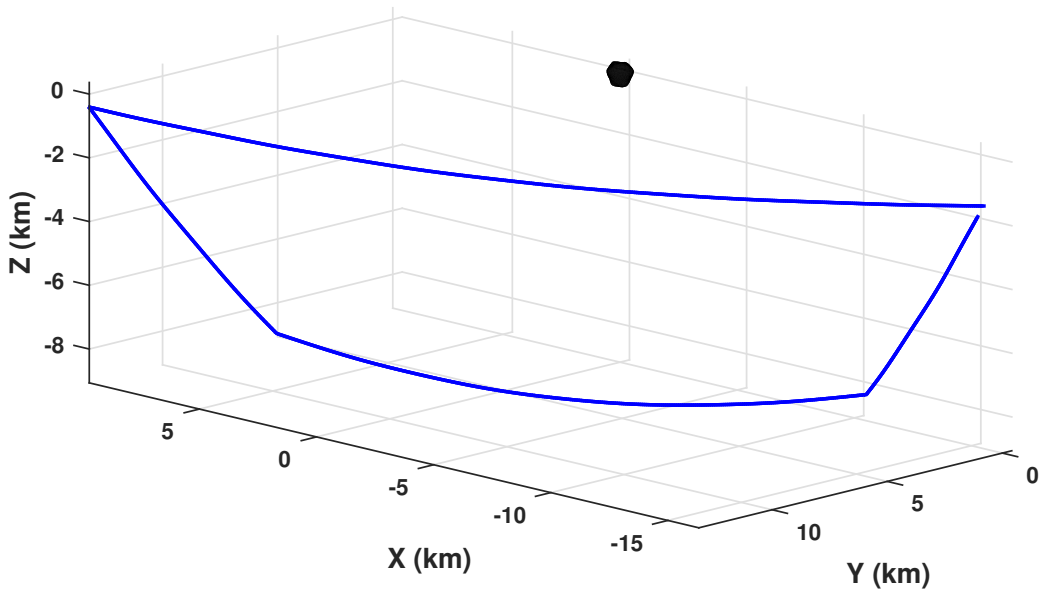

Figure A.1: AIM's DCP Trajectory

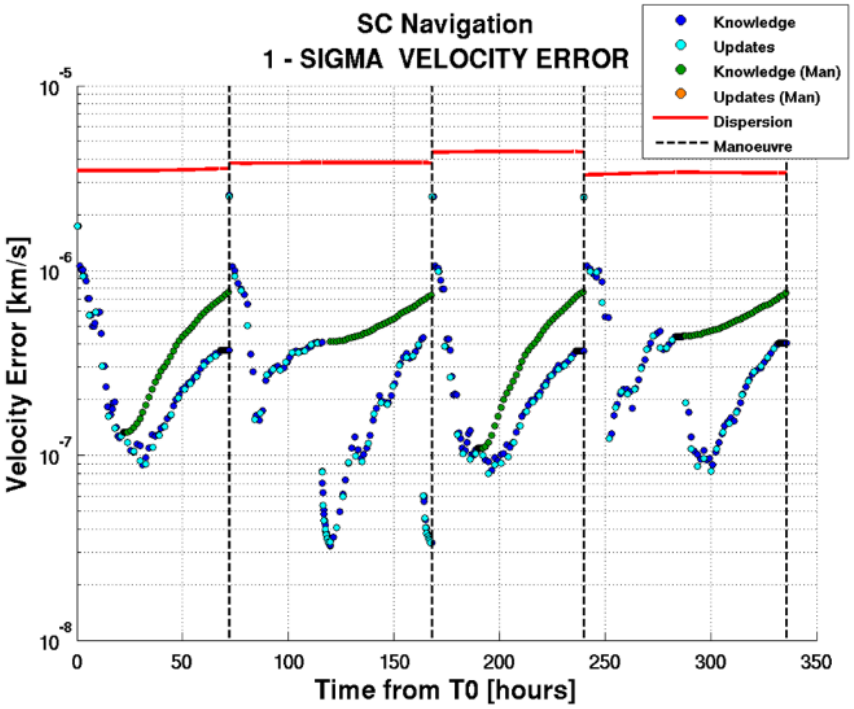

Figure A.2: AIM's DCP Velocity Navigation and Guidance Performance for five DCP Arcs

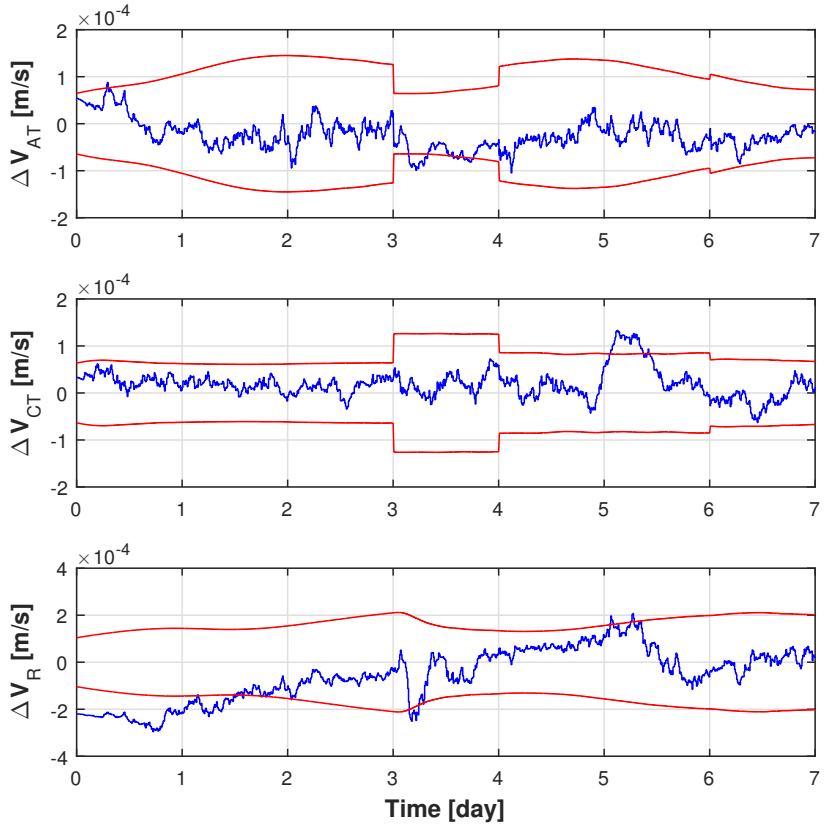

Figure A.3: Velocity Navigation Performance for four DCP arcs

Annex B

The Early Characterisation Phase (ECP)

Here in this annex, all extra analyses that are interesting for the navigation analyses are displayed and their results discussed. An extensive overview of the early-characterisation phase (ECP) is shown below.

In Table B.1, the positions in the Didymos J2000 reference frame are displayed. The complete evolution of some important variables along AIM's orbit during the ECP are shown in Figure B.1. These plots shown the evolution of the distance to the asteroid, the excess velocity over the escape velocity, the latitude, and the phase angle. Over each plot, the communication windows are shown in red, while optical navigation arcs are shown in blue.

Table B.1: ECP nodes position

	Node 1	Node 2	Node 3	Node 4
r_x [km]	14.89	8.42	-19.83	-15.19
r_y [km]	18.17	14.00	-68.32	12.94
r_z [km]	18.66	-20.09	-21.09	17.48
Distance [km]	30.00	25.90	30.00	26.52

B.1. Alternative approaches to the scale-factor problem

An alternative approach to the solving of the scale-factor problem was presented in Section 7.3. It consists on the complete non-dimensionalisation of the problem. All parameters that carry information about distances are non-dimensionalised by the selected scale-factor. Some examples of this are shown in Equations (B.1)-(B.2). The complete navigation problem is then solved by the use of these non-dimensional parameters. Results show that the uncertainty in the scale is carried by all parameters until radiometric measurements start to be available and are fed into the filtering process. This effect can be observed in Figure B.2.

$$\mathbf{X}_{SC_{pos}} = scale \cdot \mathbf{x}_{SC_{pos}} \tag{B.1}$$

$$\begin{aligned} \mu_{Didymos} &= scale^3 \cdot \mu_{Didymos_s} \\ \mu_{Didymoon} &= scale^3 \cdot \mu_{Didymoon_s} \end{aligned} \tag{B.2}$$

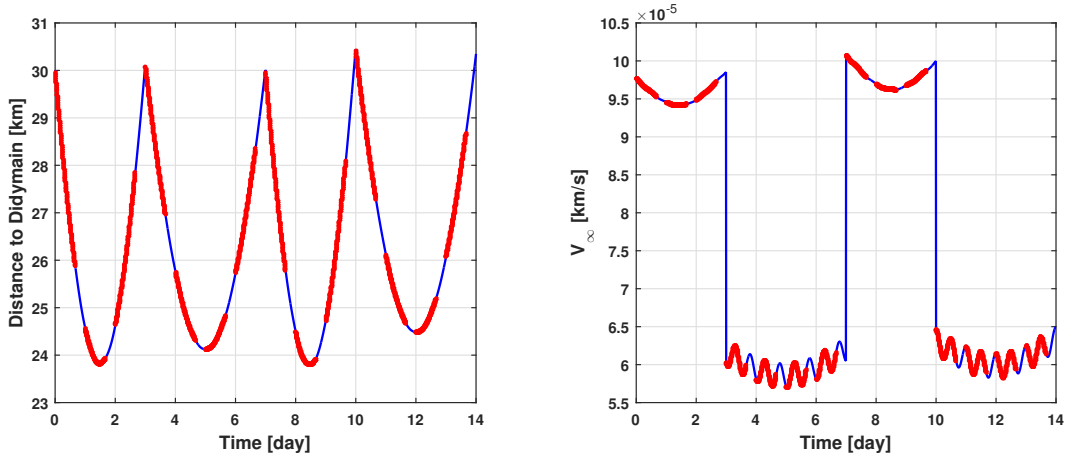

(a) Distance (b) Excess Velocity

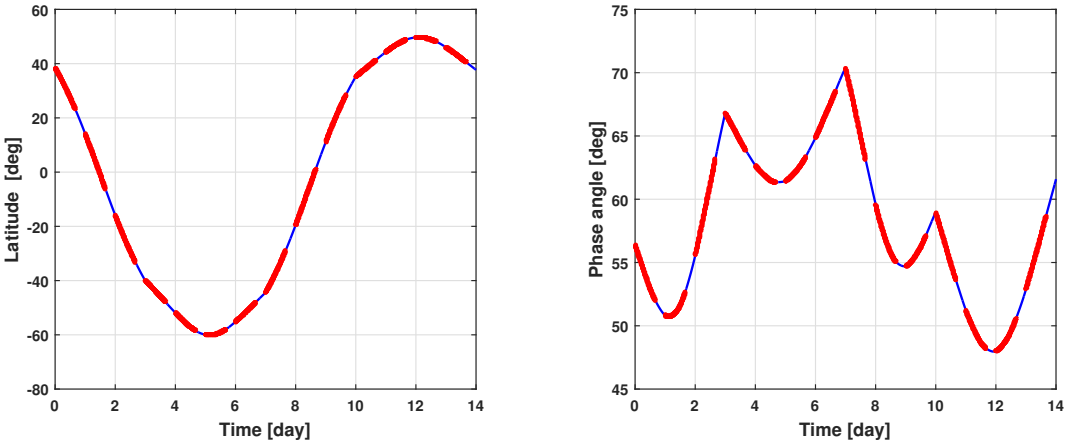

(c) Latitude (d) Phase Angle

Figure B.1: AIM's ECP Trajectory

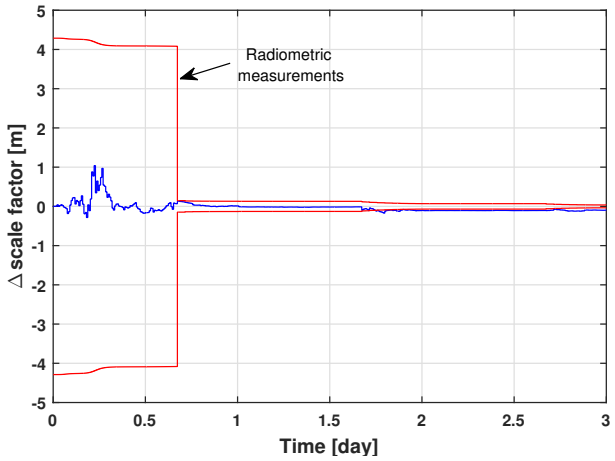

Figure B.2: Centre of Gravity Offset Navigation Error

B.2. Alternative analyses

Some alternative analyses that are interesting for the characterisation of the navigation design have been carried out. Between all of them, two stand out: the inclusion of a steerable high-gain antenna and altimeter measurements.

B.2.1. Steerable high gain antenna

If AIM were to carry a steerable high-gain antenna, the antenna could be oriented to Earth whilst the cameras are pointing to the asteroid. Thus, communications could be established at the same time optical navigation is taking place. This would allow radiometry to be available at the same time landmarks are being tracked, thus, providing absolute information on distances and directly solving the scale-factor indetermination. Results show an outstanding improvement in the navigation solution, as seen in Table B.2 and Table B.3. The majority of this improvement comes from the radial axis, since there is now information along this axis at all working epochs, thus dramatically improving its accuracy.

Table B.2: Position navigation error

	Units	RMS
Along-track position	[m]	0.42
Cross-track position	[m]	0.49
Radial position	[m]	0.98
Position modulus	[m]	1.18

Table B.3: Velocity navigation error

	Units	RMS
Along-track velocity	[mm/s]	0.028
Cross-track velocity	[mm/s]	0.064
Radial velocity	[mm/s]	0.048
Velocity modulus	[mm/s]	0.085

B.2.2. Altimeter

Altimeters were carried by former asteroid missions such as NEAR-Shoemaker and Hayabusa, as explained in Chapter 2. However, these are very high-consuming devices which would increase power consumption and thus, ultimately, costs. They were removed from the AIM mission to save costs. An analysis on how the navigation improves when altimetry is included has been carried out.

Results in Table B.4 and Table B.5 show an improvement in the radial axis, just as expected. Nevertheless, the overall solution is not as good as that of the steerable HGA, due to non-simultaneity of radiometric and on-board measurements. The solution worsens during the communication arc, increasing the overall RMS. Nevertheless, carrying an altimeter proves to be the best solution for increasing the accuracy along the radial axis.

Table B.4: Position navigation error

	Units	RMS
Along-track position	[m]	0.52
Cross-track position	[m]	1.29
Radial position	[m]	0.85
Position modulus	[m]	1.64

Table B.5: Velocity navigation error

	Units	RMS
Along-track velocity	[mm/s]	0.036
Cross-track velocity	[mm/s]	0.094
Radial velocity	[mm/s]	0.065
Velocity modulus	[mm/s]	0.120

B.3. Final navigation strategy results

Here in this section, the results of the final navigation strategy as described in Section 9.1 are shown. These are the most precise results that both meet the requirements and the assumptions. Numerical results for the orbit determination are displayed in Table B.6 and Table B.7. The maximum precision along the radial axis seems to be of the same order as the across-track axis. However, the causes behind each are quite different.

The maximum precision along the radius is determined by the character of the optical measurements, while the error along the cross-track direction seems to be caused only by operational constraints. This was observed when the inclusion of a steerable high-gain antenna was simulated, where the error along the cross-track direction is almost equal to the error in the along-track. The effect is observed in the spikes produced during the communication windows, as seen in Figure B.3.

The navigation error evolution for the mass of the Didymos system and Didymoon are also displayed. Lastly, the equivalent area for the solar radiation pressure is shown. This was modelled following a process noise model, due to the high uncertainty on its value. This uncertainty is observed in the navigation solution, which only manages to achieve a RMS of 1.5 square metres, while the actual value is about 7.5 square meters.

Table B.6: Position navigation error

	Units	RMS
Along-track position	[m]	0.63
Cross-track position	[m]	1.42
Radial position	[m]	1.42
Position modulus	[m]	2.10

Table B.7: Velocity navigation error

	Units	RMS
Along-track velocity	[mm/s]	0.03
Cross-track velocity	[mm/s]	0.10
Radial velocity	[mm/s]	0.07
Velocity modulus	[mm/s]	0.13

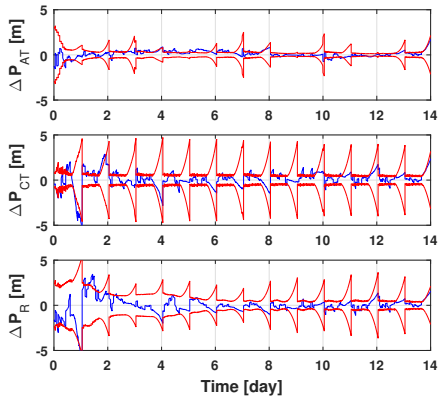

(a) Position

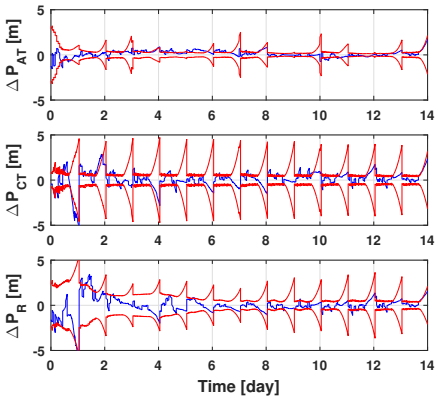

(b) Velocity

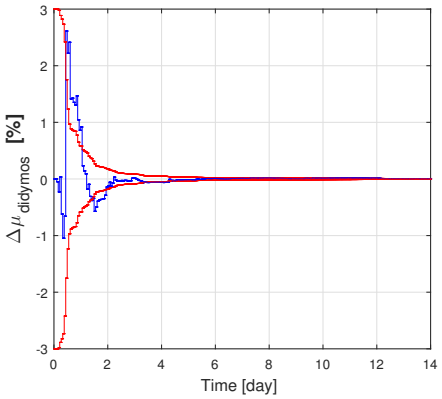

(c) Didymos gravitational parameter

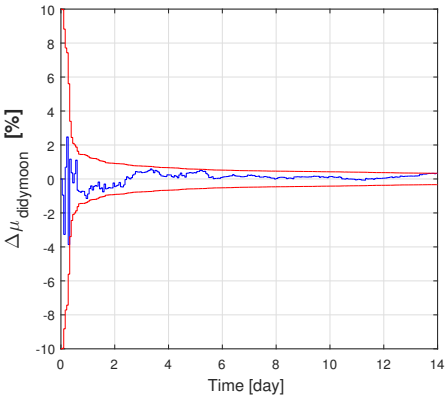

(d) Didymoon gravitational parameter

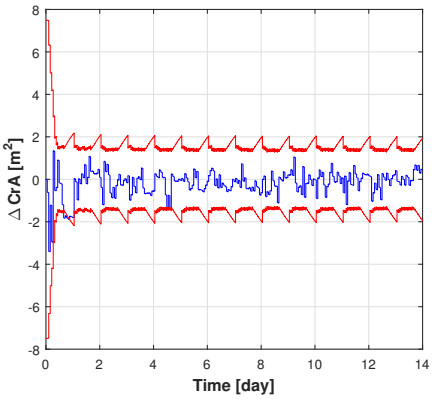

(e) SRP equivalent area

Figure B.3: Navigation error

Annex C
GMV Inputs

This annex will describe the interface between GMV's contributions and the exposed work. A clarification of the software design and implementation, exposed in Chapter 6, will also be carried out.

The present work has been carried out at GMV Aerospace and Defence in Tres Cantos, Spain. GMV has a long heritage in GNC-system design, mission analysis, and interplanetary missions. This heritage and its involvement in the Asteroid Impact Monitoring mission (AIM) has been of great help for the present MSc Thesis project. GMV possesses two navigation-analysis toolboxes that have been handed over to help with the project and the software design, validation, and verification. These two are Filtering and Estimation Toolbox (FEST) and SBNav/INTNav.

FEST is a MATLAB navigation toolbox that allows to perform navigation assessments to the user. FEST's high-level architecture, in other words, its skeleton, has been the basis on which the developed software has been integrated. FEST integrates a graphical user interface that allows the selection of mission scenarios, navigation filters, and sensors.

SBNav/INTNav are two FORTRAN toolboxes that perform covariance analyses on a provided mission-scenario. SBNav's covariance analysis resembles the objective structure for the navigation.

FEST has been used as the basis for the simulator integration. Its structure has been kept as the skeleton of the simulator described in Section 6.1. The integrated high-level functions have been developed from the scratch and integrated into FEST's structure. These functions are listed below with all their lower level functions that were developed in the process.

Real world SC dynamics around Didymos, DOPRI5, DOPRI8, Didymoon ephemeris generation and storage, etc.

Sensors Range, Doppler, DDOR, centroiding, landmark matching, altimeter, operational availability, etc.

Navigation Filter SRIF algorithm, Cholesky decomposition, House-holder transformation, partial-derivatives calculation, etc.

Guidance FTOA algorithm, manoeuvre calculation, dispersion propagation, ground-knowledge propagation, operations, etc.

Post-processing measurement residuals, navigation error, LM-post processing, nav-camera live-views, LM visualisation.

On the other hand some low level functions have been reused; their source is indicated below:

FEST frame transformations such as inertial to LVLH, quaternions to DCM and vice versa, cross product, non-spherical gravity acceleration.

SBNav landmark generation (translated from FORTRAN).

Spice Toolkit keplerian elements to Cartesian coordinates and the ephemeris of the Sun, Earth, and Didymos.

Here below in Table C.1, all documents that have been consulted for the present work is listed. The reference style followed by GMV has been used though this report, when referring to GMV's internal documents. These are property of GMV and are not publicly available.

Table C.1: GMV Applicable Documents

AD	Doc Code	Issue	Document name
AD01	GMV 20490/17 V1/17	1.2	EN01 - AIM Mission Analysis Report
AD02	GMV 20009/17	1.0	FASTMOPS CCN - AIM Ground Performance Analyses
AD03	GMV 22645/14 V1/14	1.2	TN01 - FASTMOPS Assumptions Consolidation
AD04	GMV 40151/14 V1/14	1.4	TN03 - FASTMOPS Software Design Document
AD05	GMVSA 2086/93	1.0	Software Tool for Interplanetary Navigation
AD06	GMV 23099/13 V1/13	1.0	IANT - Autonomous Navigation Technologies State-of-the-art

Annex D
Frame transformations

Here in this annex, the more common frame transformations, described in Section 3.1 used during this work will be listed.

SC body frame to camera frame

$$\begin{pmatrix} x \\ y \\ z \end{pmatrix}_{CAM} = \begin{bmatrix} 0 & 1 & 0 \\ 0 & 0 & -1 \\ -1 & 0 & 0 \end{bmatrix} \begin{pmatrix} x \\ y \\ z \end{pmatrix}_{SC} \tag{D.1}$$

Didymos ecliptic J2000 to orbital frame

$$\begin{aligned} \mathbf{u}_R &= -\frac{\mathbf{x}_{SC}}{r} \\ \mathbf{u}_{CT} &= \mathbf{u}_R \times \frac{\mathbf{v}_{SC}}{V} \\ \mathbf{u}_{AT} &= \mathbf{u}_{CT} \times \mathbf{u}_R \end{aligned} \tag{D.2}$$

$$\begin{pmatrix} x \\ y \\ z \end{pmatrix}_{orb} = \begin{bmatrix} \mathbf{u}_{AT} & \mathbf{u}_{CT} & \mathbf{u}_R \end{bmatrix} \begin{pmatrix} x \\ y \\ z \end{pmatrix}_{DEJ2000} \tag{D.3}$$

where AT stands for along-track, CT for cross-track, and R for radial

Didymos ecliptic J2000 to SC body frame

$$\begin{pmatrix} x \\ y \\ z \end{pmatrix}_{SC} = \begin{bmatrix} 1-2(q_2^2+q_3^2) & 2(q_1q_2+q_3q_0) & 2(q_1q_3-q_2q_0) \\ 2(q_2q_1-q_3q_0) & 1-2(q_1^2+q_3^2) & 2(q_3q_1+q_1q_0) \\ 2(q_3q_1+q_2q_0) & 2(q_3q_2-q_1q_0) & 1-2(q_1^2+q_2^2) \end{bmatrix} \begin{pmatrix} x \\ y \\ z \end{pmatrix}_{DEJ2000} \tag{D.4}$$

Didymos ecliptic J2000 to Didymain body frame

$$\begin{pmatrix} x \\ y \\ z \end{pmatrix}_{DM} = \begin{bmatrix} \cos\theta & -\sin\theta & 0 \\ \sin\theta & \cos\theta & 0 \\ 0 & 0 & 1 \end{bmatrix} \begin{bmatrix} \cos\lambda & 0 & \sin\lambda \\ 0 & 1 & 0 \\ -\sin\lambda & 0 & \cos\lambda \end{bmatrix} \begin{bmatrix} \cos\beta & -\sin\beta & 0 \\ \sin\beta & \cos\beta & 0 \\ 0 & 0 & 1 \end{bmatrix} \begin{pmatrix} x \\ y \\ z \end{pmatrix}_{DEJ200} \tag{D.5}$$

where β is de right ascension of Didymain's rotation axis, λ its declination, and θ the rotation of the asteroid.

Bibliography

Battin, R. (1968), *An Introduction to the Mathematics and Methods of Astrodynamics,*, 1999 edn, AIAA, Wright-Patterson Air Force Base.

Branco, J. a., Cabral, F., Milhano, T., Sousa, B. and Voirin, T. (2016), "Fastmops - filling the gap from quasi-stationaty orbit down to a phobos automated approach for landing", *in* "SpaceOps 2016", SpaceOps, Daejeon, p. 18.

Butcher, J. (1987), *The Numerical Analysis of Ordinary Differential Equations: Runge-Kutta and General Linear Methods*, 1st edn, Wiley-Interscience, New York.

Cheng, A. F., Atchison, J., Kantsiper, B., Rivkin, A. S., Stickle, A., Reed, C., Galvez, A., Carnelli, I., Michel, P. and Ulamec, S. (2015), "Asteroid impact and deflection assessment mission", *Acta Astronautica* Vol. 115, pp. 262–269.

Companys, V. (2015), The rosetta mission flight operations, Technical report, ESOC, ESA.

De León, J., Licandro, J., Serra-Ricart, M., Pinilla-Alonso, N. and Campins, H. (2010), "Observations, compositional, and physical characterization of near-earth and mars-crosser asteroids from a spectroscopic survey", *Astronomy & Astrophysics* Vol. 517, p. A23.

Delpech, M., Bissonnette, V. and Rastel, L. (2015), "Vision based navigation for proximity operations around asteroid 99942 apophis", *in* "Proceedings of the 25th International Symposium on Space Flight Dynamics (ISSFD), Munich, Germany".

Di Lizia, P. (2008), "Robust space trajectory and space system design using differential algebra", PhD thesis, Politecnico di Milano.

ESOC (2014), Navigation analysis for comet operations up to ssp delivery, Technical report, ESA, Darmstadt.

Genova, A., Marabucci, M. and Iess, L. (2012), "A batch-sequential filter for the bepicolombo radio science experiment", *in* "Journal of Aerospace Engineering, Sciences and Applications", Vol. 4, pp. 17–30.

Gil-Fernandez, J. and Gomez-Tierno, M. A. (2010), "Optimal guidance of low-thrust trajectories", *Journal of guidance, control, and dynamics* Vol. 33 nr. 6, pp. 1913–1917.

Gil-Fernandez, J., Ortega, G., Casasco, M., Huertas, I., Dubois-Matra, O. and Carnelli, I. (2016), "Esa gnc technologies for asteroid characterization, sample-return, and deflection missions", *in* "2016 IEEE Aerospace Conference", pp. 1–9.

Gil-Fernández, J., Panzeca, R. and Corral, C. (2008), "Impacting small near earth objects", *Advances in Space Research* Vol. 42 nr. 8, pp. 1352–1363.

Godard, B., Budnik, F., Noz, P. M., Morley, T. and Janarthanan, V. (2015), "Orbit determination of rosetta around comet 67p/churyumov-gerasimenko", *in* "Proceedings 25th International Symposium on Space Flight Dynamics–25th ISSFD, Munich, Germany", Munich.

Grieger, B. and Küppers, M. (2017), "Determining the mass of didymos' secondary by visual imaging", *in* "EGUGA 2017", EGU General Assembly, Vienna.

Hahn, W. (1967), *Stability of Motion*, 1st edn, Springer-Verlag, Berlin.

Herfort, U. and Casas, C. M. (2015), "Trajectory preparation for the approach of spacecraft rosetta to comet 67p/churyumov-gerasimenko", *in* "Proceedings 25 th International Symposium on Space Flight Dynamics-25 th ISSFD, Munich, Germany", Munich.

Iess, L., Abello, R., Ardito, A., Comoretto, G., Lanucara, M., Maddè, R., Mercolino, M., Rapino, G. and Tortora, P. (2006), "The software correlator for esa delta-dor", *in* "4th Radionet Engineering Forum Workshop: Next Generation Correlators for Radio Astronomy and Geodesy", Vol. 28.

Johnson, A. E. and Matthies, L. H. (1999), "Precise image-based motion estimation for autonomous small body exploration", *in* "AIRAS 1999", Artificial Intelligence, Robotics and Automation in Space, Noordwijk, p. 627.

Kawaguchi, J. H. (2006), "Summary of guidance, navigation, and control achievement in its proximity phase", *AIAA* Vol. 6533, pp. 21–24.

Kicman, P., Lisowski, J. and Bidaux-Sokolowski, A. (2016), "Vision-based navigation around small bodies", *in* A. N. AstroNet-II, ed., "Astronet-II 2016", Springer, Cham, Tossa de Mar, pp. 137–149.

Kominato, T., Matsuoka, M., Uo, M., Hashimoto, T. and Kawaguchi, J. (2006), "Optical hybrid navigation and station keeping around itokawa", *AIAA/AAS Astrodynamics Specialist Conference and Exhibit* Vol. p. 6535.

Kubota, T., Hashimoto, T., Kawaguchi, J., Uo, M. and Shirakawa, K. (2006), "Guidance and navigation of hayabusa spacecraft for asteroid exploration and sample return mission", *in* "Sice-Icase 2006", Sice-Icase, Bexco, pp. 2793–2796.

Leondes, C. (1968), *Advances in Control Systems: Theory and Applications*, 2014 edn, Academic Press, London.

Michel, P., Cheng, A., Küppers, M., Pravec, P., Blum, J., Delbo, M., Green, S., Rosenblatt, P., Tsiganis, K., Vincent, J.-B. et al. (2016), "Science case for the asteroid impact mission (aim): a component of the asteroid impact and deflection assessment (aida) mission", *Advances in Space Research* Vol. 57 nr. 12, pp. 2529–2547.

Miller, J. K., Konopliv, A., Antreasian, P., Bordi, J., Chesley, S., Helfrich, C., Owen, W., Wang, T., Williams, B., Yeomans, D. et al. (2002), "Determination of shape, gravity, and rotational state of asteroid 433 eros", *Icarus* Vol. 155 nr. 1, pp. 3–17.

Montenbruck, O. (1992), "Numerical integration methods for orbital motion", *Celestial Mechanics and Dynamical Astronomy* Vol. 53 nr. 1, pp. 59–69.

Montenbruck, O. and Gill, E. (2000), *Satellite Orbits*, 1st edn, Springer, Wessling.

Munoz, P., Budnik, F., Companys, V., Godard, B., Casas, C., Morley, T. and Janarthanan, V. (2015), "Rosetta navigation during lander delivery phase and reconstruction of philae descent trajectory and rebound", *in* "Acta Astronautica", Vol. 125, pp. 65–79.

Munoz, P., Budnik, F., Godard, B., Morley, T., Companys, V., Herfort, U. and Casas, C. (2012), "Preparations and strategy for navigation during rosetta comet phase", *in* "ISSFD 2012", International Symposium on Space Flight Dynamics, Pasadena.

NASA (2009), Delta-differential one way ranging operations, Technical report, NASA, Washington.

Pardo De Santayana, R. and Lauer, M. (2015), "Optical measurements for rosetta navigation near the comet", *in* "Proceedings of the 25th International Symposium on Space Flight Dynamics (ISSFD), Munich, Germany", Vol. 150, pp. 1619–1637.

Parisi, M., Finocchiaro, S. and Iess, L. (2012), "Multi-arc and batch-sequential filters for the orbit determination of esa's juice mission", *in* "ISSFD 2012", International Symposium on Space Flight Dynamics, Pasadena.

Pellacani, A., Naudet, J., Suatoni, M. and Stefanescu, R. (2016), "Aim vision based gnc", *in* "IAC 2016", IAC, Guadalajara.

Prince, P. J. and Dormand, J. R. (1981), "High order embedded runge-kutta formulae", *Journal of Computational and Applied Mathematics* Vol. 7 nr. 1, pp. 67–75.

Richardson, D. C., Barnouin, O. S., Benner, L. A. M., Bottke, W., Campo Bagatin, A., Cheng, A. F., Eggl, S., Hamilton, D. P., Hestroffer, D., Hirabayashi, M., Maurel, C., McMahon, J. W. and Michel, P. (2016), "Dynamical and physical properties of 65803 didymos", *in* "AAS 2016", American Astronomical Society, The Woodlands.

Scheeres, D. (2002), "The orbital dynamics environment of 433 eros", *Ann Arbor* Vol. 1001 nr. 2002, pp. 48109–2140.

Shirakawa, K., Morita, H., Uo, M., Kubota, T. and Kawaguchi, J. (2006), "Accurate landmark tracking for navigating hayabusa prior to final descent", *in* "AAS/AIAA Space Flight Mechanics Meeting, 2006", Tampa.

Shuang, L. and Pingyuan, C. (2008), "Landmark tracking based autonomous navigation schemes for landing spacecraft on asteroids", *Acta Astronautica* Vol. 62 nr. 6-7, pp. 391–403.

Sidi, M. J. (1997), *Spacecraft Dynamics and Control*, 1st edn, Cambridge, Tel Aviv.

Simon, D. (2006), *Optimal state estimation: Kalman, H infinity, and nonlinear approaches*, John Wiley & Sons.

Suatoni, M., Gonzalez-Arjona, D., Casasco, M., Dubois-Matra, O., Gil-Fernandez, J. and Pellacani, A. (2016), "Hil testing of a vision-based autonomous gnc for the aim mission", *in* "IAC 2016", IAC, Guadalajara.

Takeishi, N. (2013), "Automatic landmark recognition for asteroid by image features", *in* "IEEE Institute of Electrical and Electronics Engineers, 2013", Dalian.

Takeishi, N., Yairi, T., Tsuda, Y., Terui, F., Ogawa, N. and Mimasu, Y. (2015), "Simultaneous estimation of shape and motion of an asteroid for automatic navigation", *in* "IEEE 2015", IEEE, Seattle.

Tapley, B. D., Schutz, B. E. and Born, G. H. (2004), *Statistical Orbit Determination*, 1st edn, Elsevier, San Diego.

Tempelman, W. (1986), "Linear guidance laws for space missions", *Journal of Guidance, Control, and Dynamics* Vol. 9 nr. 4, pp. 495–502.

Wakker, K. F. (2015), *Fundamentals of Astrodynamics*, 1st edn, TU Delft, Delft.

Wertz, J. (1978), *Spacecraft Attitude Determination and Control*, 1st edn, Kluwer, Silver Spring.

Wie, B. (2008), *Space Vehicle Dynamics and Control*, 3rd edn, AIAA, Iowa.

Williams, B. G. (2002), "Technical challenges and results for navigation of near shoemaker", *Johns Hopkins APL technical digest* Vol. 23 nr. 1, pp. 34–45.